Quasi-static Axial Compression Behavior of Empty and Polystyrene Foam Filled Aluminum Tubes

By

Ahmet Kaan TOKSOY

A Dissertation Submitted to the Graduate School in Partial Fulfillment of the Requirements for the Degree of

MASTER OF SCIENCE

Department : Mechanical Engineering
Major: Mechanical Engineering

Izmir Institute of Technology
Izmir, Turkey

September, 2003

We approve the thesis of **Ahmet Kaan Toksoy**

Date of Signature

---------- **15.09.2003**

Assoc. Prof. Dr. Mustafa GÜDEN
Supervisor
Department of Mechanical Engineering

---------- **15.09.2003**

Asst. Prof. Dr. Metin TANOĞLU
Co-Supervisor
Department of Mechanical Engineering

---------- **15.09.2003**

Asst. Prof. Dr. Bülent YARDIMOĞLU
Department of Mechanical Engineering

---------- **15.09.2003**

Asst. Prof. Dr. H. Seçil ALTUNDAĞ ARTEM
Department of Mechanical Engineering

---------- **15.09.2003**

Asst. Prof. Dr. Selahattin YILMAZ
Department of Chemical Engineering

---------- **15.09.2003**

Assoc. Prof. Dr. Barış ÖZERDEM
Head of Department

ACKNOWLEDGEMENTS

I would like to thank my advisor Assoc.. Prof. Dr. Mustafa Güden for his guidance and encouragement. During the course of this study, he shared his all knowledge and practice in experimental study with me. I would like to thank IZOCAM® and METALUM® corporations for Extruded Polystyrene foam and Extruded Aluminum tube supplying for this thesis, respectively. Besides, I am very thankfull to MAM staff because of their helpings during the experimantal study. Finally I would like to thank to Eylem Erdoğan and my family for their patience and support.

ABSTRACT

The strengthening effect of foam filling and the effect of foam filling on the crushing properties of the light weight foam filled circular tubes were investigated through the polystyrene foam filled thin-walled Al tubes of 16 and 25 mm in diameter. The empty tubes crushed progressively in asymmetric (diamond) mode. The foam filling however turned the deformation mode into progressive axisymmetric (concertina) mode in 25 mm Al tube, while the deformation mode in foam filled 16 mm Al tube remained to be the same with that of the empty tube. The strengthening coefficients of foam-filling defined as the ratio between the increase in the average crushing load of the filled tube with respect to empty tube and plateau load (load corresponding to the plateau stress of the foam) were found to be 1.8 and 3.2 for the concertina and diamond mode of deformation, respectively. The higher value of strengthening in diamond mode of deformation was attributed to the filler deformation beyond the densification region. This was also confirmed by the microscopic observation of the partially crushed sections of the filled tubes. The interaction effect between tube and filler was assessed by the compression testing of the partially foam filled tubes. The effects of filler density, deformation rate (in the range between 0.001-0.04 s^{-1}) and the use of adhesive between the tube wall and filler on the average crushing load, stroke efficiency and specific absorbed energy of the tubes were determined. The specific absorbed energy of the filled tube was compared with that of the empty tubes of wall thickening on the equal mass basis. Finally, two modes of deformation modes were proposed for the crushing behavior of the foam filled thin-walled Al tubes.

ÖZ

Hafif köpük malzeme doldurulmuş silindirik tüplerin ezilme özellikleri üzerindeki köpük doldurma ve köpük doldurmadaki kuvvetlendirme etkileri 16 ve 25 mm çaplı ince alüminyum tüplere polistiren köpük doldurularak incelenmiştir. Boş tüpler devamlı asimetrik (Elmas) modda ezilmişlerdir. Köpük doldurulmuş 25 mm tüplerde deformasyon modu devamlı axisimetrik (Konsantrik) deformasyon moduna dönmüş, fakat köpük doldurulmuş 16 mm Al tüplerin deformasyon modu boş olanları ile aynı kalmıştır. Köpük doldurmadaki kuvvetlendirme katsayıları, dolu tüplerdeki ortalama ezilme kuvveti artışının boş tüplere ve plato (köpük malzemelerin plato stresine eşit olan kuvvet) yüklerine oranı, konsantrik modu için 1.8, elmas deformasyon modu için 3.2 olarak bulunmuştur. Elmas deformasyon modundaki yüksek kuvvetlendirme değerleri tüp katlanmalarının arasında kalan köpük malzemelerinin yoğunlaşma bölgesinin ötesinde deformasyona uğramaları nedeni ile daha yüksek yüklerin dolgu malzemesi tarafından taşınması ile açıklanmıştır. Bu davranış dolu tüplerin kısmi ezilmiş bölümlerinin mikroskop altında incelenmesi ile de doğrulanmıştır. Tüp ve dolgu malzemesi arasındaki etkileşim etkisi yarı dolu tüplerin test edilmesi ile tespit edilmiştir. Dolgu malzemesi yoğunluğunun, deformasyon oranın ($0.001\text{-}0.04\ s^{-1}$) ve tüp ile dolgu malzemesi arasında yapıştırıcı kullanımının ortalama ezilme yükleri, stroke verimleri ve spesifik absorbe enerjileri üzerine olan etkileri belirlenmiştir. Dolu tüpün spesifik absorbe edilmiş enerjisi aynı ağırlıktaki et kalınlığı değişik boş tüplerinkiler ile karşılaştırılmıştır. Son olarak köpük doldurulumuş tüplerin ezilme davranışları için iki deformasyon modu önerilmiştir.

TABLE OF CONTENTS

LIST OF FIGURES

LIST OF TABLES

NOMENCLATURE

A_E	Crush force efficiency
C	Strengthening coefficient of the foam filling
D	Mean diameter
D_C	Deformation capacity
E	Absorbed energy
E^*	Elastic modulus of the foam
E_s	Elastic modulus of the solid material
H_F	Fold length
I	Interaction coefficient
k	Strain-rate sensitivity
K,n	Power law type hardening relation coefficients
l	Total length of deformation element
L_0	Initial length of tension test specimen
L	Final length of tension test specimen
m_{foam}	Mass of deformation element
m_t	Total mass of deformation element
m_{tube}	Mass of deformation element
N	Number of the circumferential folds
P_a	Average crush load of empty tubes
$P_{a,f}$	Average crush load of foam filed tubes
P_{at}	Atmospheric pressure
P_f	The foam load corresponding to the plateau stress
P_{fp}	The average crushing loads of the foam-filled tube without axial compression of the foam
P_{int}	Interaction load
P_{max}	Maximum deformation load
P_0	Initial gas pressure of the foam cells
R	Anisotropy ratio
SAE	Specific absorbed energy
S_E	Stroke efficiency

t	Thickness of tube
T_E	Total crush efficiency
ε_d	Densification strain of foam
ρ^*	Foam density
ρ_c	Tube material density
ρ_s	Solid material density
σ_c	Collapse stress of the foam
σ_{el}^*	Elastic collapse stress of foam
σ_p	Plateau stress of the foam
σ_{pl}^*	Plastic collapse stress of foam
σ_U	The ultimate tensile stress of the tube material
σ_0	Mean plastic flow stress of the tube material
$\sigma_{0.2}$	Proof strength of the tube material

Chapter I

INTRODUCTION

The collapse of Word Trade Center (WTC), whose main frame was made of steel columns, has raised the questions whether or not the columnar structures can be safely used in structural applications against the external treats that include impacts of foreign objects and airplanes and whether or not it can be possible to increase the safety limits of these structures without significantly increasing total mass. Recent numerical study on the collapse of WTC (September 11, 2001) has clearly shown that these structures were vulnerable to relatively high velocity impacts and only a small percentage of the total impact energy of the Boeing 767 moving with a cruishing speed of 240 m s^{-1} was absorbed [1]. The crushing behavior of columnar structures including rectangular and circular metal tubes was studied extensively over the 30 years. In the last decade, the scientific interest shifted through filling the columnar structures with light-weight foams because foam-filling results in an increase in the specific energy absorption over the sum of the specific energy absorption of the foam alone and tube alone. This is known as interaction effect and can potentially be used in many diverse engineering applications including main frames of structural parts such as bridges, buildings and large platforms and energy absorbing units such as packages and crush boxes in automobiles.

The strengthening effect of foam filling in rectangular tubes were experimentally and numerically studied and shown to be about 2 times of the foam plateau load [2]. This was found to increase further when an adhesive was used to bond filler to tube wall [3]. Many studies of foam-filled circular tubes were aimed at determining the effect of foam filling on the specific energy absorption of the tube and no systematic study has been performed on the strengthening of tubes with foam filling. In designing with foam filled tubes, knowledge of upper and lower limits of the strengthening is a prerequisite for the calculation of the specific absorbed energy for any tube-foam combination. This study was therefore conducted in order to determine the strengthening effect of foam filling in circular tubes folding with progressive asymmetric (diamond) and progressive axisymmetric (concertina) modes.

Commercially available polystyrene foam in three different densities was chosen for the filling of the Aluminum (Al) tubes in various tube wall thickness and diameter. The effects of foam density, deformation rate and the use of adhesive on the crushing properties of the tubes including average crushing load, stroke efficiency and specific absorbed energy were determined. A novel experimental method based on the compression testing of the partially foam-filled tubes was also performed aiming at determining the interaction effect between filler and tube. The specific absorbed energy in foam filled tubes was compared with those of empty tubes on equal mass basis by means of simple analytical calculations of the wall thickening strengthening of the empty tubes. Based on experimental results two models of foam-filled tube crushing have been proposed.

Chapter II

BACKGROUND

2.1 Foams: Structure and Compression Deformation Behavior

Foams are the light-weight materials made of groups of cells. Nature uses these materials in many applications. The cellular structure of the wood is mechanical; that is to support the tree and cancellous bone is to give animals a light and stiff frame. Among many other purposes, the nature's choice of foams is also for the optimization of fluid transport and thermal insulation.

Synthetic man made foams are usually inspired from nature and they may be considered in two groups in terms of cell structure; open and closed-cell foams (Figure 2.1) and in three groups in terms of mechanical behavior: elastomeric, elastic-plastic and elastic-brittle foams (Figures 2.2(a), (b) and (c)).

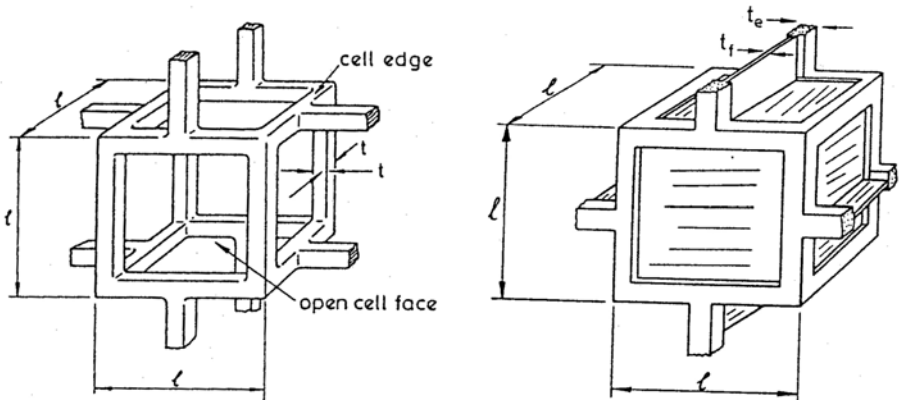

(a) (b)

Figure 2.1 Cubic models of a) open-cell and b) closed-cell foams [4].

Under compressive loads, foams show characteristic stress-strain behavior. Compressive stress-strain curve consists of three consecutive regions: linear elastic, plateau or collapse and densification (Figure 2.2) [4, 5].

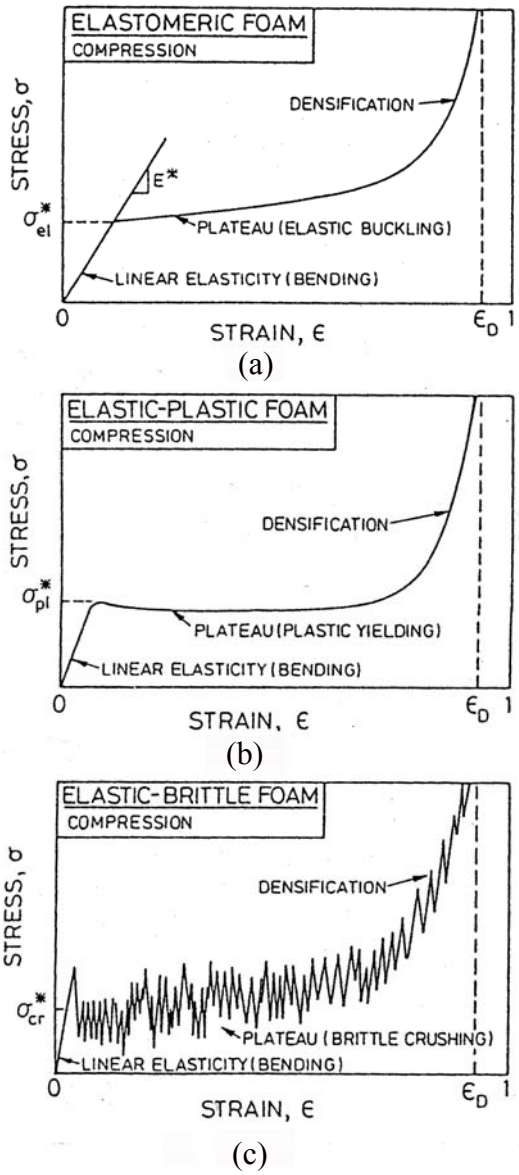

Figure 2.2 Compressive stress-strain curves of a) elastomeric, b) elastic-plastic and c) elastic-brittle foam [4].

2.1.1 Linear Elasticity

Open cell foam of low relative densities (the ratio between foam density and solid foam material density (ρ^*/ρ_s)), deforms primarily by cell wall bending [6]. With increasing relative density (ρ^*/ρ_s>0.1), cell edge compression plays a significant role. Fluid flow through open-cell foam contributes to the elastic moduli if the fluid has a high viscosity or the strain rate is exceptionally high. Besides cell edge deformation, the thin membranes of the closed cell foams, which form the cell faces, stretch normal

to the compression axis and therefore contribute to the modulus. If the membranes do not rapture, the compression of the cell fluid trapped within the cells also increases the modulus. Each of these mechanisms contributing to the linear-elastic response of the foams is shown schematically in Figures 2.3(a) and (b) for open and closed-cell foams, respectively.

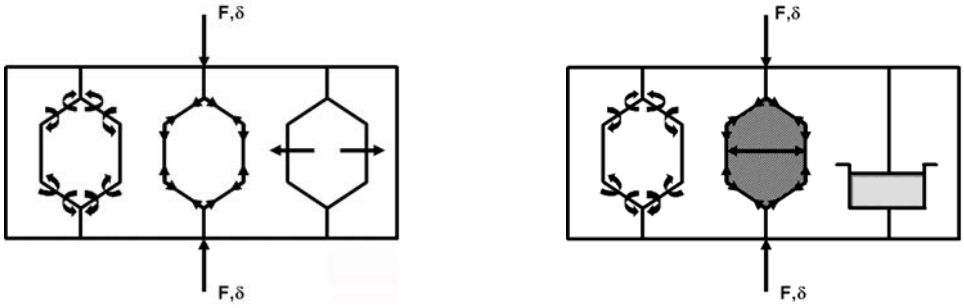

(a) (b)

Figure 2.3 The mechanisms of foam deformation: a) open-cell foam, sequentially cell wall bending, cell wall axial deformation and fluid flow between cells and b) closed-cell foams, sequentially cell wall bending and contraction, membrane stretching and enclosed gas pressure [4].

The simplest model of foam structure is the cubic model, which encompasses cubic array of members of length l and square cross-section of side t (Figures 2.1(a) and (b)). The structure and shape of the cells are actually more complex than those of the cubic model. The deformation and failure mechanisms of the cubic model are however quite similar to those of real foams and therefore it is very useful in predicting mechanical properties.

The elastic modulus of the open cell foams (E^*), which is calculated from the linear-elastic deflection of a beam of length l loaded at its mid point by a load F, is given as [4];

$$\frac{E^*}{E_s} = C_1\left(\frac{\rho^*}{\rho_s}\right) \tag{2.1}$$

where s refers to the solid material from which the foam is made and C_1 is a constant. The experimental elastic modulus of open-cell foams showed that C_1 is nearly equal to unity. The experimental results have further showed that the Poisson ratio (υ^*) was around 0.3 [4].

In closed-cell foams, a fraction of the solid, represented by ϕ, is contained in the cell edges having a thickness of t_e and the remaining fraction, $(1-\phi)$, is in the cell faces of a thickness of t_f. By including enclosed gas pressure, the Elastic modulus of closed-cell foams of the cubic model is expressed as [4],

$$\frac{E^*}{E_s} = C_1\varphi^2\left(\frac{\rho^*}{\rho_s}\right) + C_1'(1-\varphi)\frac{\rho^*}{\rho_s} + \frac{P_0(1-2\nu^*)}{E_s\left(1-\rho^*/\rho_s\right)} \tag{2.2}$$

where P_o is the initial pressure of the cell fluid and C_1 and C_1' are the constants. The first, second and third terms of Equation 2.2 are the contribution of cell wall bending, membrane stretching and enclosed gas pressure, respectively.

2.1.2 Elastic and Plastic Collapse

Linear elasticity is generally limited to small strains, 5% or less. Elastomeric foams can be compressed much larger strains. Deformation is still recoverable, but non-linear. In compression the stress-strain curve shows an extensive plateau at the elastic collapse stress (σ^*_{el}), see Figure 2.2(a). The elastic collapse stress of cubic cell model is given as [4];

$$\frac{\sigma^*_{el}}{E_s} = 0.05\left(\frac{\rho^*}{\rho_s}\right) \tag{2.3}$$

for open cell and,

$$\frac{\sigma^*_{el}}{E_s} = 0.05\left(\frac{\rho^*}{\rho_s}\right) + \frac{(P_0 - P_{at})}{E_s} \tag{2.4}$$

for closed-cell foams, respectively. P_{at} is atmospheric pressure (100 kpa).

Foams made from material that have a plastic yield point such as rigid polymers and ductile metals collapse plastically when loaded beyond the linear-elastic region. Plastic collapse gives a long horizontal plateau in the stress-strain curve similar to the

elastic buckling, but the strain is no longer recoverable. Both elastic buckling and plastic failure are localized; a deformation band is usually formed transverse to the loading axis and propagates through undeformed sections of the foam with increasing strain until all the foam section is filled with the band [4].

The plastic collapse stress is predicted as [4],

$$\frac{\sigma^*_{pl}}{\sigma_{ys}} = 0.3\left(\frac{\rho^*}{\rho_s}\right)^{3/2} \tag{2.5}$$

for open-cell foams and ,

$$\frac{\sigma^*_{pl}}{\sigma_{ys}} = 0.3\left(\varphi\frac{\rho^*}{\rho_s}\right)^{3/2} + (1-\varphi)\frac{\rho^*}{\rho_s} + \frac{P_0 - P_{at}}{\sigma_{ys}} \tag{2.6}$$

for closed-cell foams. σ_{ys} is the yield stress of solid material.

2.1.3 Densification

Following the plateau region, at a critical strain, the cell walls start to touch each other and, as a result the foam densifies. The stress in this region increases rapidly and approaches to the strength of the solid foam material. The densification strain (ε_D) is related to relative density with following equation [4];

$$\varepsilon_D = 1 - 1.4\left(\frac{\rho^*}{\rho_s}\right) \tag{2.7}$$

2.1.4 Anisotropy

The anisotropy in cell shape measured by the ratio of the largest cell dimension to the smallest is called the shape-anisotropy ratio (R). The value of R varies from 1 for isotropic foam to 10 for very anisotropic foams [4]. The relation between the plateau stress and R is calculated using cubic cell model as,

$$\frac{(\sigma_{pl})_3}{(\sigma_{pl})_1} = \frac{2R}{1 + 1/R} \tag{2.8}$$

where 3 and 1 refer to the strongest and weakest directions, respectively. The strongest direction in polymeric foams is usually the rise direction in the foam expansion process and the transverse directions are relatively weaker. Cells are relatively longer in the rise direction, giving rise to higher modulus and plateau stress in this direction. Figures 2.4(a) and (b) show the effect of foam directions on the load-displacement curves of elastomeric and rigid plastic foams, respectively.

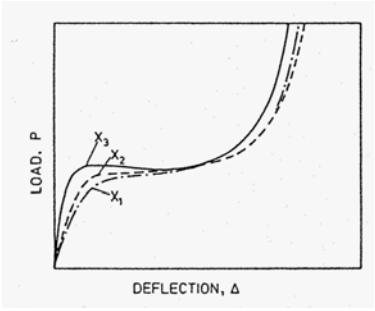

(a)

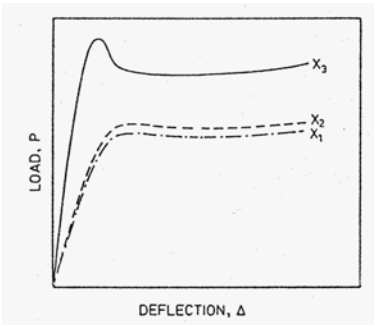

(b)

Figure 2.4 Load-deflection curves measured parallel to the three principal axes a) an elastomeric foam and b) a rigid plastic foam [4].

2.2 Tubes

The crushing behavior of thin (mean diameter(D)/ thickness(t) > 20 [7]) and thick-walled tubes has been experimentally studied since 1960. In parallel with experimental investigations, numeric and finite element analysis methods have been implemented and experimental results were compared with those of numerical studies. As mentioned in Chapter 1, the fall of the Word Trade Center reemerge scientific and engineering interest on the columnar structures. The filling of tubes with a light-weight polymeric and metallic foam has shown to be one of the effective way of increasing energy absorption of the columnar structures on the specific energy basis [8-13].

2.2.1. Terminologies Used In Crush Analysis

In any crushing event of columnar structure (Figure 2.5), the total absorbed energy (E) is the area under the load-displacement curve and is,

$$E(\delta) = \int_0^{\delta} P \, d\delta \tag{2.8}$$

where δ and P are the displacement and the load, respectively. The corresponding average crushing load (P_a) is calculated dividing the absorbed energy by the displacement,

$$P_a(\delta) = \frac{E(\delta)}{\delta} \tag{2.9}$$

The specific absorbed energy (SAE) shows the capability of a structure to absorb the deformation energy. SAE can be formulated in several bases including per unit mass and volume. SAE per unit mass is expressed as,

$$SAE = \frac{\int_0^{\delta} P \, d\delta}{m_t} \tag{2.10}$$

where m_t is the total mass of the deformation element.

The ratio between the average load P_a and maximum load P_{max}, both calculated in the interval of $\{0,\delta\}$, is defined as the crush force efficiency (A_E):

$$A_E = \frac{P_a(\delta)}{P_{max}(\delta)} = \frac{E(\delta)}{P_{max}(\delta)\,\delta} \tag{2.11}$$

Total efficiency (T_E) is the total absorbed energy divided by the products of $P_{max}(\delta)$ and total length of deformation element (l):

$$T_E = \frac{E(\delta)}{P_{max}(\delta)\,l} \tag{2.12}$$

The stroke efficiency is defined as the ratio between the point at which the total efficiency has its maximum value (δ_{max}) and total length of the crushing element,

$$S_E = \frac{\delta_{max}}{l} \tag{2.13}$$

The efficiency terms are directly related to the deformation capacity (D_C), which is the displacement divided by the initial length of the element:

$$D_C = \frac{\delta}{l} \tag{2.14}$$

$$E(\delta) = \int_0^{\delta} P \, d\delta$$

$$P_a(\delta) = \frac{E(\delta)}{\delta}$$

$$SAE = \frac{\int_0^{\delta} P \, d\delta}{m_t}$$

$$A_E = \frac{P_a(\delta)}{P_{max}(\delta)} = \frac{E(\delta)}{P_{max}(\delta)\,\delta}$$

$$T_E = \frac{E(\delta)}{P_{max}(\delta)\,l}$$

$$S_E = \frac{\delta_{max}}{l}$$

$$D_C = \frac{\delta}{l}$$

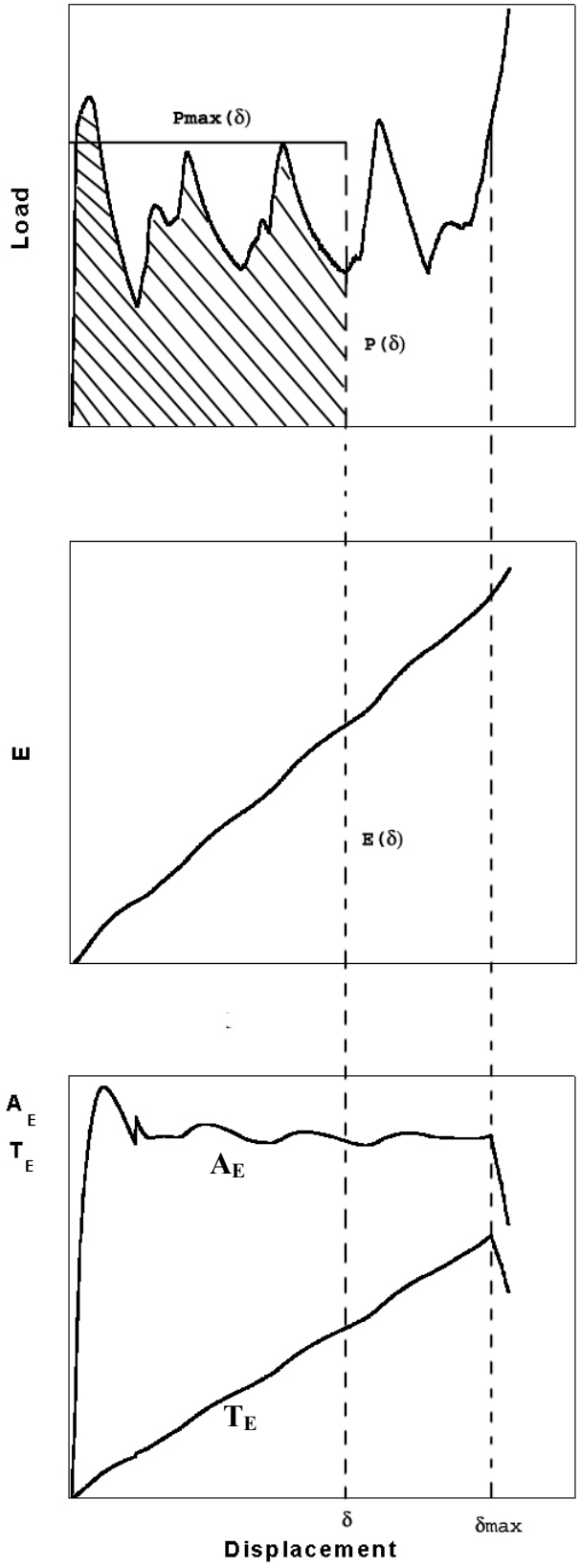

Figure 2.5 Terminologies used in the crush analysis of tubes.

2.2.2 Crushing Behavior of Empty Tubes

The crushing behavior of collapsible structures has been recently reviewed in [7] and briefly explained in this section. To our knowledge, the first analytical study on the crushing behavior of circular tubes was due to Alexander [14]. He modeled the concertina mode of deformation basing on the plastic work required for bending and stretching of extensible thin cylinder. Alexander's model of concertina mode of deformation (Figure 2.6) gives the average crushing load as;

$$P_a \cong 6\sigma_0 t(Dt)^{1/2} \tag{2.15}$$

σ_0 is the mean plastic flow stress;

$$\sigma_0 = \left(\frac{\sigma_{0.2} + \sigma_U}{2} \right) \tag{2.16}$$

where $\sigma_{0.2}$ is proof stress and σ_U is the ultimate tensile stress of tube material.

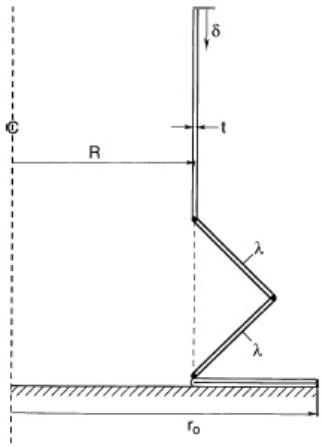

Figure 2.6 Alexander's concertina mode of deformation model.

Early studies were on the classification of the deformation modes as function of tube material properties, geometry and geometrical parameters of the tubes and the first systematic investigation on the classification of crushing types was due to Andrews *et al.* in 1983 [15]. They performed crushing tests on tubes having large ranges of t/D and L/D ratios and classified the crushing modes of cylindrical tubes in 7 groups. These are;

1. *Concertina*: axisymmetric and sequential or progressive folding starting at the end of the tube (Figures 2.7(a) and (b)).
2. *Diamond:* asymmetric but sequential folding accompanying a change in the cross-section shape of the tube (Figure 2.8(a) and (b)).
3. *Euler*: bending of tube as a strut.
4. *Concertina and 2 lobe and/or 3-lobe diamond (Mixed)*: Folding first in the concertina mode changing to diamond configuration (Figure 2.9(a) and (b))
5. *Axisymmetric/concertina*: simultaneous collapse along the length of the tube, axisymmetric single or multiple barreling of the tube (Figure 2.10(a) and (b) and Figure 2.11(a) and (b)).
6. *2-lobe diamond:* Simultaneous collapse along the tube in the form of the 2-lobe diamond configuration.
7. *Tilting of tube axis*: Shearing of tube on the platen surface in the form of the 2-lobe diamond configuration.

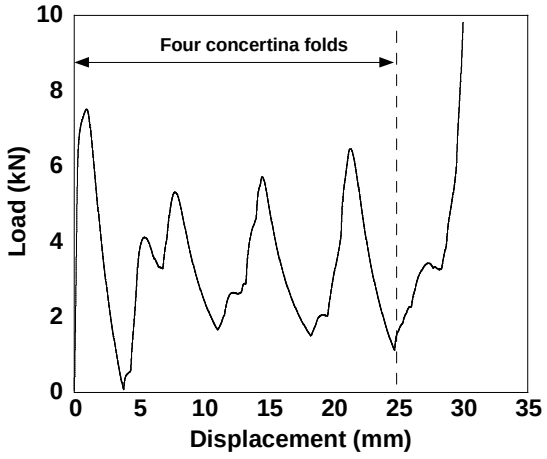

(a) (b)

Figure 2.7 a) Concertina mode of deformation in 6063 Al tube (D=19.16 mm and t= 0.84 mm) and b) corresponding load-displacement curve with 4-fold [16].

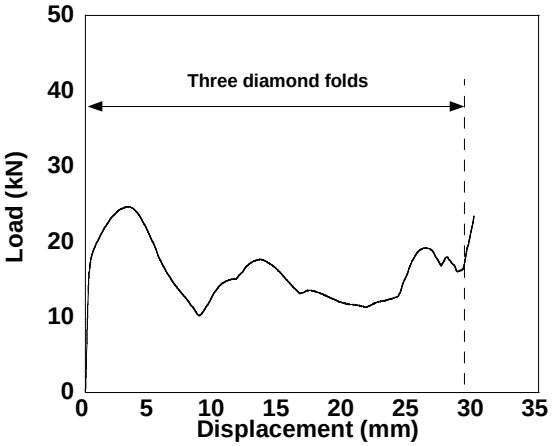

(a) (b)

Figure2.8 a) Diamond deformation mode in 6063 Al tube (D=17.5 mm and t=1.31 mm) and b) corresponding load-displacement curve with 3-fold [16].

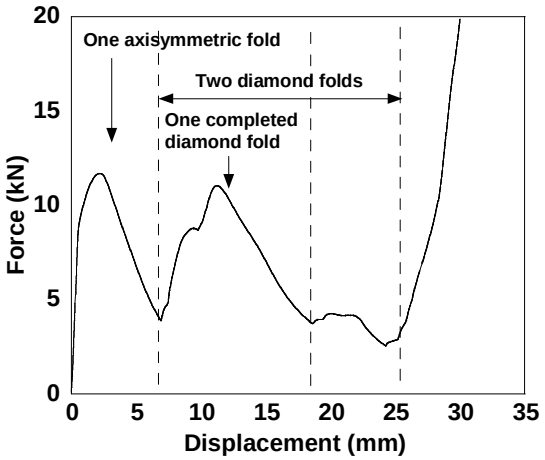

(a) (b)

Figure 2.9 a) Mixed mode of deformation in 6063 Al tube (D=20.63 mm and t=1.48 mm) and b)corresponding load-displacement curve with 3-fold [16].

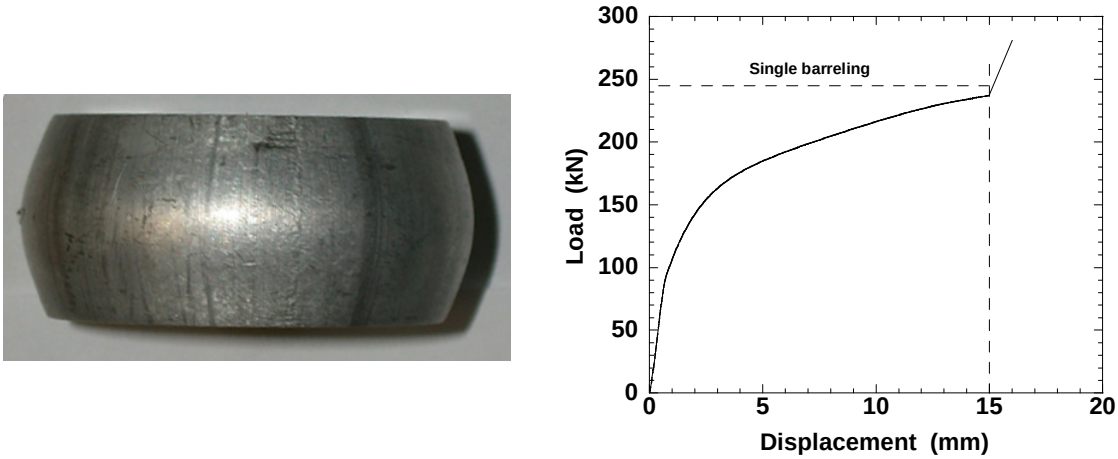

(a) (b)

Figure 2.10 a) Single barreling in 6063 Al tube (D=42.5 mm and t=7.5 mm) and b) corresponding load-displacement curve [16].

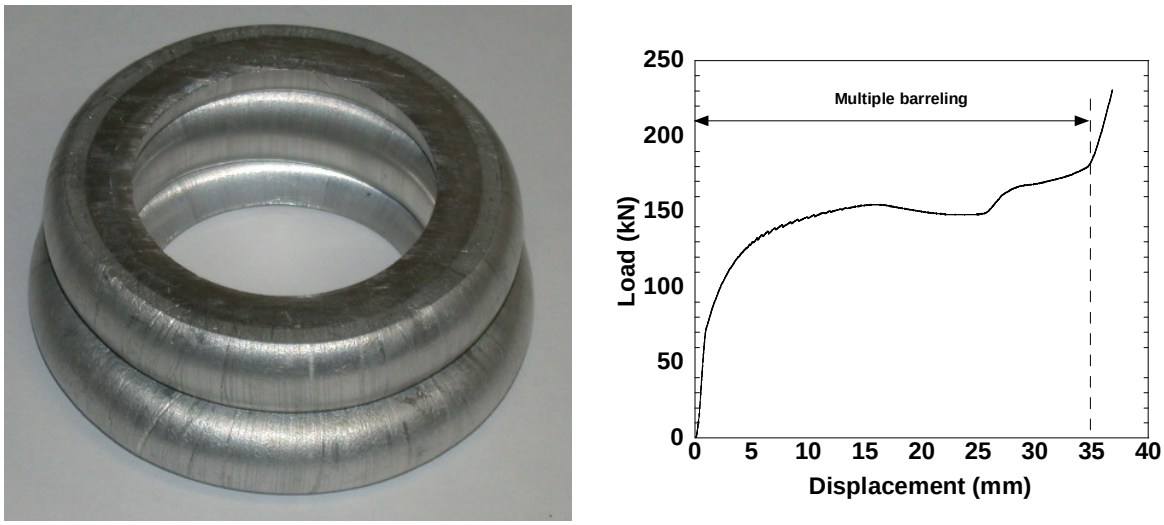

(a) (b)

Figure 2.11 a) Multiple barreling in 6063 Al tube (D=44.88mm and t=5.12mm) and b)corresponding load-displacement curve [16].

Andrews *et al.* also formed a chart that indicated the dominant deformation modes of HT30 Al alloy tube as functions of L/D and t/D (Figure 2.12). For the thin-walled tubes with t/D ratio smaller than 0.013, the deformation mode was found to be diamond and the number of folds increased with decreasing t/D ratio. It was also shown in this study that although the average crushing load and absorbed energy were higher in the concertina mode, the absorbed energy in the development of one complete fold was higher in diamond mode [15].

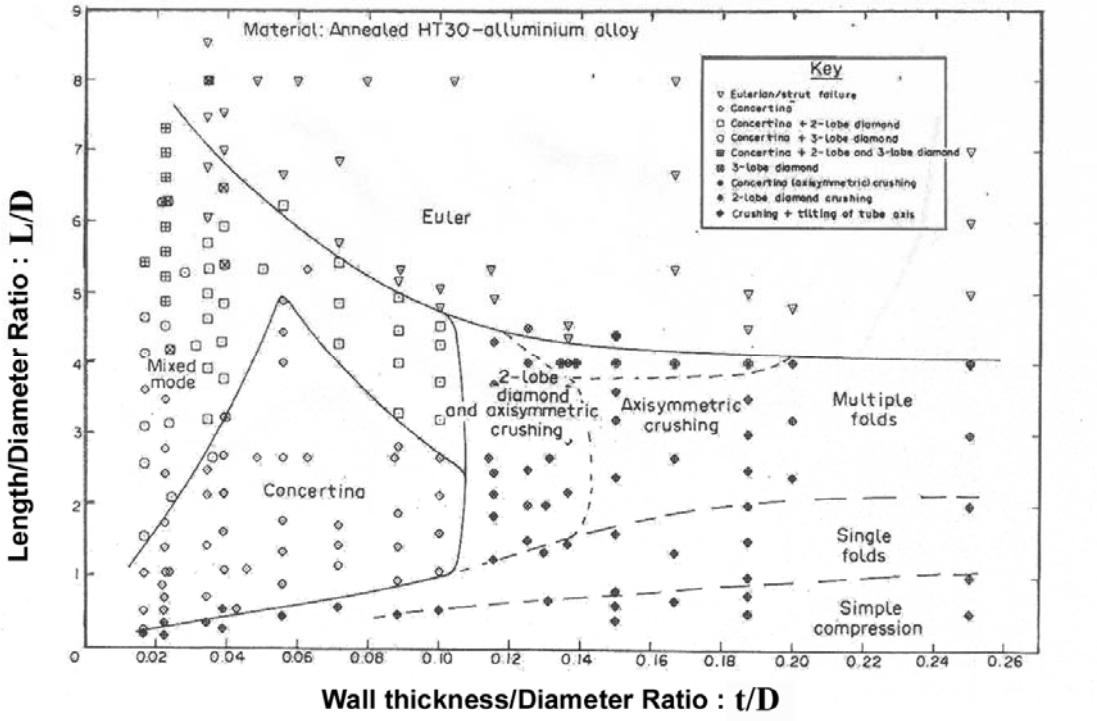

Figure 2.12 Classification of crushing mode of HT30 Al tubes as functions of D/t and L/t [15].

Abramowicz and Jones modified Alexander's model and proposed the average crushing load equations in 1984 and 1985 for the concertina mode of deformation [17, 18, 19] as,

$$P_a \cong \sigma_0 t\left(6(Dt)^{1/2} + 3.44t\right) \tag{2.17}$$

and

$$P_a \cong \sigma_0 t \frac{6\sqrt{Dt} + 3.44t}{0.86 - 0.57\sqrt{t/D}} \tag{2.18}$$

Wierzbicki *et al.* proposed an expression for the concertina mode of deformation as [20];

$$P_a = 7.933\,\sigma_0 t^2 \left(\frac{D}{t}\right)^{1/2} \tag{2.19}$$

Singace and Elbosky experimentally studied concertina mode of deformation [21]. They showed that concertina mode was composed of two characteristic movements: outward and inward folding (Figure 2.13). During the axial deformation, tube will be laid down partly to the inside and partly to the outside of the tube generator, the total of which is defined by the folding length in concertina deformation mode [22].

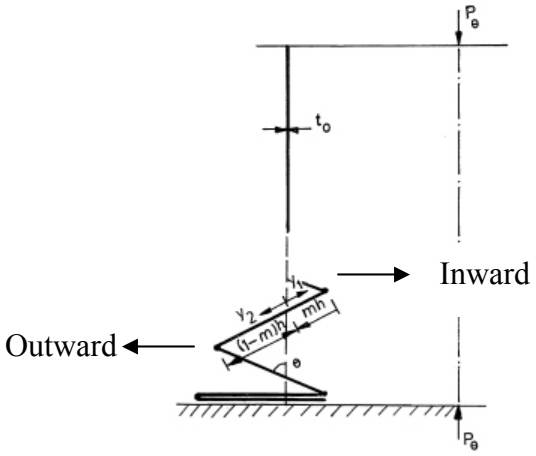

Figure 2.13 Concertina mode of circular tube deformation; inward and outward folding [21].

Outward fold length over total length of deformation fold is called eccentricity. The eccentricity factor was proposed to be 0.65, but experimentally determined values of the eccentricity factor was shown to be less than this value [22]. It was proposed that if continuous zone or curved elements were used to represent the folding elements, a

better agreement between the theory and the experimental results was expected [22]. Singace's analytical approach of mean crushing force is,

$$\frac{P_a}{M_P} \cong 22.27\left(\frac{D}{t}\right)^{1/2} + 5.632 \tag{2.20}$$

where $M_p = \sigma_0 t^2/2\sqrt{3}$ is the fully plastic bending moment per unit length [22].

By minimizing the total external work which is done by the total bending and membrane energy during the deformation, Singace proposed following equation for the mean crush load of diamond mode of deformation [23],

$$\frac{P_a}{M_P} \cong -\frac{\pi}{3}N + \frac{2\pi^2}{N}\tan\left(\frac{\pi}{2N}\right)\frac{D}{t} \tag{2.21}$$

where N is the number of the circumferential folds.

Alexander, assuming the energy was dissipated at the plastic hinges during the folding process of diamond mode of deformation, proposed following equation [14],

$$P_a \cong 2.286n^2\sigma_0 t^2 \tag{2.23}$$

where n is the number of diamonds formed.

Pugsley and Macaulay investigated the diamond mode of deformation of thin cylindrical columns having large D/t ratios [24]. The deformation energy was assumed to be absorbed by plastic bending and shear of the diamond pattern and following equation was proposed for the average crushing load of diamond mode of deformation,

$$P_a \cong \sigma_0 t(10.05t + 0.38D) \tag{2.24}$$

Wierzbicki gives an approximate expression for diamond mode of deformation as [10];

$$P_a \cong 18.15\sigma_0 t^2 (D/t)^{1/3} \tag{2.25}$$

For diamond mode of deformation, Abramowicz and Jones developed an expression for the mean crush force as [17]

$$\frac{P_a}{M_p} = 86.14\left(\frac{D}{t}\right)^{0.33} \tag{2.26}$$

In a recent study of Bardi *et al.* [25] the concertina mode of deformation in circular tubes was experimentally and numerically analyzed. Results of numeric model using ABAQUS were found to be close to those of experiments. The experimental results were also compared with the plastic hinge models of Alexander (Equation 2.15), Singace *et al.* (Equation 2.20) and Wierzbicki *et al.* (Equation 2.19). Although Wierzbicki *et al.* plastic hinge model predicted the load values in the range 81-91% of the measured values, predictions of the wavelength of the folds were generally poor for all three models.

H. Abbas *et al.* used the curved fold model for the analysis of concertina mode of deformation [26]. The curved fold model used was different from the previous studies of plastic hinge models of Alexander [14], Singace *et al.* [21] and Wierzbicki *et al.* [20] in a way that the straight portion of the fold was also included in the analysis. Three cases inside, outside and partly inside-outside folding, were investigated. It was found that when the accepted length of straight portion decreased, analytical load deformation curve become closer to the experimental curve in all cases. Analytical results of mean crushing load values and size of folds were also found to decrease with increasing the accepted length of straight portion but the results were still far from those of the experiments. The aim of their study was to show how mean crushing and energy absorption changed with folding parameter; m (ratio of inside fold to total fold length), as well with the parameter r (the ratio of yield stress values of the tube material in compression and tension).

Grupta and Abbas investigated the effect of thickness change in concertina folding of metallic round tubes [27]. They showed that by including thickness change, the calculated m values come closer to experimental values. Calculated average crushing loads, however, for different values of r (the ratio of the yield stress values of the tube material in compression and tension) were found to be lower than those of experiments. This was explained as fallows: since the next fold started even before the

complete crushing of previous fold, the crushing load observed in experiments started to rise before vertical crushing reached two times the size of the fold. The average crushing load was also found to increase with the increasing the value of r and reached to the experimental values [26]. They concluded that thickness change had no significant effect on the average crushing load.

Wierzbicki and Abramowicz [28, 29] developed average crushing load equations for square and hexagonal cross-sections as,

$$\frac{P_a}{M_0} \cong 48.64\left(b/t\right)^{0.37} \tag{2.27}$$

for square column and

$$\frac{P_a}{M_0} \cong 80.92\left(b/t\right)^{0.4} \tag{2.28}$$

for hexagonal column, where b is the length of the cross-section..

2.2.3. Crushing Behavior of Foam-Filled Tubes

Axial compression behavior of aluminum honeycomb filled square steel tubes was experimentally and numerically investigated by Seitzberger *et al*. [30]. It was shown that filling the steel tubes with aluminum foam increased both the deformation loads and specific absorbed energy over the sum of those of the foam alone plus tube alone. Finite element model and experimental results showed that measured and simulated behaviors were well agreed.

Crushing behavior of aluminum honeycomb and foam-filled box columns was numerically and experimentally investigated by Sanatoza and Wierzbicki [2, 3]. It was shown that the effect of filling on the tube crushing load was similar when the strong axis of the honeycomb through and normal to the compression axis, which was proving that both axial and lateral strength of the filler are effective in rising the crushing load of the tube. It was shown that aluminum foam filling had highest average crushing load and absorbed energy. In honeycomb filling, 2-D lateral and unidirectional

strengthening for axial compression direction were found to have the same effect on the crushing properties of tubes.

Santosa and Wierzbicki [31], based on FEM study, proposed following empirical equation for the average crushing load of foam-filled square tubes of length b,

$$P_{a,f} = P_a + C\sigma_p b^2 \tag{2.29}$$

where $P_{a,f}$, P_a and σ_p are the average crushing loads of the filled and empty tubes and plateau stress of the filler, respectively. The constant C in Equation 2.29 is considered strengthening coefficient of the foam filling. The values of C were numerically and experimentally shown to be 1.8 and 2.8 for foam filled square tubes with and without adhesive, respectively [31]. It was also shown by the same authors that there was a critical mass of the foam filled tube (or foam density) above which the foam filling was more efficient than tube wall thickening based on specific absorbed energy per unit mass.

Hannsen *et al.* studied static and dynamic crushing behavior of aluminum foam filled square aluminum extrusions [32, 33]. They showed that foam filled tubes formed more deformation folds as compared with empty tubes in both static and dynamic tests. This was explained as the stiffness effect of aluminum foam on sidewalls of deformation element, which decreased the buckling length of the sidewalls. It was also found that the average crush load of the filled tubes was higher than that of the sum of the crushing loads of the tube alone and foam alone, which is known as interaction effect. They also showed that stroke efficiency decreased with foam filling as compared with empty tubes.

They also modeled average crushing load of foam filled columns by including contributions of the average crushing force of empty tube, foam plateau stress and interaction effect. The model was found to be well agreed with experimental results and is given as

$$P_{a,f} = P_a + \sigma_p b^2 + C_{avg}\sqrt{\sigma_f \sigma_0}\, bh \tag{2.30}$$

where C_{avg} is a dimensionless constant which is directly related to the interaction effect.

Chapter III

MATERIALS AND MATERIALS CHARACTERIZATION

3.1 Polystyrene Foam Filler

As-received extruded polystyrene foam sheets with dimensions of 5x60x120 cm were manufactured by Izocam Company of Turkey using a process that produces partly oriented closed-cell foams with smooth continuous skins. The foam sheets investigated were supplied in three different densities with a trade name given to each of them as: i) Foamboard® 1500, ii) Foamboard® 2500 and iii) Foamboard® 3500. The densities of the foams, hereafter coded as F1500, F2500 and F3500, were determined by dividing the mass of the cubic foam sample (5x5x5 cm) by its volume and found to be 21.7 ± 1, 27.8 ± 2 and 32.1 ± 2 kg m^{-3} for F1500, F2500 and F3500, respectively. The corresponding mean relative densities; 0.0207, 0.0265 and 0.0305, were calculated by dividing the foam density to the dense polystyrene density (1050 kg m^{-3}).

The cell distribution in each as-received foam sheet was examined through three different planes (Figure 3.1); Extrusion-Width (E-W), Rise-Width (R-W) and Extrusion-Rise (E-R) and are sequentially shown in Figures 3.2(a), (b) and (c) for F1500, F2500 and F3500. The cell sizes decreases with increasing foam density as seen in Figure 3.2. It is also noted in Figure 3.2 cells are preferentially elongated through the R direction, but the cell sizes through the W and E directions are very similar (Figures 3.2(a), (b) and (c)). The foam samples show typical closed cell foam structure composing of 14-sided (tetrakaidecahedral) closed cells and each cell is composed of cell faces, edges and vertices (Figures 3.3(a) and (b)). Cell faces are the thin membranes that separate two adjacent cells; cell edges are relatively thick struts of intersection of three neighboring cells and cell vertices are the intersection of four neighboring cell edges. In a tetrakaidecahedral cell, there are 14 faces, 36 edges and 24 vertices and of 14 of cell faces are 8 regular hexagons and 4 squares. Figure 3.3(c) shows the SEM (Scaning Electron Microscopy) micrographs of cross-sections of the cells and Figure 3.3(d) is a magnified SEM micrograph near to the cell edge. The average cell face and edge thicknesses of each foams in E-W, R-W and R-E planes were

calculated using SEM micrographs taken from each specific planes and tabulated in Table 3.1.

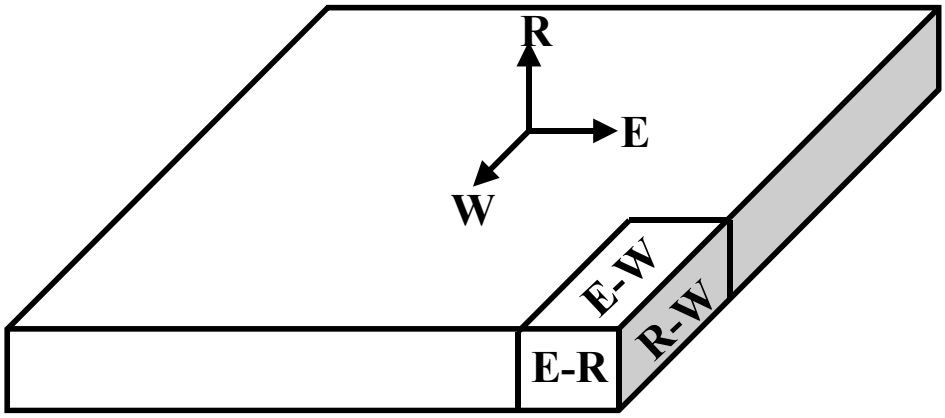

Figure 3.1 Schematic of as-received foam sheet showing R, W and E-directions and planes.

Table 3.1 Cell face and cell edge thickness through 3 planes.

Foam	**Cell face thickness (μm)**			**Cell edge thickness(μm)**		
	E-W	***R-W***	***R-E***	***E-W***	***R-W***	***R-W***
F1500	1.8	0.6	1.1	5.0	4.0	7.7
F2500	1.3	1.0	2.5	5.8	4.8	8.9
F3500	1.3	1.1	2.6	8.0	5.5	8.1

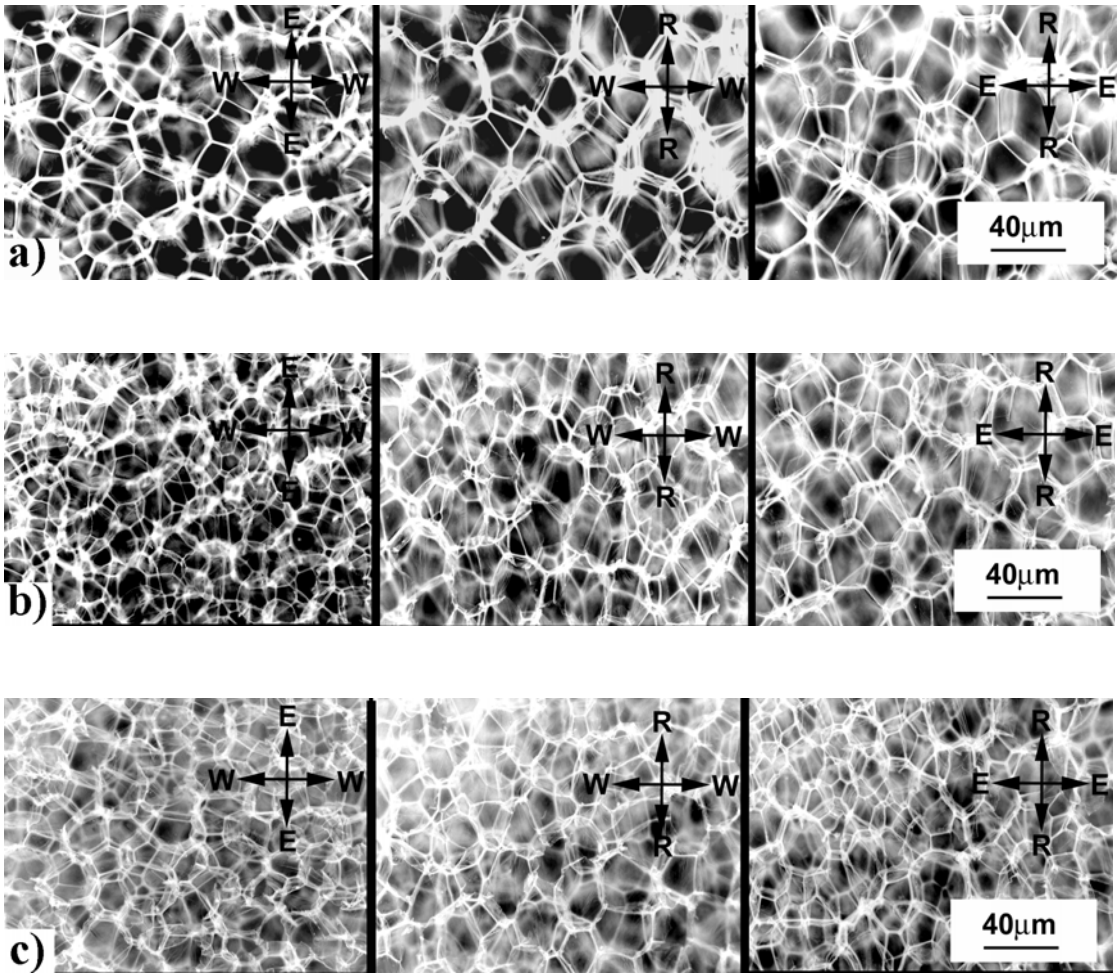

Figure 3.2 Inverted transmission optical microscope micrographs of cell structure in E-W R-W and E-R planes; a) F1500, b) F2500 and c) F3500.

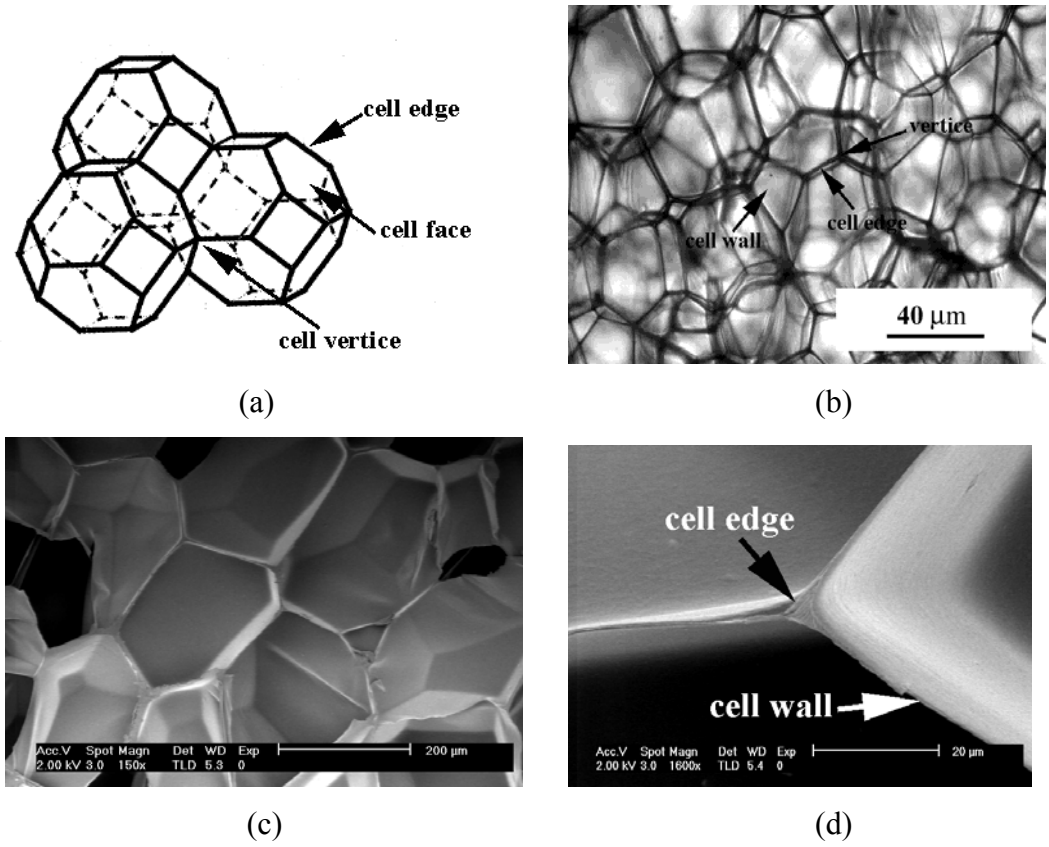

Figure 3.3 a) Tetrakaidecahedral foam model, b) transmitted optic and c) SEM micrographs of the cell wall and edges and vertices and d) SEM micrograph of the cell wall and edge.

In order to determine foam crushing behavior, compression tests were conducted on cubic samples (5x5x5 cm) prepared in accordance with ASTM D1621-91 [34] (Figure 3.4). Compression tests were conducted through (parallel) R-direction with cross-head speeds of 2.5, 8, 25 and 100 mm min^{-1}, corresponding to the strain rates of $8.33x10^{-4}$, $2.66x10^{-3}$, $8.33x10^{-3}$ and $3.33x10^{-2}$ s^{-1}, using a computer controlled SHIMADZU AG-I testing machine. In order to see the effect of cell anisotropy, compression tests at $8.33x10^{-4}$, $8.33x10^{-3}$ and $1.66x10^{-1}$ s^{-1} were also conducted through the W and E-direction. Besides conventional compression tests (Figure 3.5(a)), reloading and strain rate jumps test were also performed. The former was to determine the permanent strain and the later was to show the effect of strain rate on a deforming single foam sample by using cyclic test method. Number of the compression cycle is one and tests were stopped when the compression load reached the zero. In strain rate jump tests, initial strain rate was increased from $8.33x10^{-4}$ s^{-1} to $3.33x10^{-2}$ s^{-1} in order to investigate deformation rate effect. Few foam samples were tested through the R-direction inside a water-filled container in order to identify cell face and/or cell edge

tearing during deformation (Figure 3.5(b)). The deformation of the individual cells were observed in-situ under the transmission optical microscope on miniature compression test samples (5x5x5 mm), compressed with a micrometer until various strains (Figure 3.5(c)). Compression tests results were digitally recorded as load *vs.* displacement data, which were then converted into nominal stress *vs.* strain data. In few tests, the deformation sequence was also recorded using a video camera.

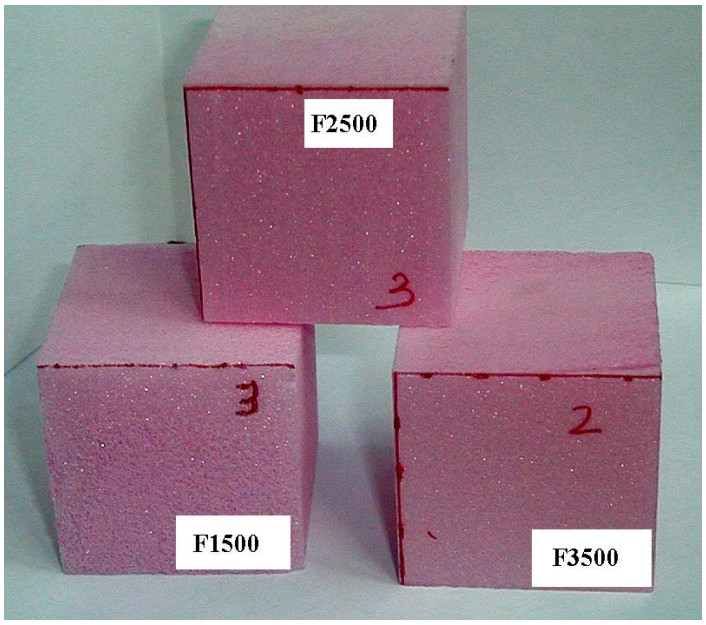

Figure 3.4 Cubic compression foam test samples.

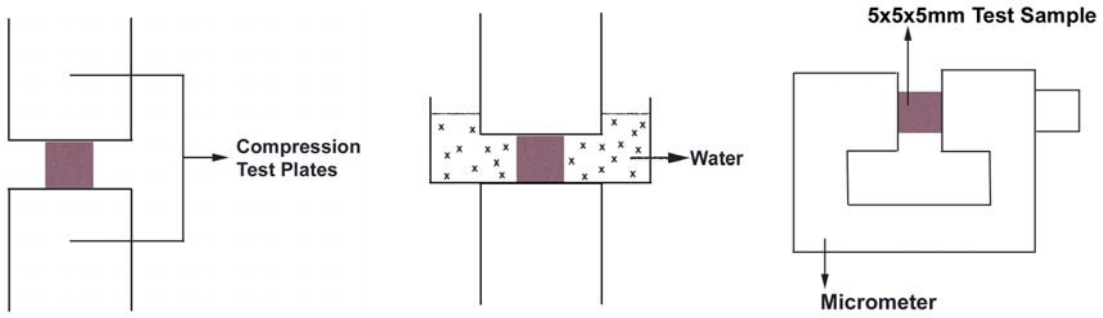

(a) (b) (c)

Figure 3.5 Compression test methods a) conventional, b) in-water and c) in-situ.

Scanning Electron Microscopy (SEM) samples of the deformed and undeformed foam specimens were prepared with a sharp blade following by inserting them inside a Nitrogen bath for few minutes. By this way, the extensive shearing of the cells, which prevented clear appearance of the cells under SEM, were avoided. SEM observations were conducted on the gold plated samples to reduce charging effect.

3.2 Cylindrical Empty and Foam-Filled Aluminum Tubes

Two different Al-tubes; 99.7% Al and 6063 Al, varying in diameter and thickness were investigated. Deep-drawn Al tubes were produced by METALUM Company of Turkey and received in two diameters, 16 and 25 mm, but nearly having the same wall thickness (0.22 and 0.29 mm). Commercially available 6063 Al tubes had an outer diameter of 19.8 mm and a wall thickness of 0.88 mm. In order to investigate the effect of wall thickness, the outer diameter of the tube was machined down to 0.5 and 0.3 mm.

The selection of the tube wall thickness and diameters are not arbitrary. Al empty tubes deformed in diamond, while foam-filled 25 mm diameter Al tube deformed in concertina and 16 mm diameter tube in diamond mode. Therefore, the strengthening effect of foam filling in both modes could be analyzed. 6063 Al empty tube of 0.88 mm thick deformed in concertina mode while 0.3 and 0.5 mm thick empty and filled-tubes deformed in diamond mode. These tubes were only tested in empty condition. The average crushing loads of these empty tubes were used for the fitting of the average crushing load of the Al-tubes as function of the D/t ratio. The geometrical parameters of the tubes are tabulated in Table 3.2.

The yield and ultimate strength of the tube materials were determined by uniaxial tensile tests conducted at a cross-head speed of 2.5 mm min^{-1}. Tension test specimens (Figure 3.6) were prepared according to ASTM B557M [35] (Appendix A). Since, the Al tubes of 16 and 25 mm diameter didn't have enough length to meet the required length of ASTM B557M standard, tension test specimens of these tubes were prepared in a quarter size of ASTM standard. Al thick sheets were bonded to the grip sections of these specimens in order to prevent the grip section from sliding.

Table 3.2 Tested tubes geometrical parameters.

Tube Material	Outer Diameter (mm)	Thickness (mm)	Length (mm)	D/t ratio
%99.7 Al	25.0	0.29	40	85
%99.7 Al	16.0	0.22	40	72
6063 Al	19.8	0.88	40	21
6063Al	19.0	0.5	40	37
6063 Al	18.6	0.3	40	61

Figure 3.6 Tension test specimen (6063 Al).

The stress (S) in tension test is calculated by dividing the load (P) by the cross-sectional area (A_0),

$$S = \frac{P}{A_0} \tag{3.1}$$

and the strain is calculated by dividing the elongation of the gage length of the specimen, ΔL, by its original length (L_0);

$$e = \frac{\Delta L}{L_0} = \frac{L - L_0}{L_0} \tag{3.2}$$

where, L is the final length of test specimen.

The Vickers hardness tests were also conducted to the cross-sections of the tubes. The test samples with length of 10 mm were cut from as-received tubes and mounted inside the polyester. The mounted samples were polished down to 1μm (Figure 3.7). Vickers Hardness tests were conducted using a Zwick/Roell ZHU 2.5 type Universal Hardness tester under 20 N load.

Figure 3.7 Metallographically prepared hardness test sample (6063 Al).

Preliminary compression tests were conducted on the empty tubes whether or not the length of the tube changed the deformation mode. Tubes with length of 10, 20, 30, 40 and 50 mm were tested and no change in deformation modes had been observed. However the shorter tubes formed only few folds. Since the thickness of the foam sheets were 50 mm, the length of empty tubes was chosen 40 mm so that maximum number folds were formed on the tube section. Tubes were machined to 40 mm in length using a diamond saw. Special cutting apparatus designed and machined in house was used to core-drill cylindrical foam samples that fitted tightly inside the tubes. The circular tubes with the lower edge sharpened was connected to the drilling machine by means of a mount as shown in Figure 3.8. Drilling was performed with a speed of 1400 turns per min. The outer diameter of the drilled foam samples was approximately equal to the inner diameter of the tubes; therefore, core-drilled samples were tightly fitted into the tubes.

Before foam filling, tubes were kept inside an acetone bath for ten minutes to clean the inner surface of the tubes. A Bison Styrabond® polystyrene adhesive was used to bind the foam filler to the tube wall. The adhesive was spread on the tube wall and then the foam filler was inserted. The excessive adhesive was removed after filler insertion. Foam filled tubes with adhesive were kept 48 hours at room temperature before they were compressed. Most of the filled tubes were compressed with adhesive while limited numbers of tests were conducted without adhesive in order to see the effect of the adhesive. Few filled samples with an epoxy-based adhesive were also compressed to analyze the effect of adhesive strength on the crushing behavior of the filled tubes.

Figure 3.8 Apparatus used to core-drill cylindrical foam filler.

Empty and foam filled tubes were compressed with four different cross-head speeds; 2.5, 8, 25 and 100 mm min^{-1}. The corresponding deformation rates, which is defined as the cross-head speed divided by the initial length of the tube, were $1.04x10^{-4}$, $3.33x10^{-3}$, $1.04x10^{-2}$ and $4.16x10^{-1}$ s^{-1}. The compression tests were conducted between the tool steel plates (Figure 3.9) with a lubricant between tube ends and compression plates.

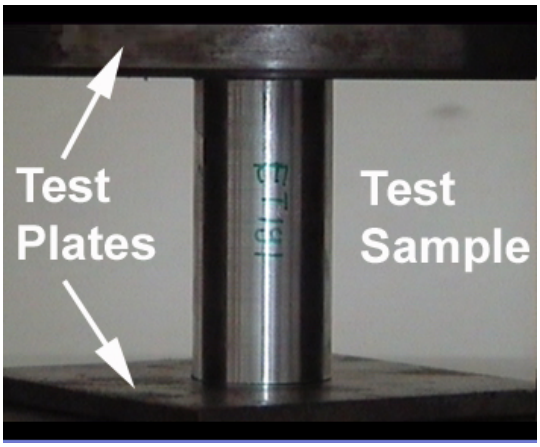

Figure 3.9 View of an empty Al tube between the compression test plates.

Chapter IV

RESULTS

4.1 Compression Behavior of the Filler

Tested foam samples showed a typical stress-strain behavior of cellular structures. The stress-strain curve consisted of three distinct regions; linear elastic, plateau and densification region, as depicted in Figure 4.1. In elastic region, stress increased linearly with the strain until a peak or maximum stress, which was followed by a plateau region. The peak stress, referred as to collapse stress, was found in all tested samples. The plateau region continued until the densification strain and thereafter stress increased sharply. In all tested samples, there was a certain level of permanent strain, proving the elasto-plastic nature of the foams.

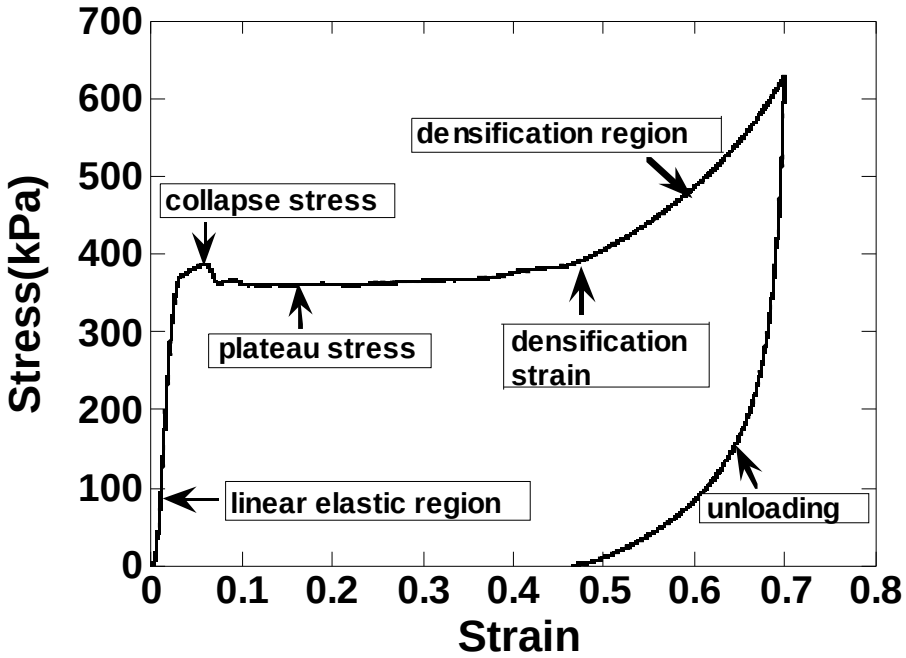

Figure 4.1 Typical stress-strain curve of the tested foam (F3500, 8.33×10^{-4} s^{-1}) showing three distinct deformation regions and unloading behavior.

Typical compressive stress-strain curves of the foams tested through the R, E and W-direction at $8.33 \times 10^{-4} s^{-1}$ are shown sequentially in Figures 4.2(a), (b) and (c) for F1500, F2500 and F3500. Although, compression behavior through the E and W-direction are very similar for each foam density, the foam shows higher compressive stresses through the R-direction. The difference in the compressive stress between R

and W or E-direction is also noted to increase with increasing foam density, while it decreases with increasing strain.

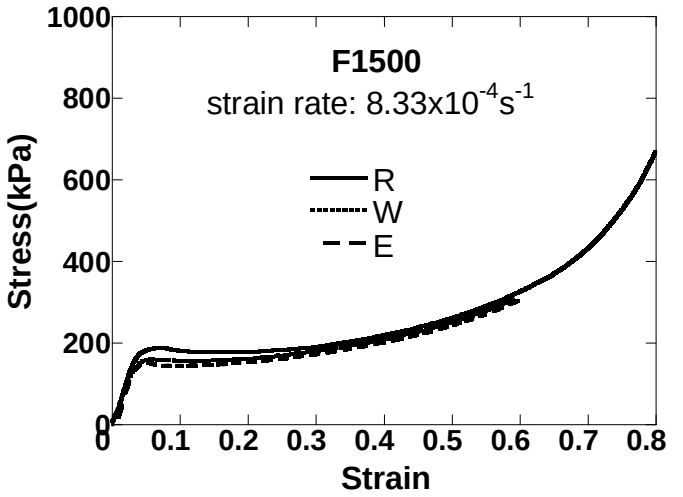

(a)

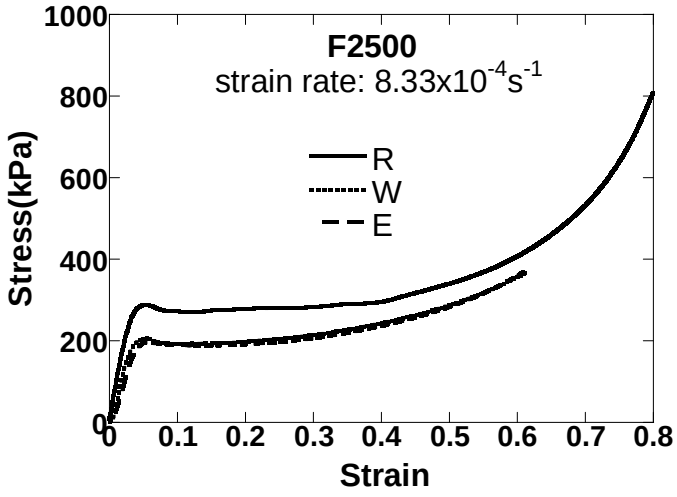

(b)

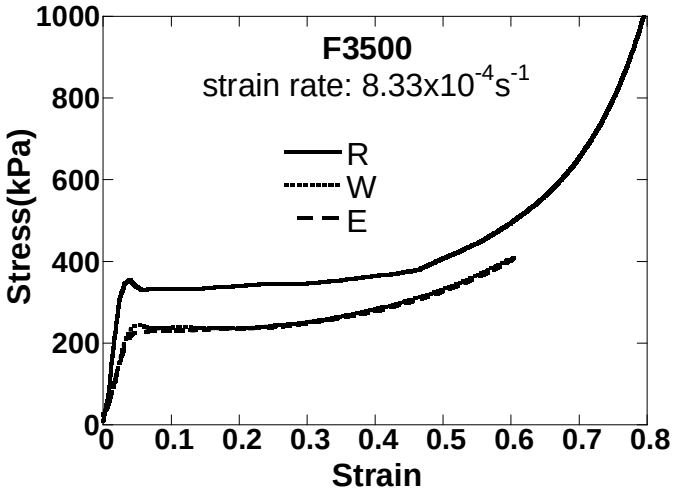

(c)

Figure 4.2 Stress-strain curves of the foam tested through R, E and W-direction at $8.33x10^{-4}$ s^{-1}; a) F1500, b) F2500 and c) F3500.

The effect of foam density on the compression behavior in each test direction is sequentially shown in Figures 4.3(a), (b) and (c) for R, W and E-direction.

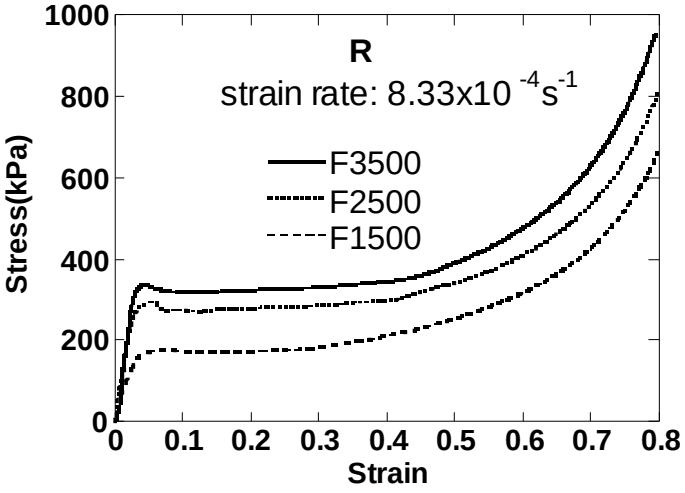

(a)

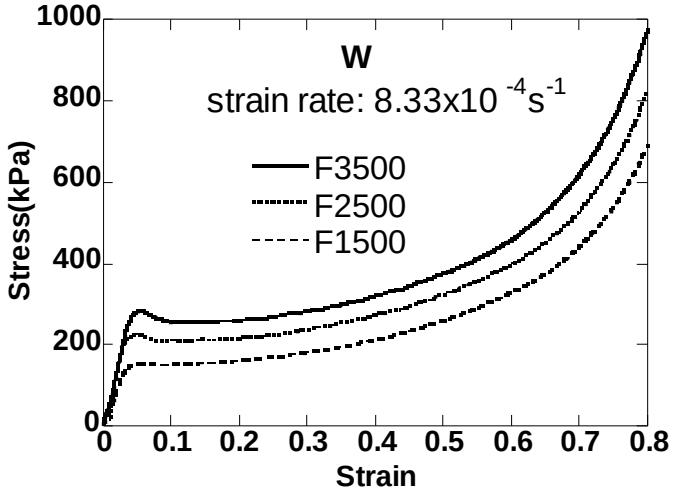

(b)

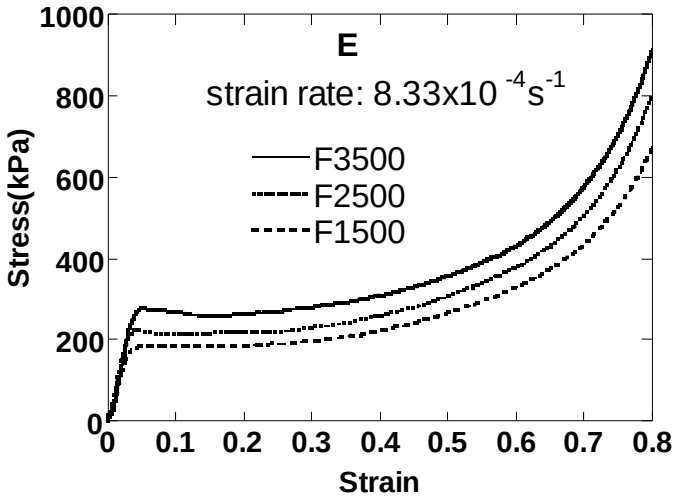

(c)

Figure 4.3 Effect of foam density on the stress-strain curves of the foam tested through a) R, b) W and c) E-direction at $8.33x10^{-4}$ s^{-1}.

The studied foam compression stress-strain curves are strain rate sensitive as shown in Figures 4.4(a), (b) and (c) sequentially for F1500, F2500 and F3500 at various quasi-static strain rates.

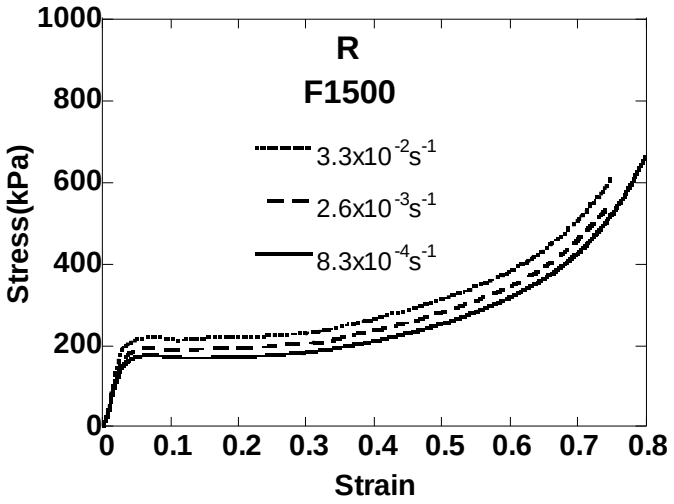

(a)

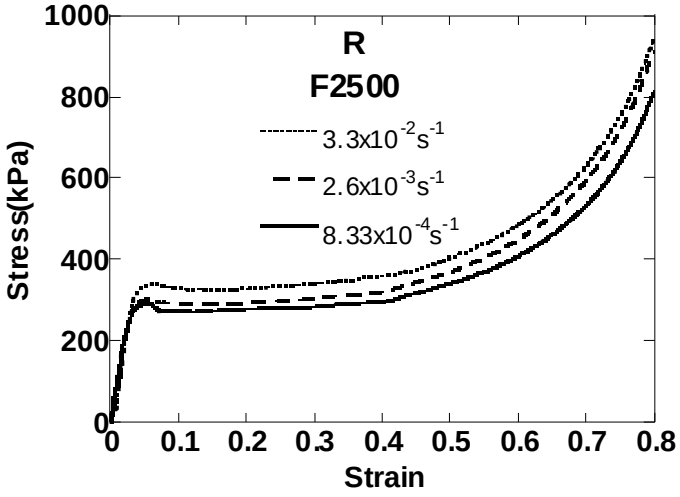

(b)

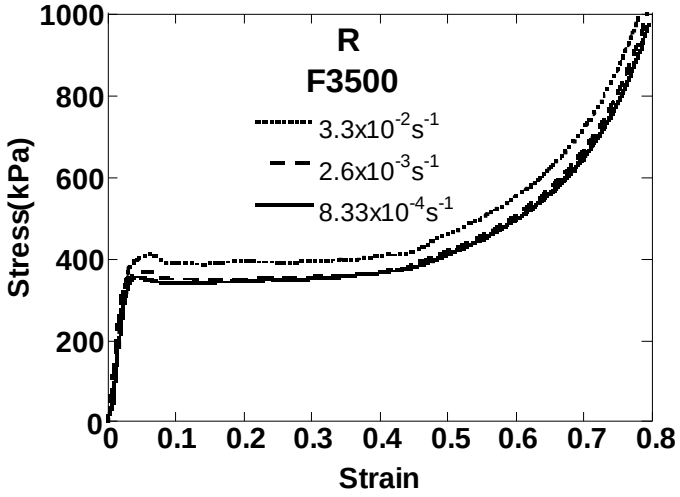

(c)

Figure 4.4 Effect of strain rate on the stress-strain curves of the foams tested through the R-direction a) F1500, b) F2500 and c) F3500.

The strain rate sensitivity of the foams was also confirmed by strain rate jump tests. In a typical jump test strain rate was increased to a higher value in the plateau and or in the densification regions as shown in Figures 4.5(a) and (b).

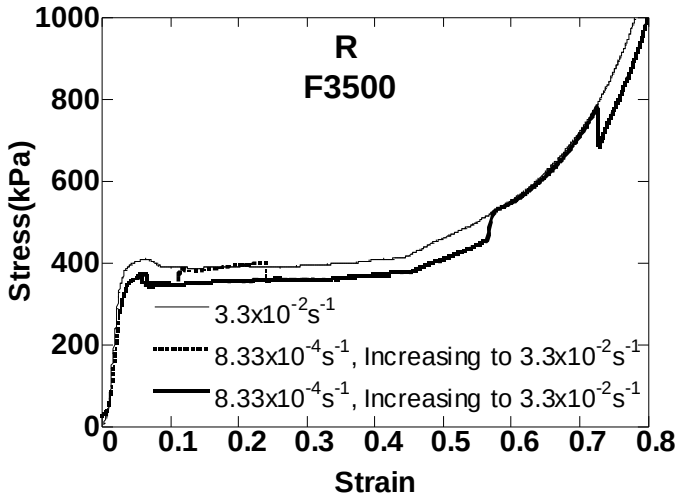

(a)

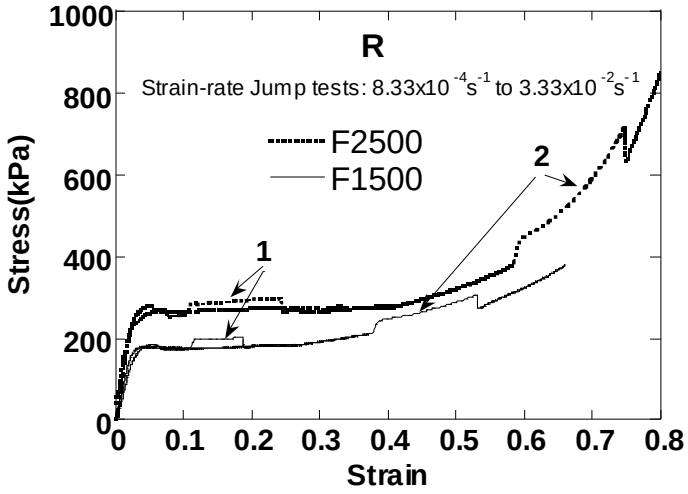

(b)

Figure 4.5 Strain rate jump tests; a) F3500 and b) F2500 and F1500, 1: plateau region, 2: densification region.

Figures 4.6(a) and (b) show the variation of the plateau and collapse stresses at $8.33x10^{-4}s^{-1}$ as function of foam relative density through R, W and E-direction. The data in these figures were fitted with following power-law type hardening relation,

$$\sigma = K\left(\frac{\rho^*}{\rho_s}\right)^n \tag{4.1}$$

where σ and $\frac{\rho^*}{\rho_s}$ are the stress (plateau (σ_p) or collapse (σ_c)) and foam relative density respectively and K and n are the constants. It is noted that the value of the n in the R

direction (1.6) is greater than those in W and E-directions (1 and 1.2), showing a more pronounced density dependence of the plateau and collapse stresses in the R-direction.

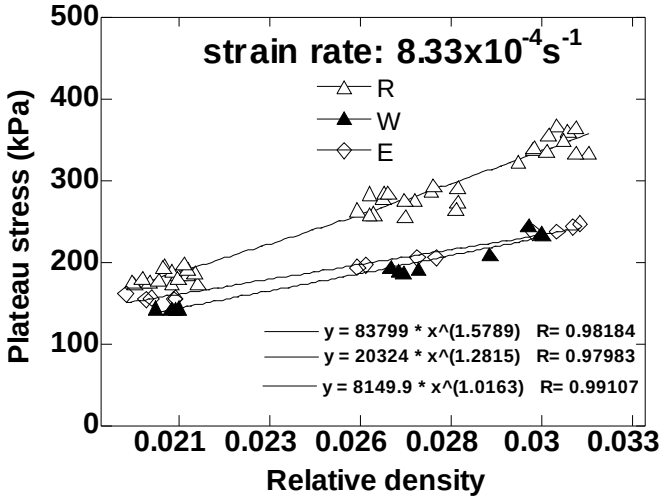

(a)

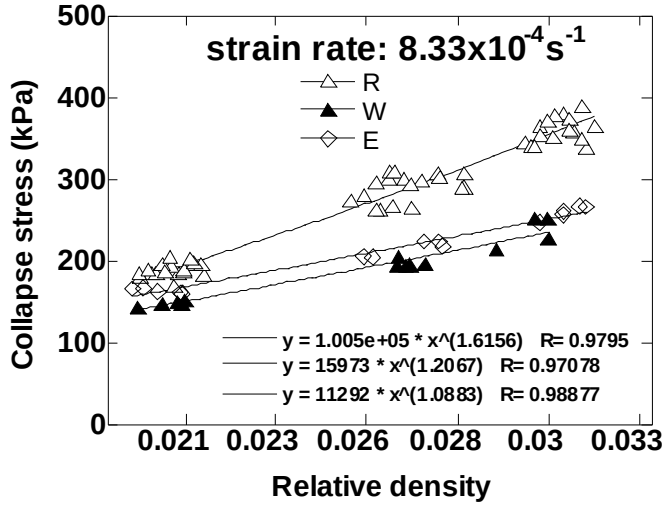

(b)

Figure 4.6 Variation of the foam a) plateau and b) collapse stress with the foam relative density at 8.33×10^{-4} s^{-1}.

The variation of the plateau stress as function of strain rate in R and W-direction are shown sequentially in Figures 4.7(a) and (b). The strain rate sensitivity of the foams (k) was found by fitting the plateau stress data with the following power-law type hardening equation,

$$\sigma(\dot{\varepsilon}) = \sigma \dot{\varepsilon}^{k} \tag{4.2}$$

where σ and $\dot{\varepsilon}$ are the stress at reference strain rate (1 s^{-1}) and strain rate, respectively. The strain rate sensitivity parameter of the foam within the studies quasi-static strain rate regime is found to be independent of the foam density and the testing direction and equals to nearly 0.04.

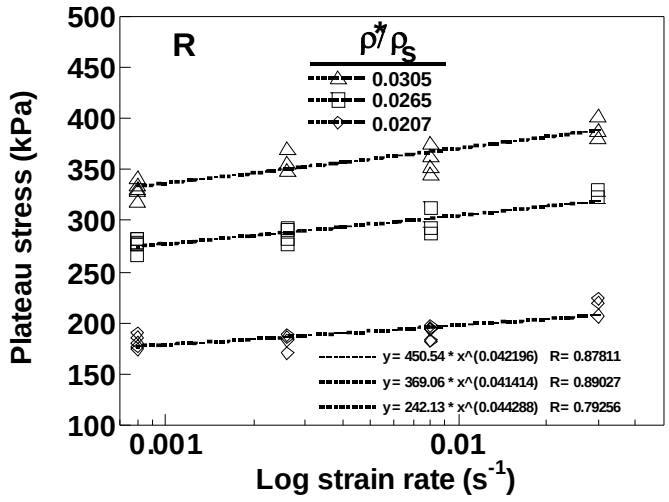

(a)

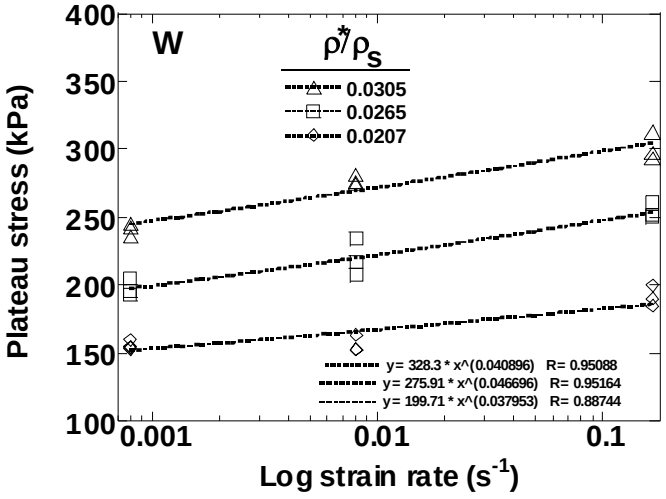

(b)

Figure 4.7 Plateau stress as function of strain rate, a) R and b) W-directions.

The elasto-plastic foam stress-strain behavior is usually fitted with the gas-pressure hardening equation [36, 37],

$$\sigma = \sigma_c + \frac{P_o \varepsilon}{1 - \varepsilon - \frac{\rho^*}{\rho_s}} \tag{4.3}$$

where P_o is the initial gas pressure of the foam cells. In all foam samples tested, the compressive stress versus gas pressure strain ratio ($1-\varepsilon-\rho^*/\rho_s$) curves showed two linear regions but with different slopes as shown in Figures 4.8(a), (b) and (c) for the foams tested normal to the R-direction. In the first linear region the slope is lower than 100 kPa (initial air pressure), while in the second region it is higher than the initial air pressure. Since a linear relationship between stress and gas pressure strain ratio existed, the stress-strain curve corresponding to the lowest strain rate (8.33×10^{-4} s^{-1}) were fitted with the following equations corresponding regions 1, 2 and 3:

$$0 < \varepsilon < \varepsilon_1 \qquad \sigma = E\varepsilon \tag{4.4}$$

$$\varepsilon_1 < \varepsilon < \varepsilon_2 \qquad \sigma = \sigma_{o1} + S_1 \frac{\varepsilon}{1 - \varepsilon - \frac{\rho^*}{\rho_s}} \tag{4.5}$$

$$\varepsilon_2 < \varepsilon < 0.85 \qquad \sigma = \sigma_{o2} + S_2 \frac{\varepsilon}{1 - \varepsilon - \frac{\rho^*}{\rho_s}} \tag{4.6}$$

where S_1 and S_2 are the slopes of the linear curves in region 2 and 3, respectively. Equation 4.4 is for the elastic response of the foam. The parameters of the Equations 4.4, 4.5 and 4.6 were first determined for the compression stress-curve at the lowest strain rate (8.33×10^{-4} s^{-1}) and then using Equation 4.2, the parameters were determined for the reference strain rate (1 s^{-1}).

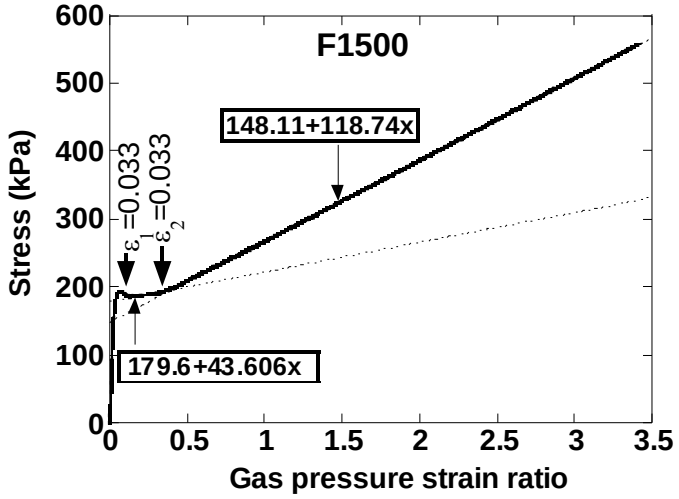

(a)

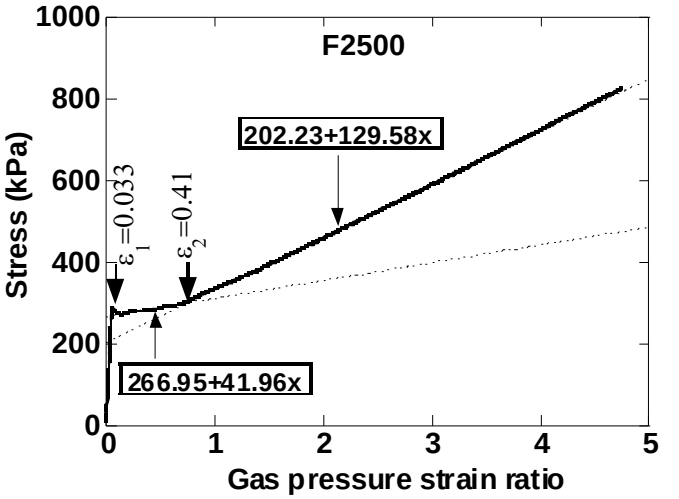

(b)

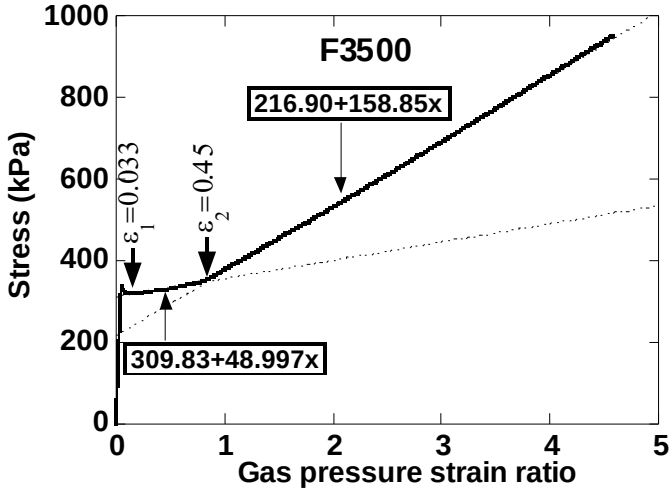

(c)

Figure 4.8 Stress *vs.* gas pressure strain ratio at 8.33×10^{-4} s^{-1}, a) F1500, b) F2500 and c) F3500.

The parameters of the Equations 4.4, 4.5 and 4.6 for reference strain rate are tabulated in Table 4.1 and 4.2 for R and W-direction, respectively. The stress-strain curves of the foams were then predicted at any strain rate interested within the studied strain rate regime.

Table 4.1 Parameters of Equations 4.4, 4.5 and 4.6 at reference strain rate of $1s^{-1}$ for the foam tested through the R-direction.

Foam	ε_1	ε_2	**E (kPa)**	σ_{o1} **(kPa)**	σ_{o2} **(kPa)**	S_1 **(kPa)**	S_2 **(kPa)**	**K**
F1500	0.033	0.30	7790	254.83	203.69	69.332	188.79	0.0443
F2500	0.033	0.41	10925	358.03	271.23	56.276	173.79	0.0414
F3500	0.033	0.45	12791	417.90	292.56	66.051	214.25	0.0422

Table 4.2 Parameters of Equations 4.4, 4.5 and 4.6 at reference strain rate of $1s^{-1}$ for the foam tested through the W-direction.

Foam	ε_1	ε_2	**E (kPa)**	σ_{o1} **(kPa)**	σ_{o2} **(kPa)**	S_1 **(kPa)**	S_2 **(kPa)**	**K**
F1500	0.05	0.2	2813	158	129.73	39.467	107.47	0.038
F2500	0.04	0.2	4643	195	169.67	41.289	127.51	0.046
F3500	0.03	0.2	7921	238	191.74	42.805	138.85	0.041

Figure 4.9(a) shows the predicted and experimental stress-strain curves of the F3500 and F1500 foams in the R-direction at various strain rates. Also Figure 4.9(b) shows the predicted stress-strain curves at $8.33x10^{-4}$ and $3.33x10^{-2}$ s^{-1} and experimental strain rate jump tests in the W-direction. Note that in the calculations, a strain rate sensitivity parameter independent of the strain was assumed. This gave small discrepancy between predicted and experimental stress-strain values at relatively lower and higher strains (>70%).

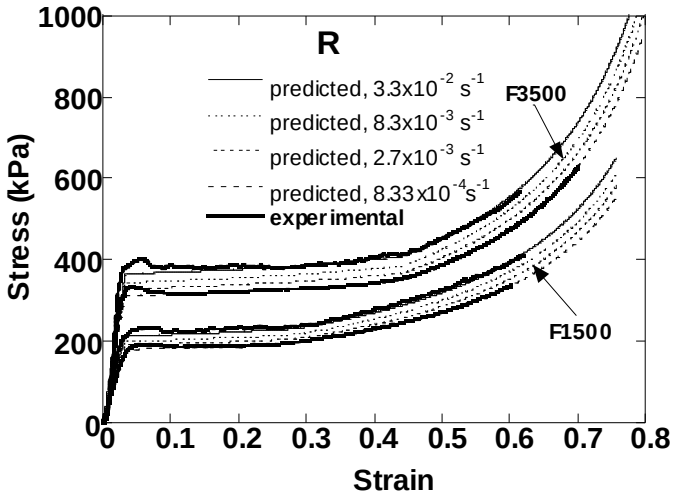

(a)

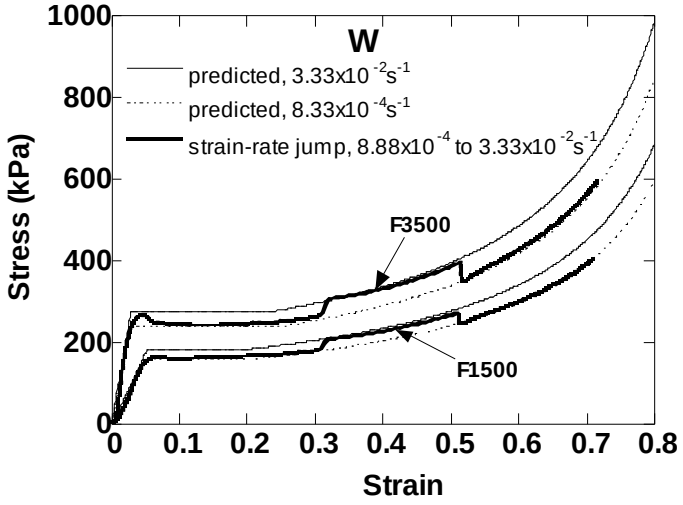

(b)

Figure 4.9 Comparison of experimental and predicted stress-strain curves of foam tested through the a) R and b) W-direction.

4.2 Deformation Mechanism of the Filler

All tested foam samples formed deformation band, usually triggered in the mid-section of the cubic sample. This was attributed to the variation in the cell-edge length and thickness and cell face thickness of the foam through the thickness of the as-received foam plates. Since the foam was extruded normal to its thickness, higher compressive stresses were likely to form near the skin, resulting in shorter but thicker cell edges and cell faces. In few samples, the skin layers, which was assumed to be 1cm thick, were removed and compression tests on these samples showed insignificant differences in the plateau regions of the stress-strain curves between with and without

skin layer samples (Figure 4.10). Following the plateau region, the stress raised more steeply in the samples with skin layer, especially in F3500 and F2500, proving that cell morphology was relatively more homogenous in F1500 as compared with F3500 and F2500. The effect of skin, however in the W and E directions was found to be significant and therefore, the skin layer was removed in these samples before compression testing.

The micrographs of in-water compressed tests samples until about 0.1, 0.2, 0.5 and 0.8 strains are shown sequentially in Figures 4.11(a), (b) and (c) for the F1500, F2500 and F3500 through the R-direction. It was observed that as soon as deformation band initiated in the mid-section, the air bubbles formed and escaped from the surface of the deformation band, proving the tearing of the cell-faces and/or cell edges. The deformation band started only after 0.1 strain in F1500, between 0.05 and 0.1 in F3500 and F2500. As the strain increased the deformation band proceeded to the plastically undeformed regions of the sample. The intensity of air bubble formation was observed to decline as the band proceeded through the skin of the foam sample.

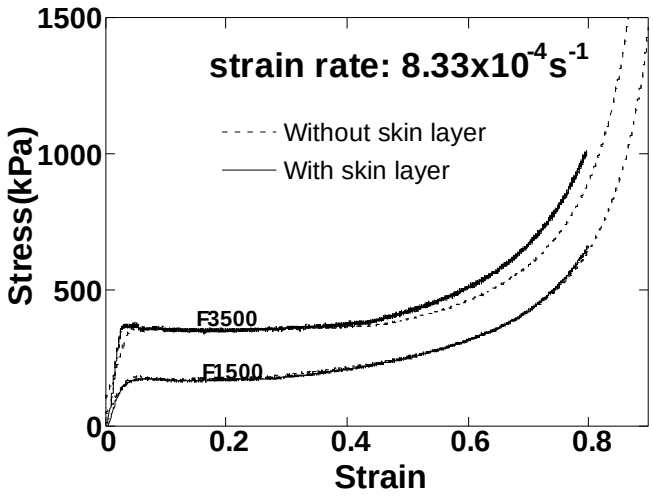

Figure 4.10 The effect skin layer on the stress-strain curves of F1500 and F3500.

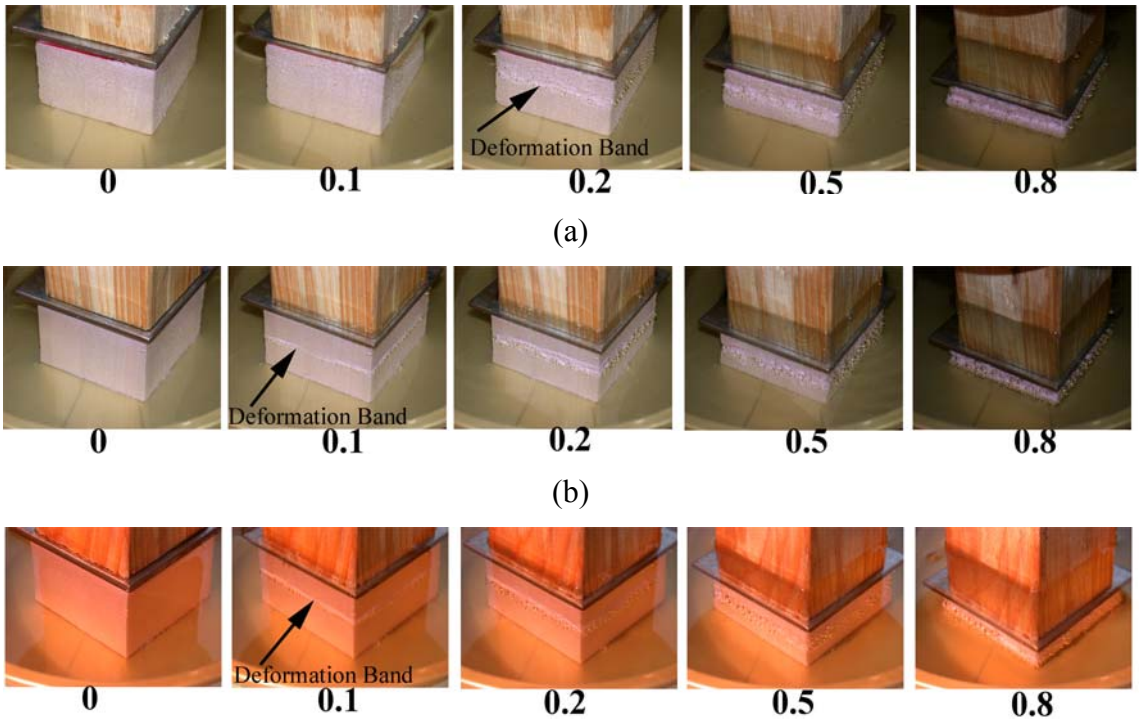

Figure 4.11 Deformation micrographs of in-water compressed foam samples test at various strains; a) F1500, b) F2500 and c) F3500.

Figures 4.12(a-d) are the micrographs of the F1500 miniature test sample compressed between 0-30% strain. As the sample compressed, cell edges started to buckle, see cell A in Figure 4.12(b). Cell edge buckling was observed to occur at relatively thin cell edges. Further deformation resulted in folding of the cell edge (Figure 4.12(d)) and cell face as well (marked by arrow in Figure 4.12(d)). The deformation band development sequence in F2500 sample is shown in Figures 4.13(a-c). It was found that local cell edge buckling lead to formation of the deformation band, which propagated through undeformed sections. The deformation within the band was assumed to reach the densification strain.

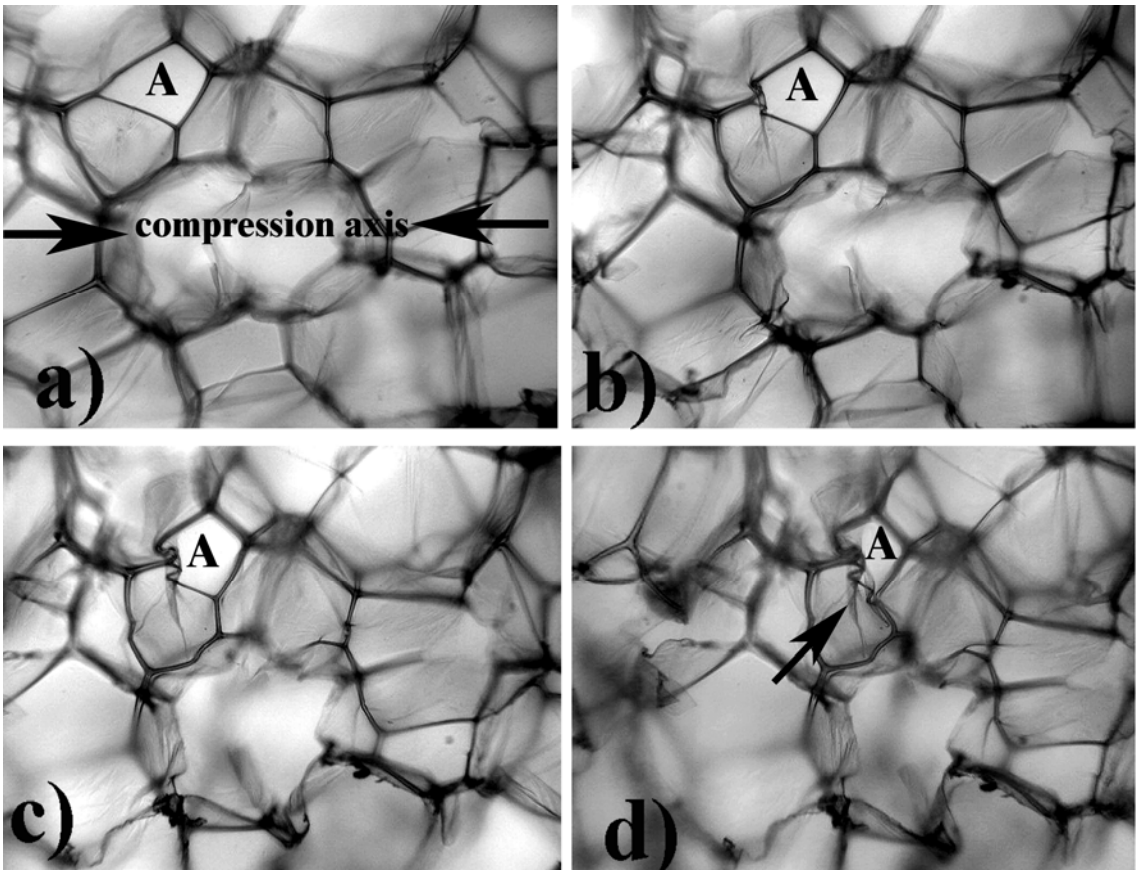

Figure 4.12 In-situ micrographs of F1500 deformation, a) 0%, b) 7% ,c) 22% and d) 29% strains.

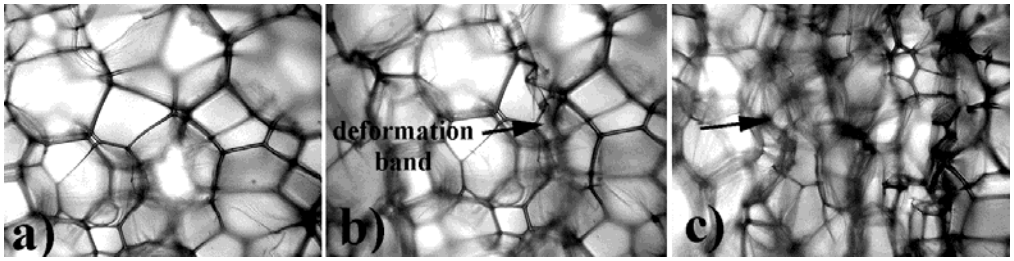

Figure 4.13 Development of deformation band in F2500 a) 0%, b) 16%, and c) 29% strains.

Figures 4.14(a) and (b) show two distinct deformation modes in the F3500 sample. In the mid-section the cell faces were folded with no significant cell stretching through the normal to the compression axis (Figure 4.14(a)). In contrast to this, the cells near to the skin were mostly stretched normal to the compression axis (Figure 4.14(b)). This was in consistent with the observations of the air evolution in-water compressed foam samples; the air evolution was faster in the mid-section, while its

evolution was reduced as the deformation proceeded through the skin layer. It is proposed that in mid-section the cell faces were torn and therefore the cells did not stretched normal to the compression axis. But as the band moves from the mid-section cell stretching become dominant deformation mode because of the thicker cell faces.

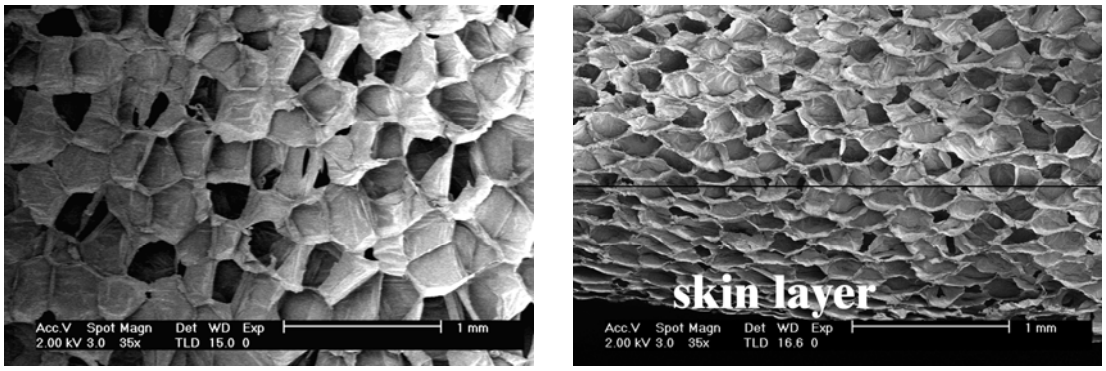

(a) (b)

Figure 4.14 SEM micrographs of deformed F3500 showing a) cell face folds inside the cells and b) cell stretching through the normal to the compression axis near to the skin layer.

4.3 Tensile Properties of the Tube Materials

The tensile stress-strain curves of the Al and 6063 Al tube materials are shown in Figure 4.15. The ultimate tensile stress (UTS), $\sigma_{U,}$ 0.2% proof strength, $\sigma_{0.2}$, and Vickers hardness number of the tube materials are listed in Table 4.3. 6063 Al has higher UTS and 0.2% proof strength and hardness number than 99.7% Al.

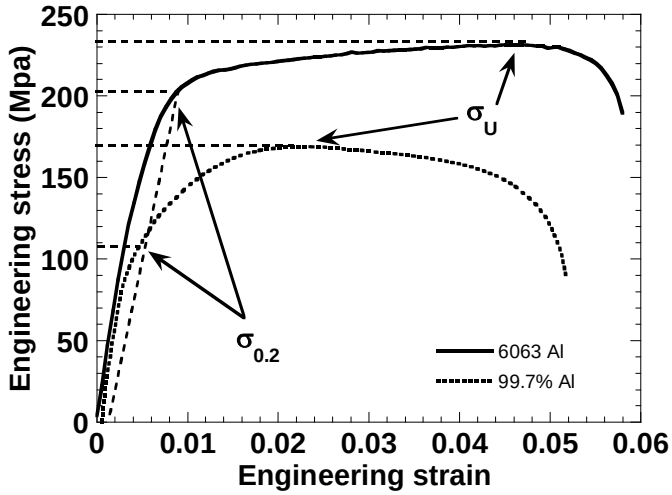

Figure 4.15 Tensile stress-strain curves of 6063 Al and 99.7% Al tube material.

Table 4.3 Mechanical properties of 6063 Al and 99.7% Al (average of at least 3 tests).

Materials	**σ_U ($\pm$ 10 MPa)**	**$\sigma_{0.2}$ ($\pm$ 10 MPa)**	**σ_0 $(\frac{\sigma_{0.2}+\sigma_U}{2})$**	**Vickers hardness number**
99.7% Al	170	105	137.5	58
6063 Al	241	205	223	80

4.4 Compression Deformation Behavior of the Empty And Foam Filled Tubes

4.4.1 Crushing Behavior of the Empty And Foam Filled Al Tubes

Empty Al tubes, both 16 and 25 mm, deformed in diamond mode. Typical load-displacement curves of the tubes are shown in Figure 4.16. The distance between the peaks loads numbered in Figure 4.16, is the fold length and the total number of peaks corresponds to the number of the folds formed in the tubes. The total number of the folds is 9-10 and 7-8 in 16 and 25 mm tube, respectively. The densification of tubes, the sudden rise in load values, starts after 32 mm displacement, corresponding to about 80% of the initial tube length. The higher load values in 25 mm diameter tube is due to the larger diameter and thicker tube wall.

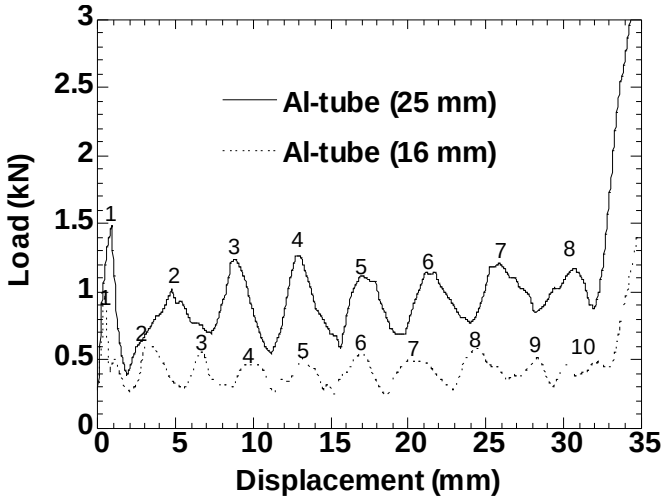

Figure 4.16 Typical load *vs.* displacement curves of the empty Al tubes at 2.5 mm min^{-1}.

The progression of the diamond folding in 16 mm Al tube is shown sequentially in Figures 4.17(a), (b) and (c) for the displacements of 5, 10 and 20 mm. Inward and outward folds seen in this figure prove the complex deformation mode of the Al tubes. The number of folds can be however counted easily; for example Figure 4.17(a) shows 2 diamond folds, Figure 4.17(b) 4 folds and Figure 4.17(c) 6 folds. The top and bottom views of the partially crushed 16mm tube sample are shown in Figures 4.18(a) and (b). The folds are six-cornered as numbered in Figure 4.18(a). The six-corner diamond folding geometry, given by S. R. Guillow *et al.* [38] and schematically shown in Figure 4.18(c), consists of 3 circumferential folds.

(a) (b) (c)

Figure 4.17 Cross-sections of the deformed 16 mm diameter Al-tube (2.5 mm min^{-1}) displacements: a)5 mm (2-diamond folds), b)10 mm (4-diamond folds) and c)20 mm (6-diamond folds).

(a) (b) (c)

Figure 4.18 a) Top and b)bottom views of the crushed 16 mm Al tube and c)schematic view of the diamond collapse mode with 3 circumferential lobes (only figure 4.18(c),[38]).

Although the first fold formation in 25 mm tube was axisymmetric, the deformation proceeded in diamond mode with 8 corners per fold (Figures 4.19(a), (b) and (c). A similar deformation behavior was also previously observed in empty Al tubes and it was due to the influence of the axisymmetric trigger on the first fold [39].

(a) (b) (c)

Figure 4.19 a) Top and b) bottom views of the crushed 25 mm Al tube and c) schematic of the diamond collapse mode with 4 circumferential lobes (only figure 4.19(c),[38]).

Few of the samples also deformed in mixed mode. In these samples the first couple of the folds formed in axisymmetric mode then the deformation was turned into diamond mode. Typical load-displacement curves the samples deformed in mixed mode and the photographs of the samples deformed in diamond and mixed mode are shown sequentially in Figures 4.20 (a) and (b).

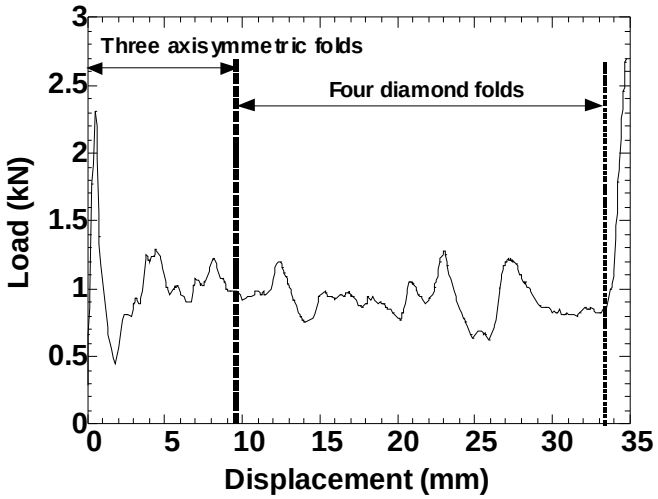

(a)

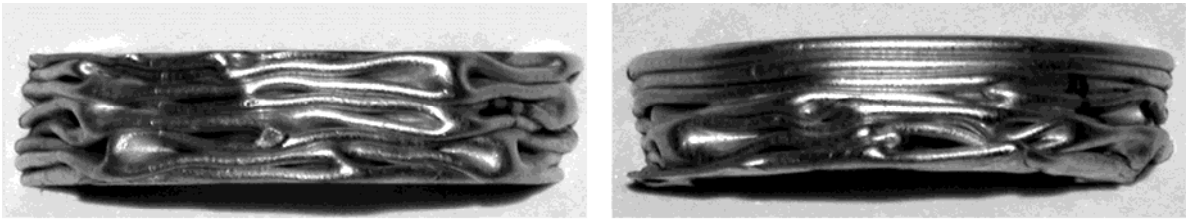

(b)

Figure 4.20 a) Load-displacement curve of the 25 mm tube deformed in mixed mode and b) side views of the samples deformed in diamond and mixed mode.

6063 Al empty tubes of 0.3 and 0.5 mm thick deformed in diamond mode (N=3) while 0.88 mm thick tube in concertina mode. The load-displacement curves of the tubes are shown in Figure 4.21. In 0.3 mm thick tube, totally 6-7 diamond folds formed, but as the thickness increased to 0.5mm the number of folds decreased to 5-6. It was also observed that in 0.5 mm thick tube the first fold formed in axisymmetric mode. In 0.88 mm thick tube the number of folds was found 4-5.

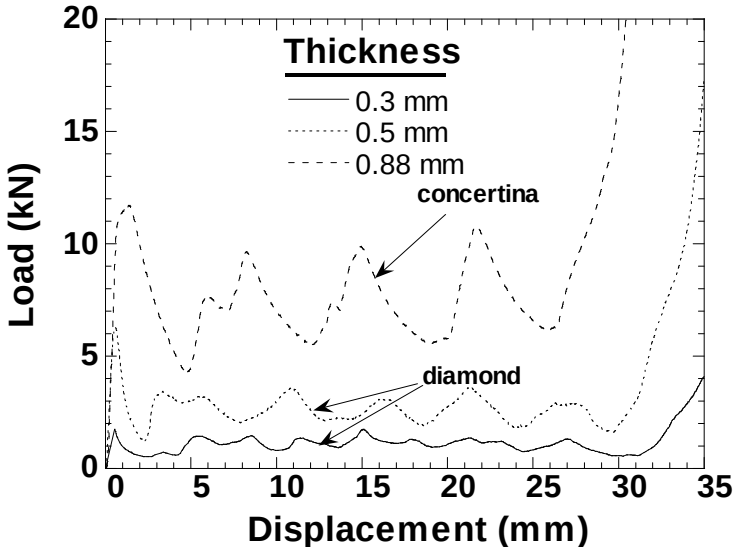

Figure 4.21 Load-displacement curves of the 6063 Al tubes (2.5 mm min^{-1}).

The deformation mode of the foam-filled 16 mm Al tube remained to be the same with that of the empty tube. Figure 4.22 shows the typical load-displacement curves of the foam-filled and empty tube and the effect of foam filling on the deformation behavior of 16 mm tube. Foam filling increased the load values, reduced the fold length; hence, increased the number of folds formed and resulted in shifting of the densification region to lower values of the displacement. The effect of increasing foam density was to increase the load values and lower the densification point (Figure 4.22).

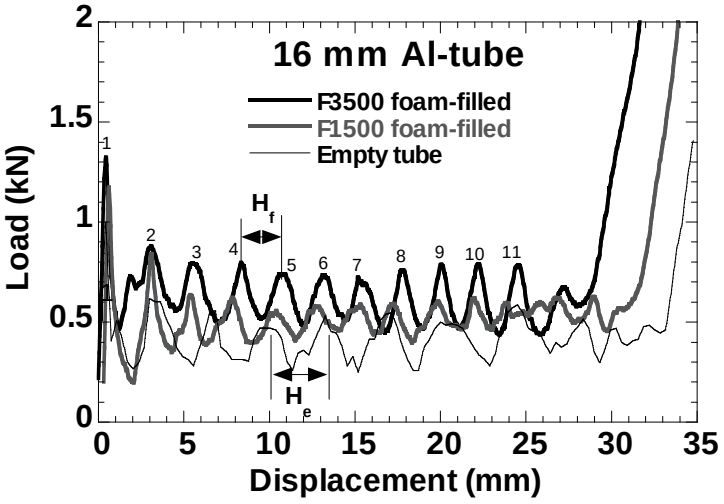

Figure 4.22 Load-displacement curves of the foam-filled and empty Al-tube (16 mm) at 2.5 mm min^{-1}.

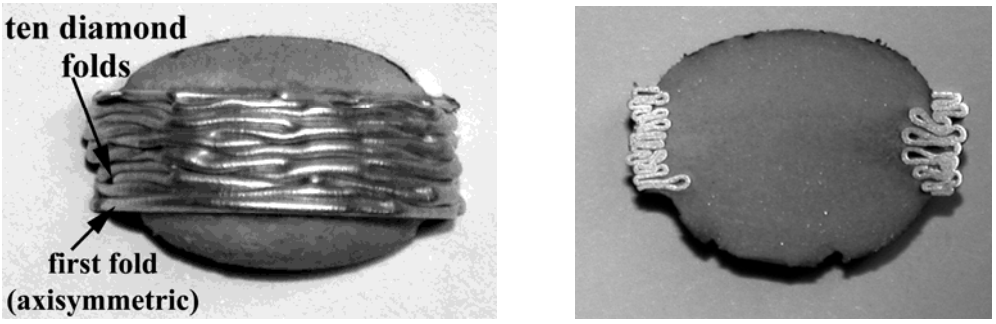

(a) (b)

Figure 4.23 a) Side-view of F1500 filled and b) interior of F3500 filled 16 mm Al tube (2.5 mm min^{-1}).

In foam-filled 16 mm tubes, the first fold usually formed in axisymmetric mode, but the deformation proceeded in diamond mode and totally 10-12 folds are formed in foam filled tube regardless of the foam density (Figure 4.23(a)). It was also noted that the elastic recovery of the foam filler was prevented by the tube wall due to the entrance of the foam in between the folds (Figure 4.23(b)).

For the studied foam densities, the foam filling of 25 mm Al tube resulted in change of deformation from diamond to concertina mode, see Figure 4.24(a) and (b). Few of the F1500 foam filled tube samples also deformed in mixed mode (Figures 4.25(a) and (b)). In concertina mode of deformation the foam filler elastically recovered after crushing; part of the foam remained to be attached to crushed tube wall, resulting in tearing of the filler (Figure 4.24(a)). But, in mixed mode, the recovery of the foam again prevented by the tube wall, because of the foam entrance in between the folds as shown in Figure 4.25(b).

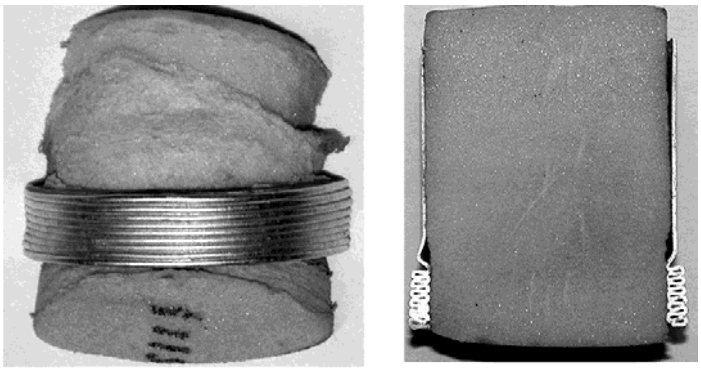

(a) (b)

Figure 4.24 Crushed F3500 foam-filled 25 mm Al tube (2.5 mm min^{-1}), a)side and b) interior.

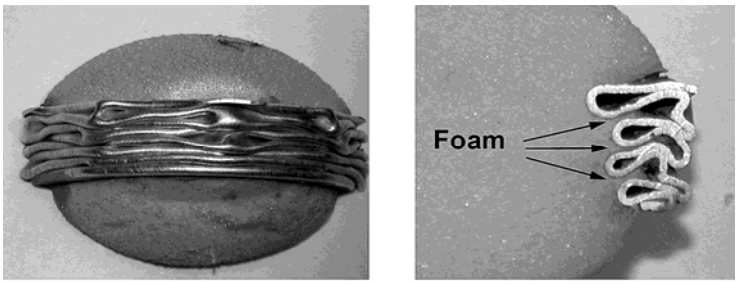

(a) (b)

Figure 4.25 Mixed deformation mode in 25 mm F1500 foam-filled Al tube, a) side and b) interior, near to the tube wall (2.5 mm min^{-1}).

The effect of foam filling on the load-displacement behavior of 25 mm Al tube, as in the case of 16 mm tube, was to increase of the load values, reduce fold length; hence, increase the number of the folds and lower the densification point (Figure 4.26). Increasing foam density increases the load values but also slightly lowers the densification point.

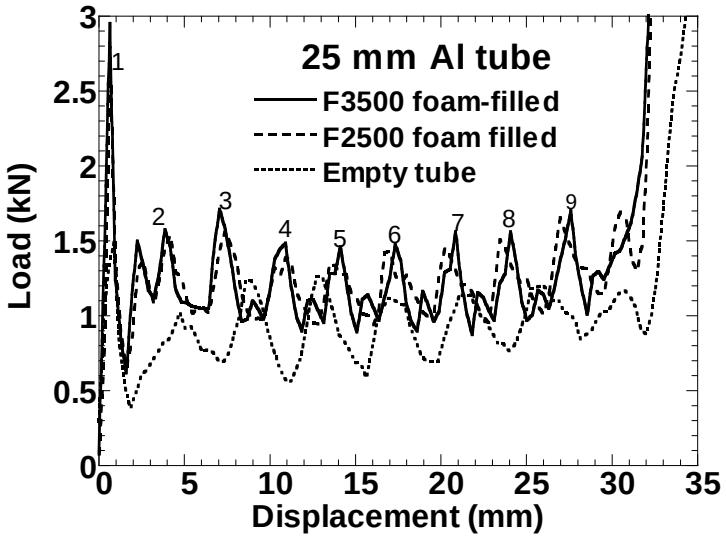

Figure 4.26 Load-displacement curves of the foam-filled and empty Al-tube (25 mm) at 2.5 mm min^{-1}.

Figure 4.27 shows the comparison of the load-displacement curves of the concertina and mixed mode of deformation in foam filled 25 mm Al tube. Compared to concertina mode, the fold length increases and hence number of folds decreases in the mixed mode. It is also noted in Figure 4.27, in both modes densification starts at the same displacement.

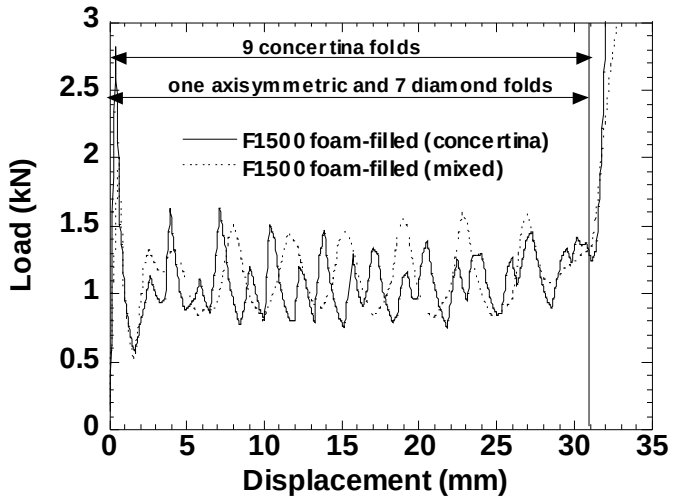

Figure 4.27 Load-displacement curves of the concertina and mixed mode of deformation in F1500 foam-filled 25 mm Al tube at 2.5 mm min^{-1}.

The effect of deformation or crushing rate, which is expressed as the displacement rate divided by the initial tube length, on the load-displacement curves of the empty and foam filled tubes are shown in Figures 4.28(a)-(d) for 16mm Al tube. There is a slight or negligible effect of deformation rate on the crushing load of empty tube. In foam filled tube, the effect of increasing deformation rate is to rise the load values, mainly due to the strain rate dependent compressive flow stress of the filler. A similar effect of deformation rate on the load-displacement behavior of the 25 mm empty and foam-filled Al tube was also found.

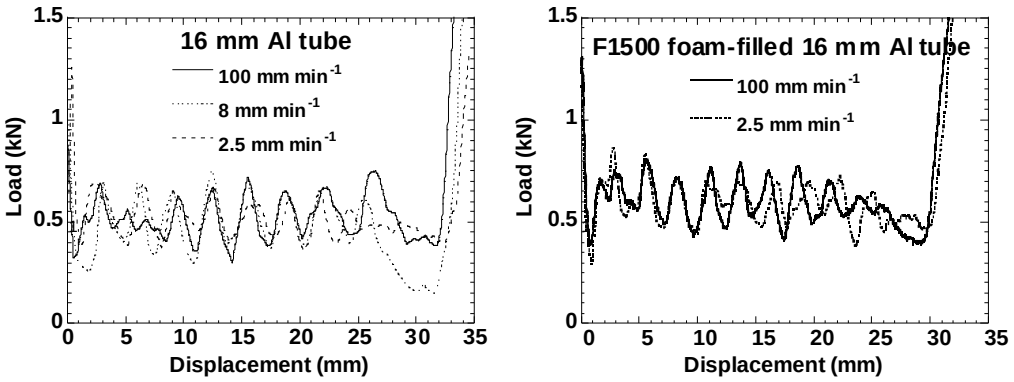

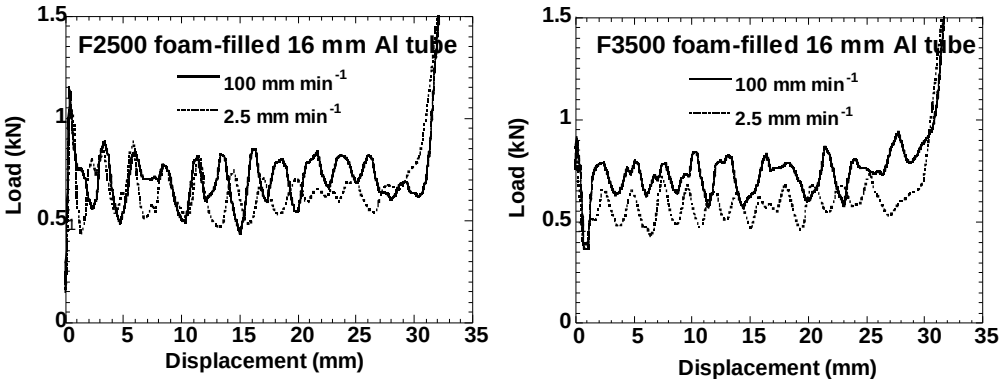

(c) (d)

Figure 4.28 Effect of deformation rate on the load-displacement curves of the 16 mm Al tube; a) empty and b) F1500, c) F2500 and d) F3500 filled tubes.

4.4.2 Effect Of Foam Filling On the Average Crushing Load, Stroke Efficiency And Specific Absorbed Energy

The average crushing load values of the empty and foam filled tubes showed initially a maximum and then reached almost a constant load value as the displacement increased. Foam filling increased the average crushing load of the tubes (Figure 4.29).

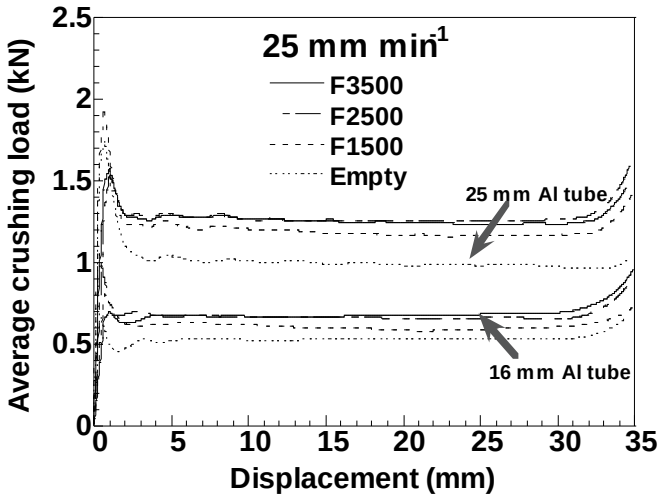

Figure 4.29 Effect of foam filling on the average crushing load of the Al tubes at 25 mm min^{-1}.

Figures 4.30(a) and (b) show the variation of the average crushing load (at 50% deformation) with the deformation rate for 16 and 25 mm Al tubes, respectively. A small effect of deformation rate on the average crushing load values of the filled tubes is seen in these curves. Each datum given in Figures 4.30(a) and (b) is the average value of the at least three tests and details of the tests are given in Appendix B.

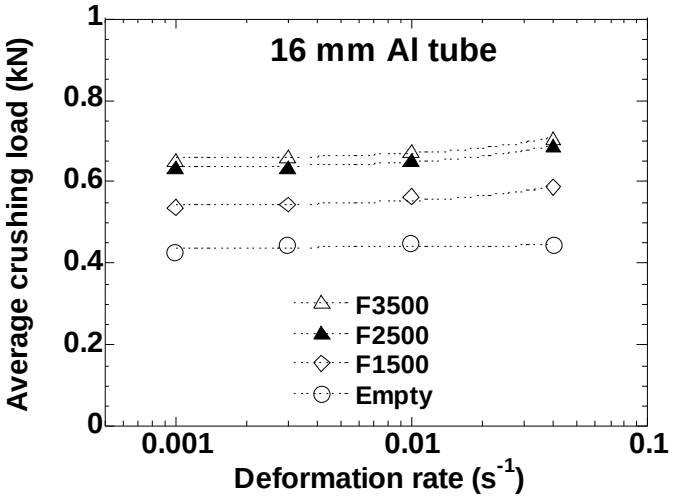

(a)

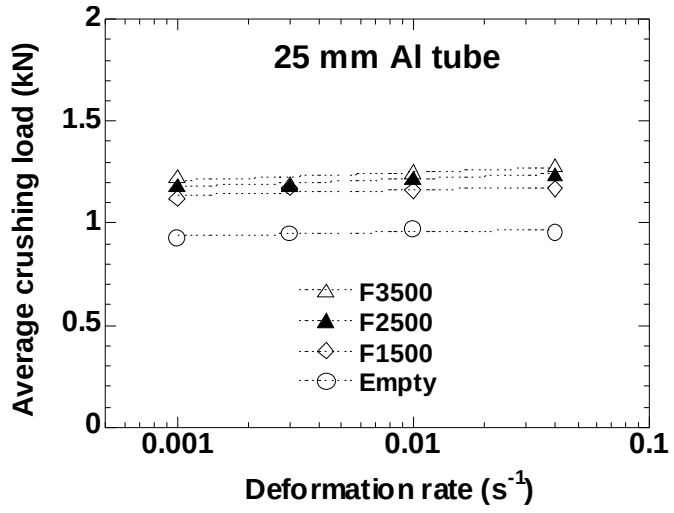

(b)

Figure 4.30 Average crushing load *vs.* deformation rate; a) 16 and b) 25 mm Al tubes.

Although foam filling increased the average load values, it decreased the stroke efficiency. Figure 4.31(a) and (b) show the variation of stoke efficiency in the tubes as function of deformation rate. Despite the small dependence on the deformation rate,

stroke efficiency decreased as the foam density increased in tubes and the dependency of stroke efficiency on the foam density is relatively smaller in 25 mm Al tube (Figure 4.32).

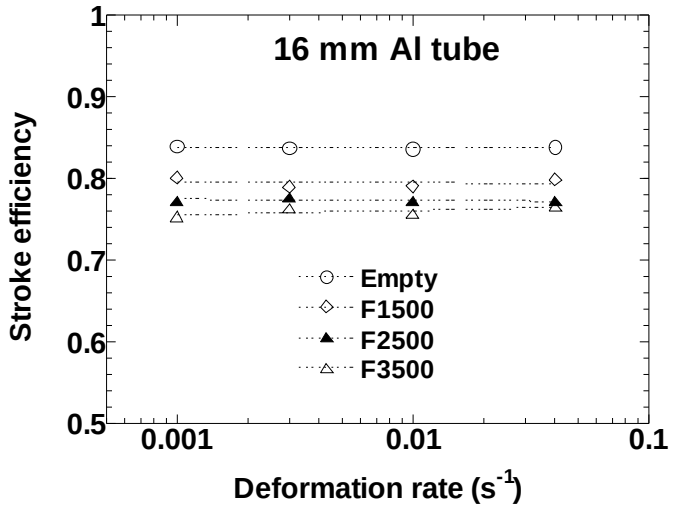

(a)

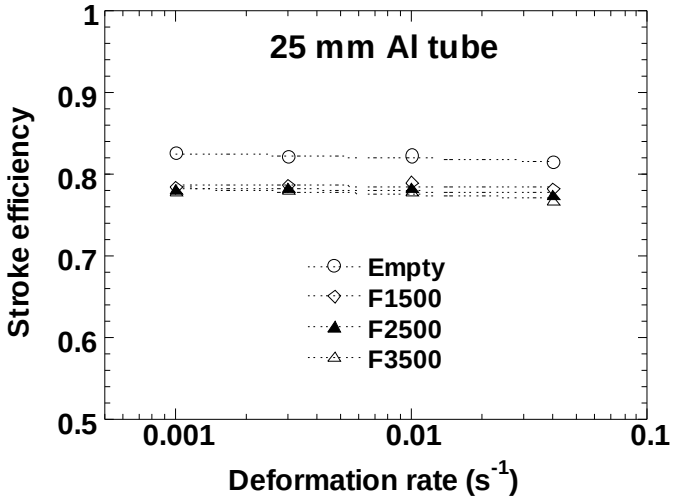

(b)

Figure 4.31 Effect of deformation rate on the stroke efficiency; a) 16 and b) 25 mm Al tubes.

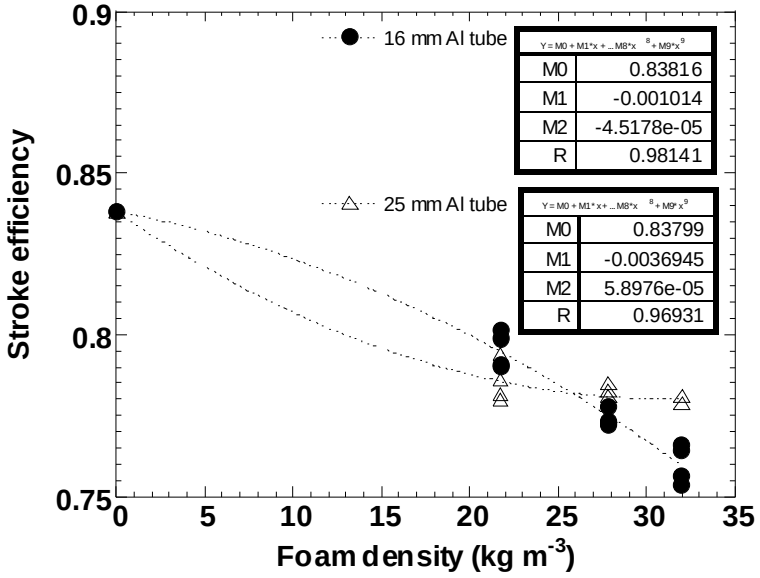

Figure 4.32 Effect of foam density on the stroke efficiency (deformation rate 0.001 s^{-1}).

The effect of deformation rate on the SAE at displacements corresponding to stroke efficiency of the empty and foam-filled tubes is shown sequentially for 16 and 25 mm Al tube in Figure 4.33(a) and (b). Although SAE increased with increasing foam filling in 16 mm Al tube, almost no significant effect of foam filling was found in 25 mm Al tube.

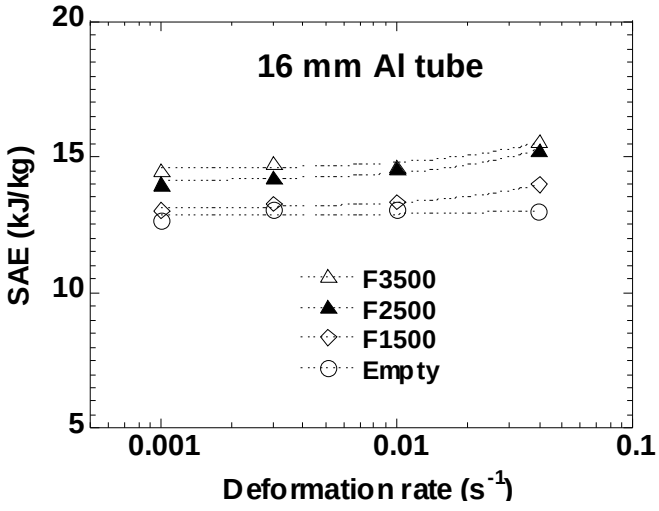

(a)

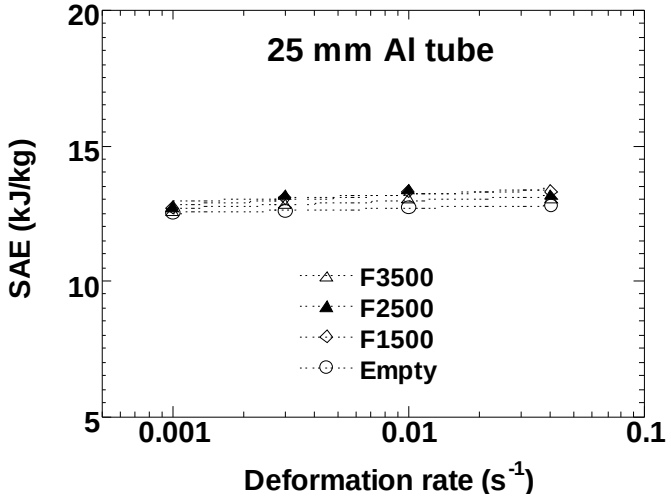

(b)

Figure 4.33 SAE *vs.* deformation rate; a) 16 and b) 25 mm tubes.

4.4.3 Effect of Adhesive

The effect of adhesive in 16 mm Al foam filled tubes was to increase the average crushing load slightly especially at low displacements (Figure 4.34(a)). On the other hand, no significant effect of the adhesive was found in foam-filled 25 mm Al tube. The foam filled tubes with and without adhesive deformed until various displacements were sectioned and examined. In 16 mm Al tubes without adhesive, it was found that after compression testing, the foam filler partially recovered (Figure 4.35), but foam fillers with adhesive showed no recovery after compression (Figure 4.36). In 25 mm tubes, the bonding between tube wall and filler broke down after the formation of the first couple of folds.

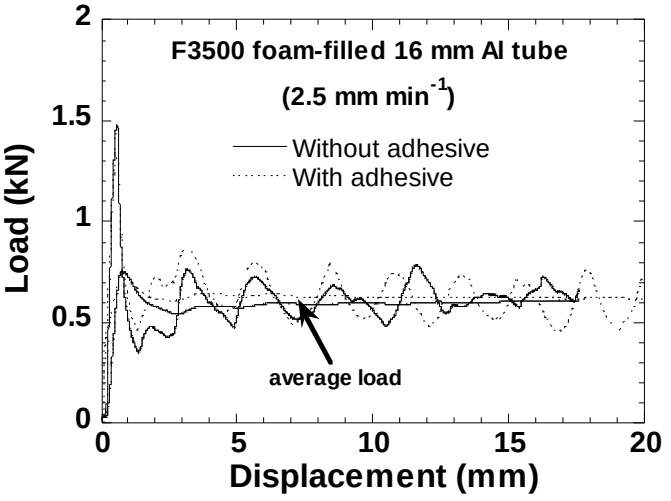

(a)

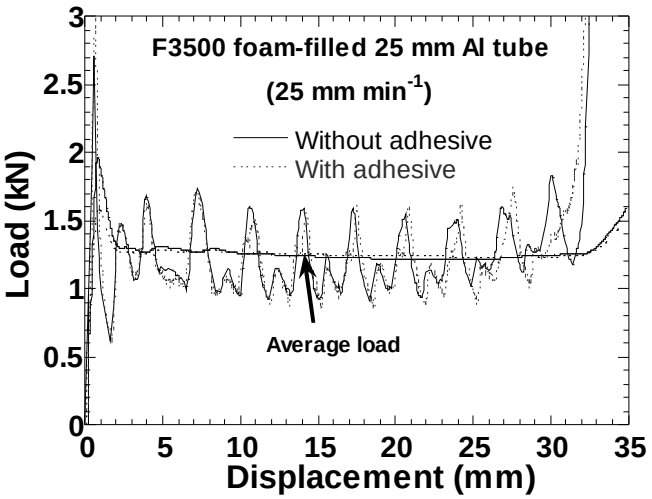

(b)

Figure 4.34 Effect of adhesive on the load and average crushing load of the foam-filled tubes a) 16 and b) 25 mm Al tubes.

Figure 4.35 Side and cross-sections of the foam-filled 16 mm Al tube without adhesive.

Figure 4.36 Side and cross-sections of the foam-filled 16 mm Al tube with adhesive.

4.4.4 Partially Filled Tubes

In partially filled 16 mm Al tube with adhesive, folding either started at the filled (sample A, Figure 4.37(a)) or empty (sample B, Figure 4.37(b)) end of the tube. The effect of partial foam filling in samples A, is the increase of the load values (Figure 4.38(a)) and reduction of the fold length as compared with empty tube, but the fold length almost remained to be the same with that of filled tube. In samples B, the fold length and load values are however similar to those of empty tubes until the point a, Figure 4.38(b), at which folding starts to proceed in the filled section. Thereafter, the fold length and the peak loads of samples B reach the level of the sample A. In partially foam-filled tubes, without adhesive the load-displacement curves were found to be similar to that of the filled tube with adhesive.

(a) (b)

Figure 4.37 Compressed partially filled 16 mm Al tubes; folding started at a) the filled end and b) empty end.

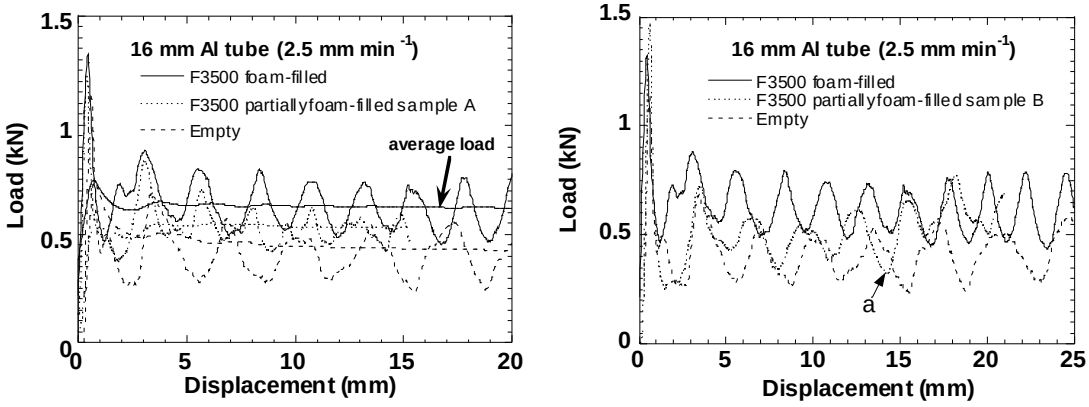

(a) **(b)**

Figure 4.38 Load-displacement curves of the empty, partially filled and filled tubes: a) sample A and b) sample B.

The load-displacement curves of the 25 mm Al empty and partially filled and filled tubes without and with adhesive shown in Figures 4.39(a-c). In partially filled tube without adhesive, folding similarly started either at the filled (sample A, Figure 4.40(a)) or empty (sample B, Figure 4.40(b)) end of the tube. The effect of foam filling in samples A, is the reduction of the fold length and increase of the load values (Figure 4.39(b)). In samples B, the fold length and load values are however the same with those of empty tubes until the point a of Figure 4.39(c), at which folding starts to proceed in the filled section. Thereafter, the fold length and the peak loads of samples B reach the level of the sample A (point b in Figure 4.39(c)). In partially filled tube with adhesive,

the deformation mode changes into concertina mode (Figure 4.40(c)), if the folding starts at the filled end, else the deformation mode is the same with that of empty tube. As shown in Figure 4.40(b) the concertina folding of the partially filled tube with adhesive shows a very similar load-displacement curve with the foam filled tube, except the magnitude of the load values are higher in the filled tube.

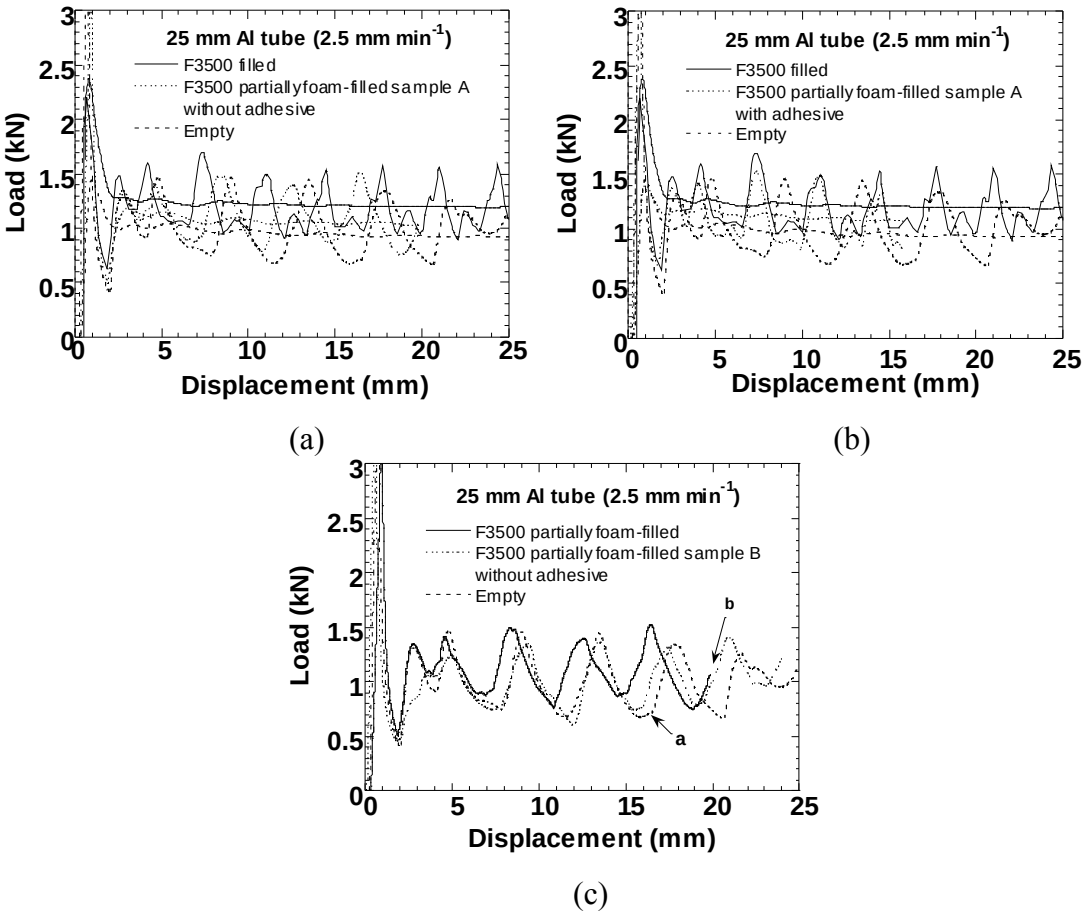

Figure 4.39 Load-displacement curves of 25 mm Al empty, partially filled and filled tubes; a) without adhesive sample A, b) with adhesive sample A and c) without adhesive sample B.

(a) (b) (c)

Figure 4.40 Cross-sections of deformed partially filled tubes a) sample A, b) sample B and c) sample A with adhesive.

In Tables 4.4 and 4.5 the crushing parameters of the partially filled 16 and 25 mm Al tubes are tabulated, respectively. In the same tables, the crushing parameters of the empty and filled tubes are also given for comparison. The effect of partial foam filling on the crushing behavior the Al tubes was the same with the full foam filling; decrease of fold length and increase of the average crushing load. It is also noted that the fold length of the partially and filled Al tubes are the same. This is also true for 25 mm Al tube when the partially filled tube deforms in concertina mode.

Table 4.4 Crushing parameters of empty, partially F3500 filled 16 mm Al tubes (average of 5 tests at 2.5 mm min^{-1})

16 mm Al tube	**P_a (kN)**	**ΔP_a (P_a-P_e) (kN)**	**Number of folds**	**Fold Length (mm)**	**Def. Mode**
Empty	0.43	0	9-10	3.4-3.8	diamond
Partially filled (adhesive)	0.53	0.1		2.2-2.3	diamond
Filled	0.65	0.22	10-11	2.2-2.5	diamond

Table 4.5 Crushing parameters of empty, partially F3500 filled 25 mm Al tubes (average of 5 tests at 2.5 mm min^{-1})

25 mm Al tube	**P_a (kN)**	**ΔP_a (P_a-P_e) (kN)**	**Number of folds**	**Fold Length (mm)**	**Def. Mode**
Empty	0.93	0	7-8	4.1-4.5	diamond
Partially filled	1.04	0.12		3.9-4	diamond
Partially filled (adhesive)	1.08	0.15		3.2-3.5	concertina
Filled	1.23	0.3	9-10	3.2-3.5	concertina

Chapter V

ANALYSIS OF RESULTS AND DISCUSSION

5.1 Average Crushing Loads of the Empty Tubes

The average crushing loads of the tested empty tubes were fitted with previously proposed equations for the average crushing loads of diamond and concertina deformation modes and the results are shown in Figures 5.1(a) and (b) as function of D/t. The experimentally determined average crushing loads in these figures corresponds to 50% deformation and it was also found that average crushing loads at 40 and 60% deformation were very similar to that of 50% deformation.

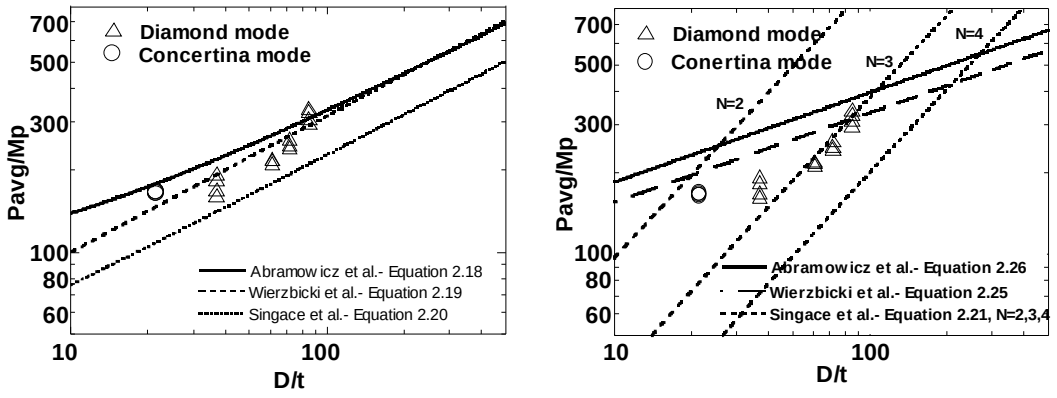

(a) (b)

Figure 5.1 Fitting of the experimental average crushing load with previously proposed equations for a) concertina and b) diamond deformation modes.

For both concertina and diamond mode, results are well fitted with empirical equations of Wierzbicki *et al.*[20] for concertina mode of deformation (Equation 2.19) within the studied D/t ratios (Figure 5.1(a)). Predicted values are in the range of 86- 99 % of the measured experimental values. Their empirical relationship for diamond mode (Equation 2.25) [10] predicts the average crushing load values in the range of 70-98% of the measured ones for diamond mode (Figure 5.1(b)). Above the D/t ratio of 60, this relationship were found to predict the average crushing loads in the range of 82-98% of the measured data.

As shown in Figure 5.1(b), Singace's empirical relationship [23] for diamond deformation mode with N=3 (Equation 2.21) gives good correlation between predicted and experimentally found average crushing loads in the D/t range between 60-80. Predicted values are in the range of 93.5 - 99 % of the measured experimental values for diamond mode. In this D/t ratio range the tested empty tubes deformed in diamond mode with 3 circumferential lobes, except 25 mm Al tube. Singace's empirical relationship for concertina deformation mode (Equation 2.20) [22] predicted lower and less accurate average crushing loads than that of the tested tubes results (Figure 5.1(a)).

Values of empirical relationship of Abramowicz *et al.* for concertina mode (Equation 2.18) [18], are higher than experimental ones until the D/t ratios reaches value of 80**.** Results of relationship of Abramowicz *et al.* [17] for diamond mode (Equation 2.26) is higher than experimental results. It was found that measured values are in the range of 65- 85 % of the predicted values for diamond mode.

5.2 Strengthening Coefficient of the Foam Filling

The simplest approach for predicting average crushing load of foam-filled tubes is to add the foam crushing load, which is usually taken as the load corresponding to the plateau stress, to the empty tube average crushing load. In the model, also called *additive* model, foam filler and tube are assumed to be deform independently.

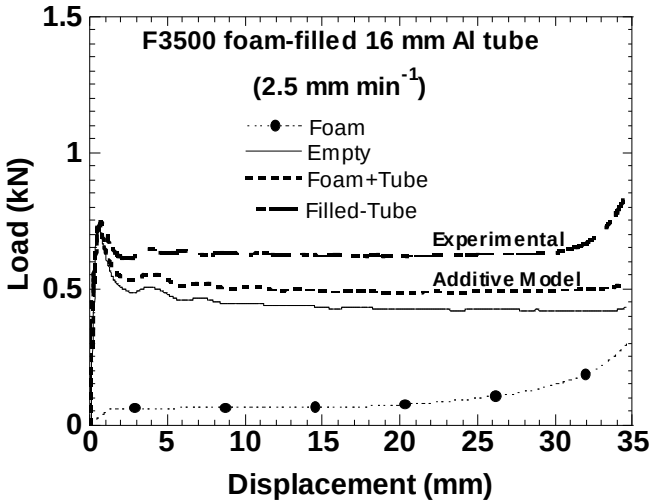

Figure 5.2 Loads and average crushing loads of the foam (alone), empty tube, empty tube+foam (alone) and foam filled tube .

Generally, the additive model gives the load and average crushing load values lower than experimental values for the reason of the interaction effect between the tube

wall and the filler. The interaction effect is also found in the tested polystyrene foam filled Al tubes (Figure 5.2).

The strengthening coefficient of foam filling can be expressed by modifying Equation 2.29 for circular tubes as;

$$C = \frac{P_{a,f} - P_a}{\sigma_p \pi R^2} = \frac{\Delta P_a}{P_f} \tag{5.1}$$

where P_f is the foam load corresponding to the plateau stress. The interaction between the filler and the tube was determined experimentally by avoiding the axial compression of the filler. In this case, the interaction load (P_{int}) and interaction coefficient (I) are expressed as,

$$P_{int} = P_{fp} - P_a^0 \tag{5.2}$$

$$I = \frac{P_{int}}{P_f} \tag{5.3}$$

where P_{fp} is the average crushing loads of the foam-filled tube without axial compression of the foam.

In order to find the strengthening coefficient of the polystyrene foam filling, the average crushing loads of the empty tubes were subtracted from those of the filled tubes and the results were divided by the foam load corresponding to the plateau stress. The calculations were made between the tests at the same deformation rates. Two different foam loads were used in the calculations: load corresponding to the plateau stress in the R direction and load corresponding to the sum of the plateau stresses in the R and W-directions. The results are shown sequentially in Figures 5.3(a) and (b) for foam load of R and R+W. Note also the slopes of the curves in Figures 5.3(a) and (b) correspond to the strengthening coefficient given in Equation 5.1. For the foam load of R direction, the 16 mm filled tube crushing load is about 3.2 times of the foam R-load, while a smaller strengthening coefficient is found for 25 mm tube, 1.82. For the foam load of R+W, the strengthening coefficients are about 1.8 and 1 for 16 and 25 mm tubes, respectively.

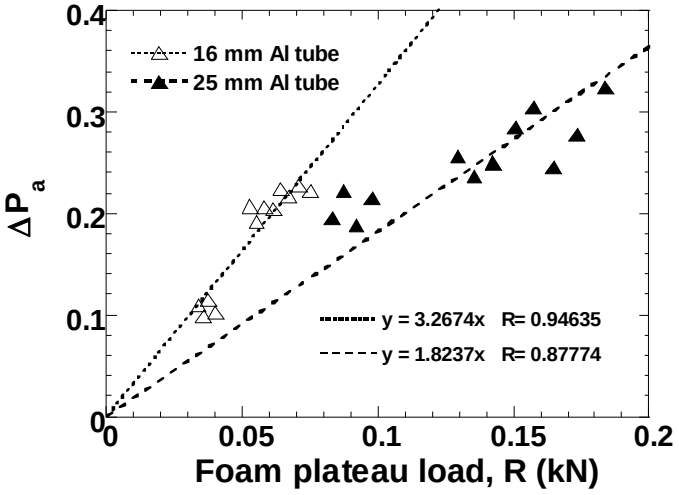

(a)

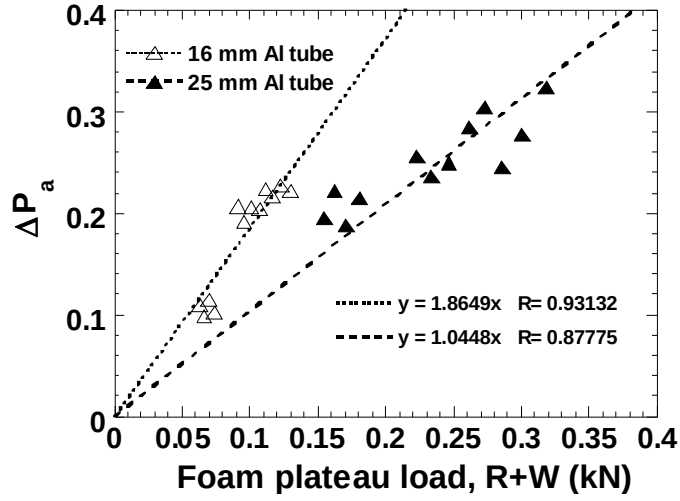

(b)

Figure 5.3 Increase in average crushing loads of Al tubes as function of the foam plateau loads a) R and b) R+W.

In the filled tubes, the interaction effect is partly due to the resistance of the filler to the inward and/or outward folding of the tube and partly due the interfacial friction stress between foam and tube wall [40]. Numerical studies of Al foam-filled tubes have shown a negligible effect of interfacial frictional stress on the crushing strength of tubes [31]. Figure 5.4 shows the stress-strain curve of the F3500 samples compressed inside the 25 mm Al tube (confined test) and unconfined F3500 samples (5x5x5 cm). Although the plateau stresses are the same, confined sample shows a higher densification strain. This tended to confirm that foam compression inside tubes showed the similar stress-strain behavior with the unconfined sample. This also partly

proved an insignificant effect of interfacial frictional stresses between the foam and the tube wall.

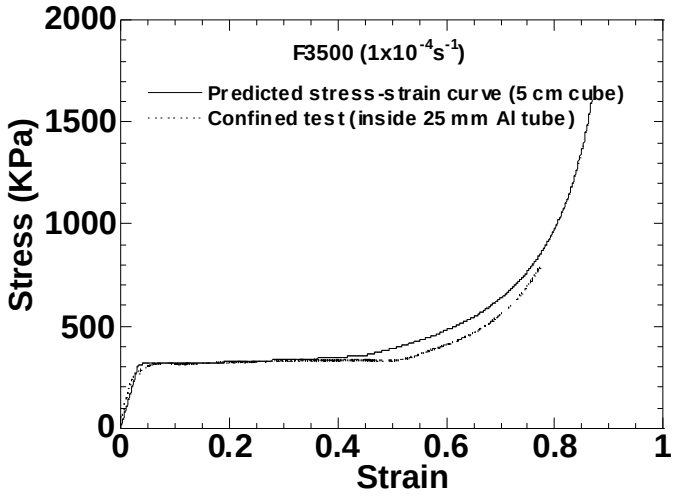

Figure 5.4 Comparison of the stress-strain curves of F3500 samples compressed inside 25 mm Al tube and unconfined sample (5cm cube).

The use of adhesive can contribute to the specific absorbed energy of the tube by two mechanisms, namely, increased load transfer from tube wall to the foam core and peeling of the adhesive [3, 31]. The latter mechanism occurs mainly due to the outward folding of the tube. In Al-foam filled tubes with an epoxy bonding layer between filler and the tube, the strengthening coefficient was numerically and experimentally found to be 2.8 for square tubes, which is higher than that of the foam filling without adhesive (1.8) [31].

The use of adhesive not only increases the strengthening coefficient but also changes the triggering position of the first fold. Figure 5.5 (a) and (b) show the axisymmetric folding of an Al tube; in empty tube folding started at the end of the tube, while it started in the mid-section of the tube in the case of aluminum foam filling.

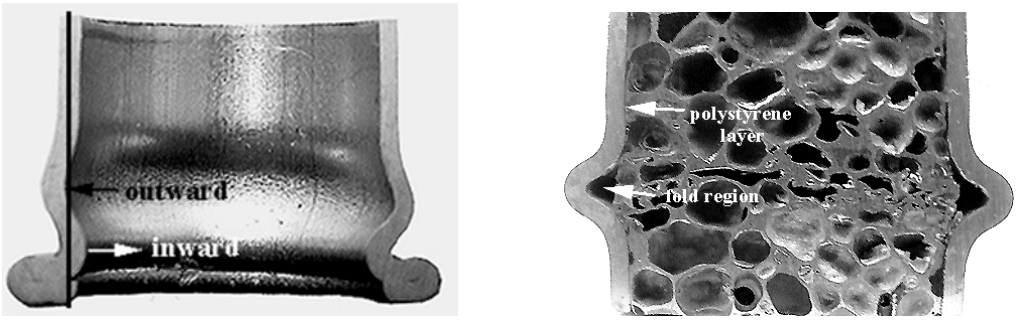

Figure 5.5 Axisymmetric folding in a) empty and b) Al-foam filled Al tubes [41].

This is basically due to the effect of local inhomogeneity of the foam, which forms a favorable side for fold formation on the tube. In polystyrene foam filled tubes, folding started at the end of the tube in all tested filled tube samples, proving the relatively homogenous cell size distribution of the foam used.

The deformation cross-sections of the 16 mm Al foam filled tubes with and without adhesive are shown in Figures 5.6(a) and (b), respectively. In both tubes, tube and filler deformation started at the end of the tube. This is in contrast to the foam alone deformation in which the deformation band forms in the mid sections. It is also noted in this figure, the filler deformation is localized in the fold region of the tubes. The separation of the tube wall from the filler during outward folding is clearly seen in Figure 5.6(b) for the without adhesive sample.

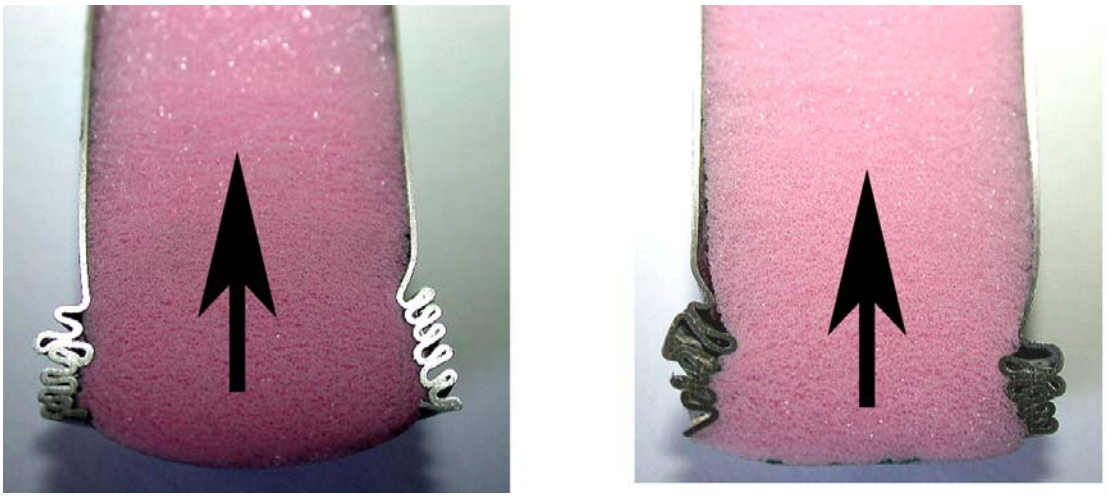

(a) (b)

Figure 5.6 F3500 foam filled 16 mm Al tubes; a) with adhesive and b) without adhesive.

Since the foam deformation started in the fold region, the axial strain in the foam may be assumed to scale with the fold length. The fold length can be roughly calculated using following relation:

$$H_f = \frac{S_E * l}{N} \tag{5.4}$$

where H_f is the fold length and N is the number of folds. Nearly 11 folds were formed in the foam filled 16 mm tube, corresponding to the fold length of 2.74 mm. Assuming the

folds moved until the faces touch to each other, the strain of the foam in the fold region is,

$$\varepsilon_f = \frac{H_f - 2t}{H_f} \tag{5.5}$$

This gives a compression strain of the filler nearly equal to 0.75. Replacing foam R load at 0.75 strain with plateau load in Figure 5.3 (b) gives a strengthening coefficient of 1 for the tested 16 mm foam filled Al tube (Figure 5.7).

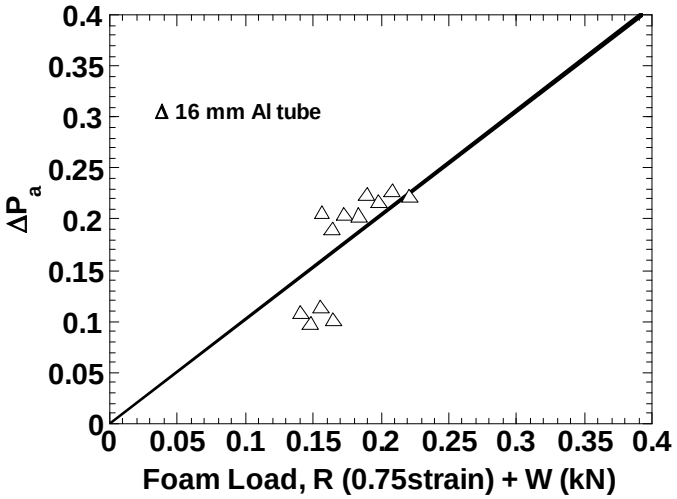

Figure 5.7 Increase in average crushing loads of foam filled 16 mm Al tubes as function of the foam load of R at 0.75 strain + W.

A close inspection of the crushed 16 mm Al foam filled tube also confirms the foam axial deformation in the fold area (Figures 5.8 (a) and (b)). Close inspection of the 25 mm foam filled tubes cross-sections showed that, foam and tube deformed independently in most part of deformation (Figure 5.9). In the filled tubes with adhesive, it was observed that the filler peeled off completely and/or partially from the tube wall after the first fold; therefore, the use of adhesive become ineffective. Mainly due to this effect, the load-displacement curves of the filled tubes with and without adhesive were found to be the same. In order to see the effect of adhesive clearly, compression tests using a stronger adhesive, epoxy, were performed. The insignificant difference between the adhesives in the load-displacement curve and average crushing

loads of the filled tubes tented to confirm the inefficiency of the adhesive in the filled 25 mm Al tubes (Figure 5.10).

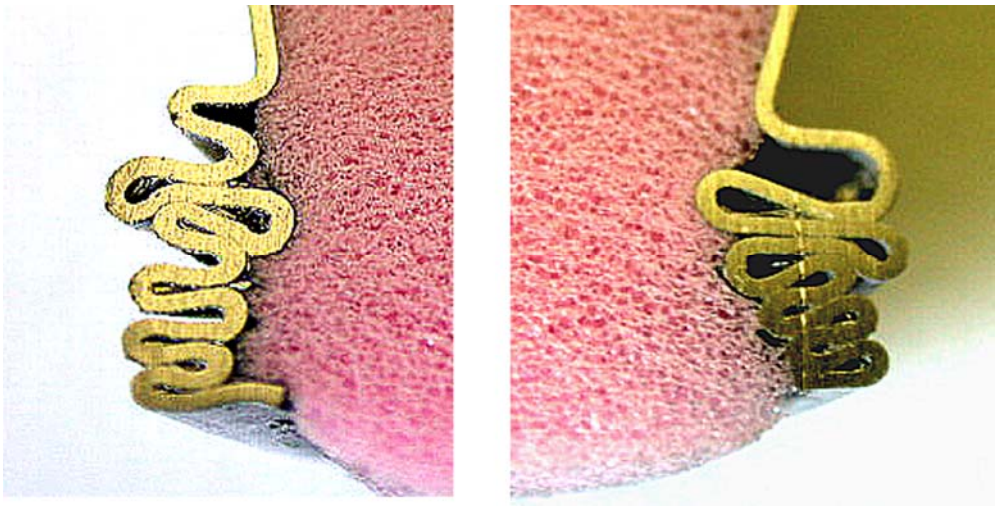

(a) (b)

Figure 5.8 Crushed F3500 foam filled 16 mm Al tubes; a) with adhesive and b) without adhesive.

Figure 5.9 Partially crushed F3500 foam filled 25 mm Al tubes with adhesive.

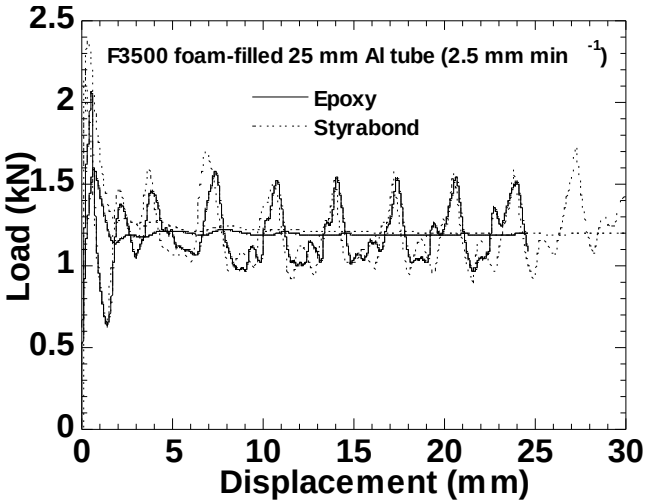

Figure 5.10 Load *vs.* displacement curves of 3500 filled 25 mm Al tube with Styrabond and epoxy.

The axial deformation of the filler in the fold region of 16 mm Al tube was also seen in the deformed cross-section of the partially filled tubes with and without adhesive, see Figures 5.11(a) and (b). In these tests as the tube compressed the foam length decreased due to the axial deformation in the fold region.

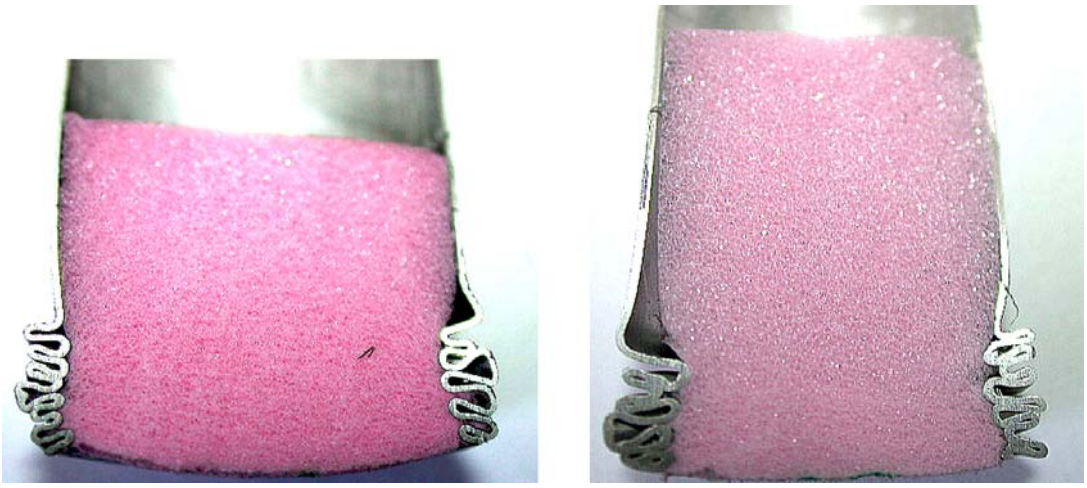

(a) (b)

Figure 5.11 F3500 partially filled 16mm Al tubes; a) with adhesive and b) without adhesive.

Figures 5.12 (a) and (b) show the partially foam filled 25 mm Al tube cross sections. Although no axial deformation of the foam is seen in the cross-section of the sample without adhesive (diamond), local axial deformation of the foam in sample with adhesive (concertina) is clearly seen. Therefore, it was found that partially filled tube

with adhesive showed a higher average crushing load as compared with that of the partially filled tube without adhesive.

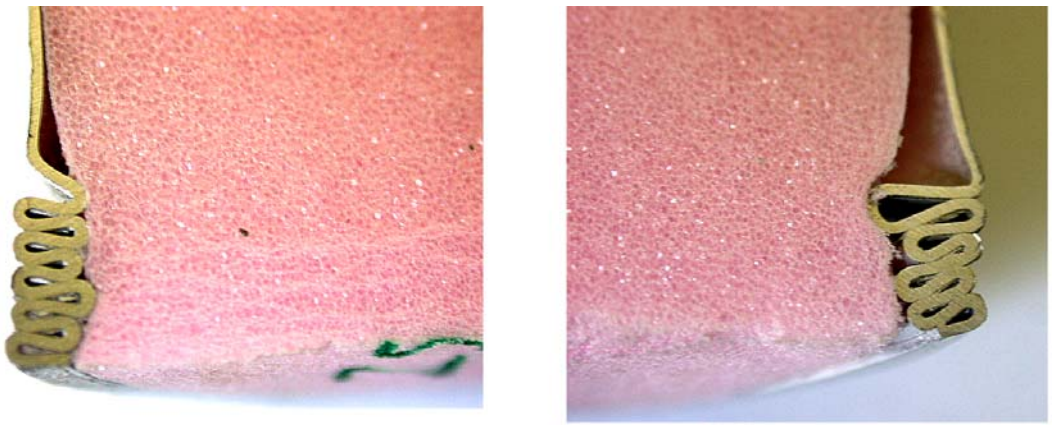

(a) (b)

Figure 5.12 F3500 partially filled 25 mm Al tubes; a) with adhesive and b) without adhesive.

The increase in the average crushing loads of the partially foam-filled tube (without adhesive) with respect to the empty tube is due to the resistance of the foam filler to the inward folding of the thin-walled tube, leading to shorter fold lengths and hence increased crushing loads. The interaction effect for the 16 mm Al tube with and without adhesive was higher than 1. In 25 mm Al tubes without adhesive it was found that the interaction effect was nearly 1 and with adhesive it was again greater than 1 (Figure 5.13). The strengthening coefficient of the polystyrene foam filling of the present study was also compared with those of the previous experimental studies on Al and polyurethane foam-filled Al cylindrical tubes [38, 39]. The comparison is shown in Figure 5.14, in which the strengthening coefficient is plotted as function of foam/tube load ratio.

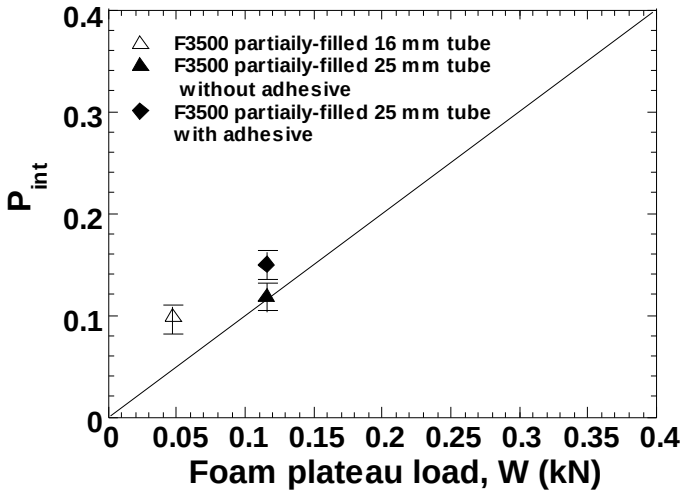

Figure 5.13 Increase in the average crushing loads of partially filled Al tubes as function of the foam plateau load of W.

Three distinct regions designated as 1, 2 and 3, are shown in Figure 5.14. In region 1, foam filling does not change the deformation mode: both empty and filled tubes deform in diamond or mixed mode. As the foam load increases, the deformation changes into mixed or concertina mode and in the third region, it is predominantly concertina. The highest strengthening coefficients, ranging between 2-4, are found in Region 1, where the foam load is relatively low as compared with the tube crushing load and foam filling does not change the deformation mode. In region 2, the foam filling switched deformation mode from diamond into mixed or concertina and the strengthening coefficient in this region fluctuates around 2. In the last region, the deformation mode is predominantly concertina and the strengthening coefficient is below 2 but higher than 1.

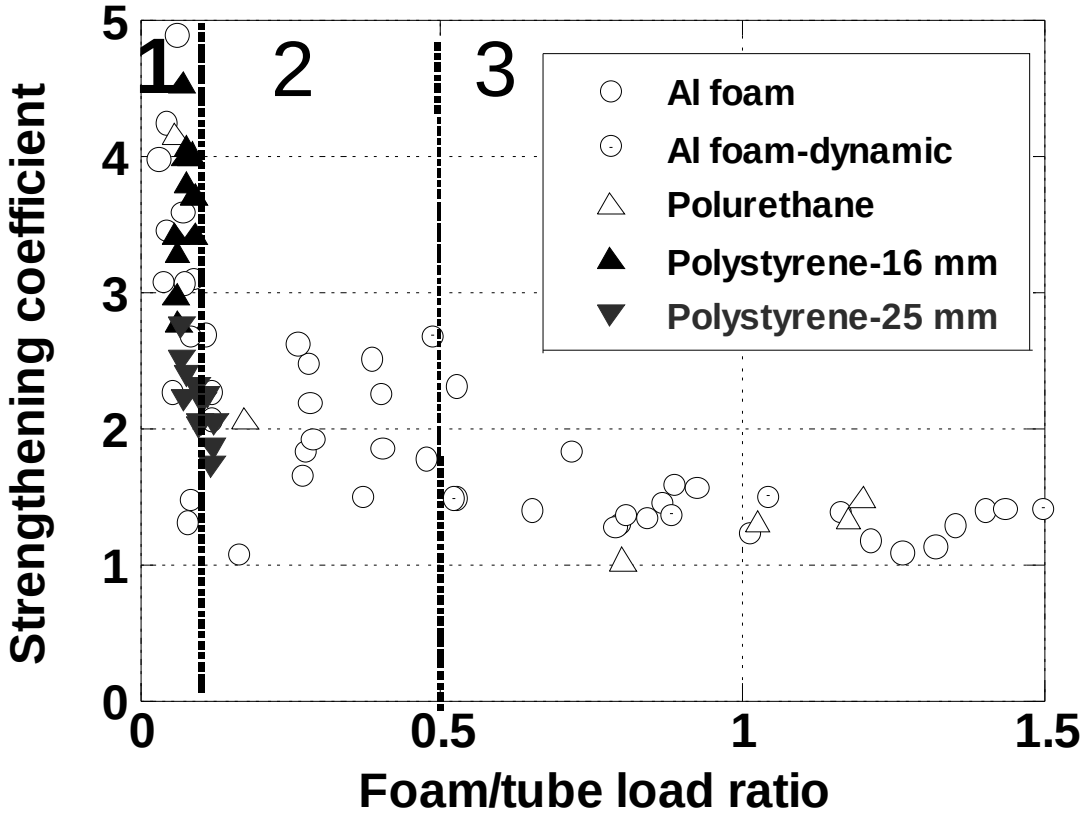

Figure 5.14 Comparison of strengthening coefficients polystyrene foam filling with those of previous studies of polyurethane and Al-foam filling.

The polystyrene foam filling of the present study shows good agreements with previous studies. For 16 mm tubes, in which the empty and foam-filled tubes deform in diamond mode shows strengthening coefficients higher than 2. The strengthening coefficient of the foam-filled 25 mm tubes, in which the deformation mode shifted to concertina is around 2.

5.3 Specific Absorbed Energy (SAE)

For efficient foam filling, the specific energy absorption of the foam filled tube should be higher than that of the empty tube at equal mass basis. The SAE of the foam filling is therefore should be compared with that of the wall thickening of the empty tube. This was done by assuming empty tubes average crushing loads followed the Equations 2.19 and 2.21. The details of the analysis is given in Appendix C.

In Figures 5.15 (a) and (b), variation of SAE with the total mass of the tubes are shown for 16 and 25mm Al tube, respectively. Foam filling in 16 mm Al tube is seen

to be advantages over the empty tube for the diamond mode of deformation. Note that in Figure 5.15 (a) there exists a critical mass (shown by arrows in Figure 5.15 (a)) and hence a critical foam density, after which the foam filling becomes more efficient than wall thickening. The critical mass decreases as the deformation rate increases and increases as the strengthening coefficient decreases. In 25 mm Al tube since the filled tube deformed in concertina mode the comparison is rather difficult. It is assumed that filled tube obeys the concertina mode and this gives a relatively lower SAE than empty tube (diamond) when the filler mass is zero (Figure 5.15 (b)). The low strengthening coefficient (1.82) in these tubes is the main reason for the inefficient foam filling when compared with wall thickening. But, again with increasing deformation rate the filling becomes more efficient.

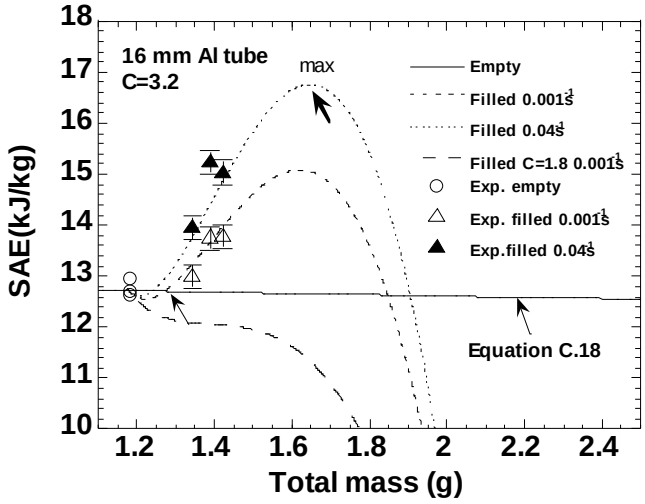

(a)

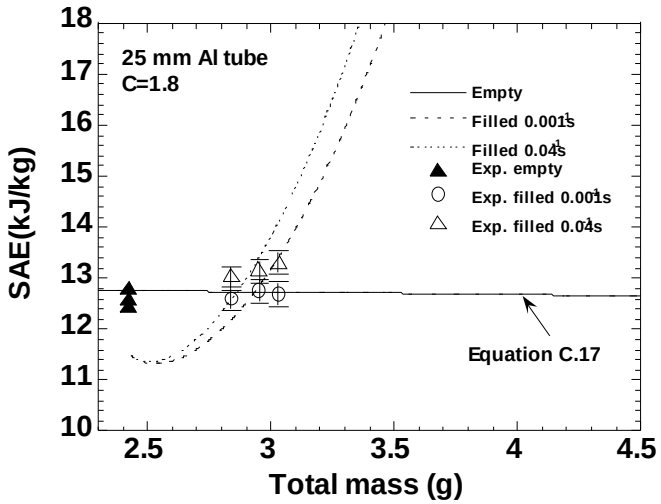

(b)

Figure 5.15 SAE *vs*. total mass; a) 16 mm and b) 25 mm Al tubes.

It is also noted that the SAE of the empty tubes are very similar, but foam filling makes the 16 mm Al tube more efficient, mainly due to the higher strengthening coefficient. Within the studied foam densities the increase in the SAE of the 16mm Al tube is as much as 15% and higher foam densities will be expected to increase SAE further.

One of the critical issues of foam filling is the reduction of the SE with the foam filling, which was more pronounced for the foam filled 16 mm Al tubes. At higher foam densities, the analysis showed that the reduction in SE overcome the increase in the average crushing force and therefore this resulted in a maximum in SAE-total mass curves as shown in Figure 5.15 (a). The critical foam density for 16mm Al tube is calculated 150 kg m^{-3} and after this density SAE decreases with foam filling. It should be noted that the analysis assumes a parabolic reduction in SE with the increasing foam density and any deviation from parabolic relation and change in deformation mode will change the predicted critical foam density.

5.4 Two Models of Foam Filled Tube Deformation

Based on experimental results and microscopic observation, two models of polystyrene foam filled thin-walled Al tube deformation are proposed. The first model is shown schematically in Figure 5.16(a) and features the axial deformation of the foam filler in between the folds. In this model, tube folding and filler axial deformation occur together. Therefore, the foam deformation in this model is determined by the amount of axial deformation of the folds and may be above the critical strain for densification; hence, the foam load may be well above the load of plateau stress. This model corresponds to the diamond mode of deformation of the polystyrene foam filled 16mm tubes in this study. The second model is based on independent deformation of the tube and filler and shown in Figure 5.16(b). Hence the foam deformation is independent from tube, the localized deformation of the foam and tube occurs in different regions of the tube. In this case, the foam deforms as if it were unconfined and this is proposed for the concertina mode of deformation in polystyrene foam filled Al tubes. The proposed models are also consistent with the previous studies shown in Figure 5.14, in which the diamond mode of deformation resulted in higher strengthening.

The reduction in the fold length was proved to be a result of filler resistance to inward folding of the tubes in partially filled tubes. This effect should also be clarified further by testing filled tubes with varying lateral resistance similar to the tests done in [29] with Al honeycomb filling.

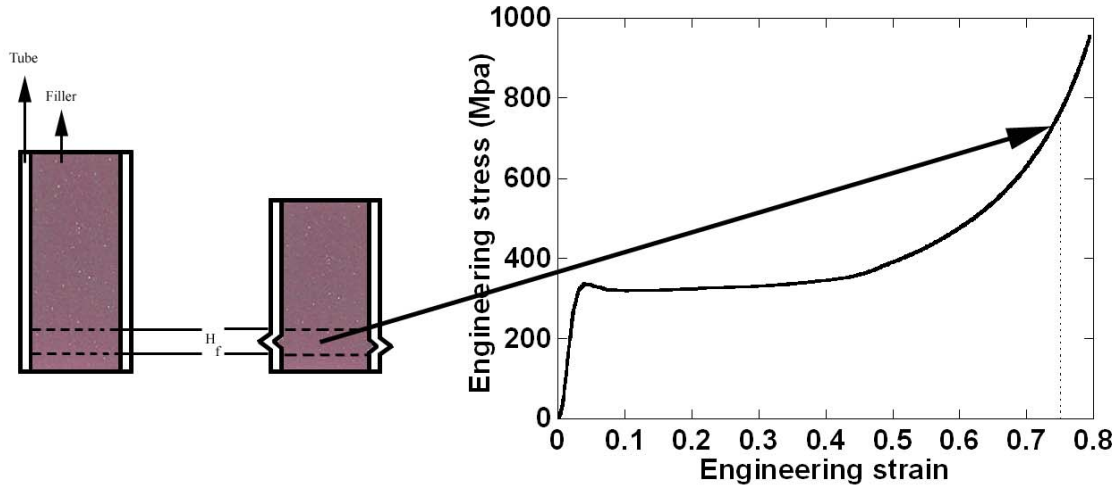

(a)

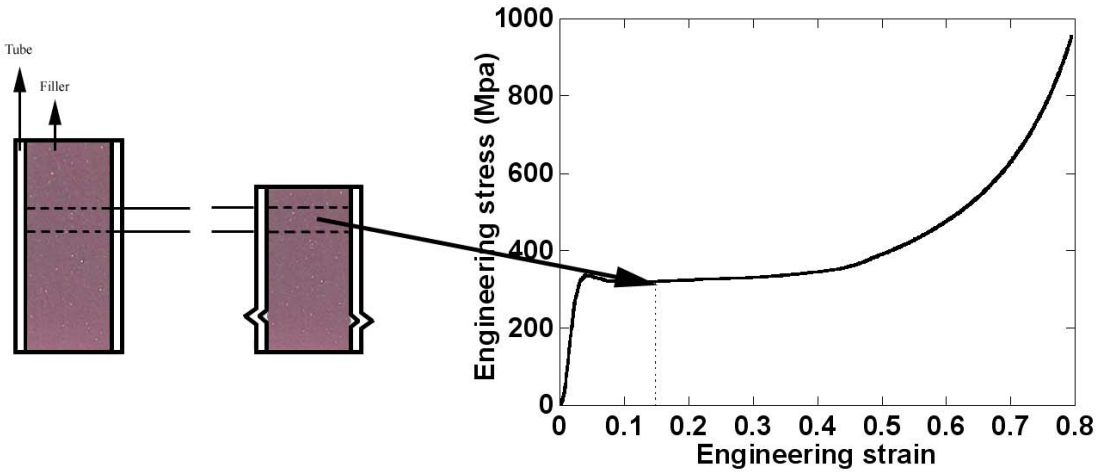

(b)

Figure 5.16 Schematic of the proposed two models of foam filled tube deformation; a) tube and filler deform together, b) tube and filler deform independently.

Chapter VI

CONCLUSIONS

The crushing behavior of the polystyrene foam filled Al-tubes have been investigated through compression testing of the filled and partially filled tubes at varying deformation rates. The effect of foam density, adhesive and deformation rate on the load-displacement, average crushing load and specific absorbed energy have been determined for two different modes of deformation: diamond and concertina. The specific energy absorption behavior of the empty and filled tubes was analyzed on the basis of the equal mass. Followings may be concluded

1. The foam filling changed the deformation mode of the 25 mm Al tube from diamond into concertina due to the thickening effect of the foam filling.
2. The effect of foam filling was to increase the average crushing load over that of the tube alone +foam alone, known as interaction effect. The foam filling, on the other hand, decreased fold length and the stroke efficiency.
3. The tests conducted on partially filled tubes have clearly shown that filler axial deformation triggered at a place at which folding started in diamond mode (16 mm Al), while filler and tube deformed independently in 25 mm Al tube (concertina).
4. No significant effect of adhesive use was found for the filled tubes. In 16 mm Al tube, the foam deformed in between the folds with and without adhesive. This was also confirmed by the microscopy of the compressed partially filled tubes. In 25 mm Al tube, the adhesive was presumed to be separated from the tube wall at the early stage of the folding, mainly due to the localized deformation of the filler in the mid sections. In partially filled tubes, it was found that the use of adhesive became effective and resulted in axial deformation of the filler in the fold region.
5. The deformation of the filler between the folds was likely to exceed the plateau stress of the foam, giving a higher strengthening coefficient in foam filled 16 mm Al tube as compared with 25 mm Al tube. The similarities between the strengthening coefficients of the present and previous studies

tended to conclude that diamond mode of deformation resulted in higher strengthening coefficient.

6. The results have also shown that there should be a critical foam density (or mass) before which the foam filling was not efficient in terms of SAE at equal mass basis. For the studied strain rate dependent polystyrene foam, the increasing deformation rate decreased the critical foam density and also increased the SAE.
7. The effect of reduction in the stroke efficiency with foam filling was found to result in a maximum in SAE in foam filled tubes.

REFERENCES

1. T. Wierzbicki, X. Teng, “How the airplane wing cut through the exterior columns of the World Trade Center”, International Journal of Impact Engineering, 28 ,2003, 601–625.

2. M. Seitzberger, F. G. Rammerstorfer, H. P. Degischer, “Crushing of axially compressed steel tubes filled with aluminum foam”, Acta Mechanica, 125, 1997, 93-105.

3. S. Santosa, T. Wierzbicki, A. G. Hannsen, M. Langseth, “Crash behavior of box columns filled with aluminum honeycomb or foam”, Computers and Structures, 68, 1998, 347-367.

4. L. J. Gibson, M. F. Ashby, “Cellular Solids: structures and properties, second edition”, Cambridge University Press, 1997.

5. M. Avalle, G. Belingardi, R. Montanini, “Characterization of polymeric foam under compressive impact loading by means of energy-absorption diagram”, International Journal of Impact Engineering, 25, 2001, 455-472.

6. S. K. Maiti, L. J. Gibson, M. F. Ashby, “Deformation and energy absorption diagram for cellular solids”, Acta Metall. , Vol. 32, 11, 1984, 1963-1975.

7. A. A. A. Alghamdi, “Collapsible impact energy absorbers : an overview”, Thin-Walled structures, 39, 2001, 189-213.

8. I. W. Hall, O. Ebil, M. Guden, C. J. YU, “Quasi-static and dynamic crushing of empty and foam filled tubes”, Journal of Materials Science, 36, 2001, 5853-5860.

9. A. A. Singace, “Collapse behavior of plastic tubes filled with wood sawdust”, Thin-Walled Structures, 37, 2000, 163-187.

10. W. Abramowicz, T. Wierzbicki, “Axial crushing of foam-filled columns”, Journal of Mechanical Science, 30 (3/4), 1988, 263.

11. A. K. Toksoy, M. Guden, I. W. Hall, “Axial compression of aluminum closed-cell foam filled and empty aluminum tubes”, Automotive Technologies Congress – Bursa, 24-26 June 202, Conference Proceeding, 383-386.

12. TY. Reddy, STS. Al Hassani, “Axial crushing of wood-filled square metal tubes”, International Journal of Mechanical Science, 35 (3/4), 1993, 231-246.

13. TY. Reddy, RJ. Wall, “Axial compression of foam filled thin-walled circular tubes”, International Journal of Impact Engineering, 7 (2), 1988,151-166.

14. J. M. Alexander, “An approximate analysis of the collapse of thin cylindrical shells under axial loading”, Quarterly Journal of Mechanics and Applied Mathematics, 13, 1960, 10-15.

15. K. R. F. Andrews, G. L. England, E. Ghani, “Classification of the axial collapse of cylindrical tubes under quasi-static loading”, International Journal of Mechanical Science, 25, 1983, No. 9-10, 687-696.

16. A. Kaan Toksoy, Halit Kavi, Unpublished study, Izmir Institute of Technology Mechanical Engineering Department, 2003

17. W. Abramowicz, N. Jones, “Dynamic axial crushing of circular tubes”, International Journal of Impact Engineering, 2, 1984, 263-81.

18. W. Abramowicz, N. Jones, “Dynamic progressive buckling of circular and square tubes”, International Journal of Impact Engineering, 4, 1986, 243-269.

19. N. Jones, W. Abramowicz, “ Static and dynamic axial crushing of circular and square tubes”, In : Reid SR, editor. Metal Forming and Impact Mechanics. New york: Pergamon Press, 1985, 225-47.

20. T. Wierzbicki, S.U. Bhat, W. Abramowicz, D. Brodkin, “A two folding elements model of progressive crushing of tubes”, International Journal of Solids and Structures, 29, 1992, 3269-3288.

21. A.A. Singace, H. Elbosky, “ Further experimental investigation on the eccentricity factor in the progressive crushing of tubes”, International Journal of Solid Structures, 33, 1996, No. 24, 3517-3538.

22. A.A. Singace, H. Elbosky, “On the eccentricity factor in the progressive crushing of tubes”, International Journal of Solid Structures, 32, 1995, 3589-3602.

23. A.A. Singace, “Axial crushing analysis of the tubes deforming in the multi-lobe mode”, International Journal of Mechanical Science, 41, 1999, 868-890.

24. AG. Pugsley., M. Macaulay, “The large scale crumpling of thin cylindrical columns”, Quarterly Journal of Mechanics and Applied Mathematics, 13, 1960, 1, 1-9.

25. F.C. Bardi, H. D. Yun, S. Kyriakides, “On the axisymmetric progressive crushing of circular tubes under axial compression”, International Journal of Solid Structures, 40, 2003, in press.

26. H. Abbas, B. L. Tyagi, M. Arif, N. K. Grupta, “Curved fold model analysis for axi-symmetric axial crushing of tubes”, Thin-Walled Structures, 2003, in press.

27. N. K. Grupta, H. Abbas, “Some considerations in axisymmetric folding of metallic round tubes”, International Journal of Impact Engineering, 25, 2001, 331-344.

28. T.Wierzbicki , W.Abramowicz , “Axial crushing of multi corner sheet metal columns”, Journal of Applied Mechanics, 50, 1983, 727-734.

29. T.Wierzbicki , W.Abramowicz , “On the crushing mechanics of thin-walled structures”, Journal of Applied Mechanics, 56, 1989, 113-120.

30. M. Seitzberger, F. G. Rammerstorfer, H. P. Degischer, “Crushing of axially compressed steel tubes filled with aluminum foam”, Acta Mechanica, 125, 1997, 93-105.

31. S. Sanatoza, T. Wierzbicki, A. G. Hanssen, M. Langseth, “Experimental and numerical studies of foam-filled sections”, International Journal of Impact Engineering, 24, 2000, 509-534.

32. A. G. Hanssen, M. Langseth, O.S. Hopperstad, “Static crushing of square aluminum extrusions with aluminum foam filler”, International Journal of Mechanical Science, 41, 1999, No. 8, 967-993.

33. A. G. Hanssen, M. Langseth, O.S. Hopperstad, “Static and dynamic crushing of square aluminum extrusions with aluminum foam filler”, Int. Journal of Impact Engineering, 24, 2000, 347-383.

34. ASTM D1621-00 D1621-00 Standard Test Method for Compressive Properties Of Rigid Cellular Plastics.

35. ASTM B557M, Standard Test Methods of Tension Testing Wrought and Cast Aluminum- and Magnesium-Alloy Products [Metric].

36. N. J. Mills, H. X. Zhu, “The high strain of closed cell polymer foams”, Journal of the Mechanics and Physics of Solids, 47, 1999, 669-695.

37. F. Ramsteiner, N. Fell, S. Forster, “Testing the deformation behavior of polymer foams”, Polymer Testing, 20, 2001, 661-670.

38. S.R. Guillow, G. Lu, R. H. Grebieta, “Quasi-static axial compression of thin-walled circular aluminum tubes”, International Journal of Mechanical Sciences, 43, 2001, 2103-2123.

39. A. G. Hanssen, M. Langseth, O.S. Hopperstad, “Static and dynamic crushing of circular aluminum extrusions with aluminum foam filler”, International Journal of Impact Engineering, 24, 2000, 475-507.

40. A. G. Hanssen, M. Langseth, O.S. Hopperstad, “Optimum design for energy absorption of square aluminum columns with aluminum foam filler”, International Journal of Mechanical Sciences, 43, 2001, 153-176.

41. A. K. Toksoy, M. Tanoğlu, M. Guden, I. W. Hall, “The effect of adhesive on the strengthening of aluminum foam-filled circular tube.”, International Journal of Material Science Letters, accepted.

APPENDIX A

ASTM B557M Tension Test Standart

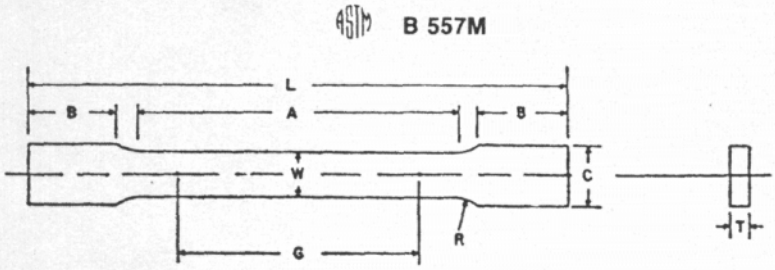

	Dimensions mm	
	Standard Specimen Sheet-Type 12.5 mm Wide	Subsize Specimen 6 mm Wide
G—Gage length	50.00 ± 0.10	25.00 ± 0.10
W—Width (Notes 1 and 2)	12.50 ± 0.05	6.00 ± 0.05
T—Thickness (Note 3)	thickness of material	thickness of material
R—Radius of fillet, min	12.5	6
L—Over-all length, min (Note 4)	200	100
A—Length of reduced section, min	57	32
B—Length of grip section, min (Note 5)	50	30
C—Width of grip section, approximate (Notes 2 and 6)	20	10

Figure A.1 Rectangular tension test specimens

NOTE 1—The ends of the reduced section shall not differ in width by more than 0.06mm for the 50.00 mm gage length specimen or 0.025 mm for the 25.00 mm gage length specimen. There may be a gradual taper in width from the ends of the reduced section to the center, but the width at each end shall not be more than 1% greater than the width at the center.

NOTE 2—For each of the specimens, narrower widths (*W* and C) may be used when necessary. In such cases the width of the reduced section should be as large as the width of the material being tested permits: however, unless stated specifically, the requirements for elongation in a product specification shall not apply when these narrower specimens are used. If the width of the material is less than *W,* the sides may be parallel throughout the length of the specimen.

NOTE 3—The dimension *T* is the thickness of the test specimen as stated in the applicable material specifications. Maximum nominal thicknesses of 12.5 mm and 6mm wide specimens shall be 12.5 mm and 6 mm, respectively.

NOTE 4—To aid in obtaining axial loading during testing of 6 mm wide specimens, the over-all length should be as large as the material will permit, up to 200 mm.

NOTE 5—It is desirable, if possible, to make the length of the grip section large enough to allow the specimen to extend into the grips a distance equal to two thirds or more of the length of the grips. If the thickness of 12.5 mm wide specimens is over 9 mm longer grips and correspondingly longer grip sections of the specimens may be necessary to prevent failure in the grip section.

NOTE 6—The ends of the specimen shall be symmetrical with the center line of the reduced section within 0.2 mm and 0.1 mm, respectively.

APPENDIX B

Experimental Results for Empty and Faom Filled Tubes

Table B.1 Analysis of experimental results of empty tubes ,outer diameter 16 mm and thickness of 0.22 mm.

Average - File Name	Strain Rate (s^{-1})	Pmax kN	P_a(40%) kN	P_a(50%) kN	P_a(60%) kN	P_a(SE) kN	SE	SAE(50%) kJ kg^{-1}	SAE(SE) kJ kg^{-1}
Ave.	**0.001**	**1.2500**	**0.4181**	**0.4133**	**0.4172**	**0.4183**	**0.8404**	**7.6589**	**12.624**
16-2		1.3280	0.3943	0.4066	0.4048	0.3952	0.8480	7.2108	12.625
16-3		1.2031	0.4154	0.4170	0.4193	0.4257	0.8249	6.9493	11.082
16-4		1.2188	0.4448	0.4382	0.4275	0.4146	0.8483	8.8166	14.167
Ave.	**0.003**	**1.3769**	**0.4781**	**0.4814**	**0.4807**	**0.4568**	**0.8373**	**8.2266**	**13.2535**
16-17		1.1250	0.4160	0.4201	0.4236	0.4193	0.8393	7.7283	12.953
16-18		1.3984	0.5127	0.5113	0.5017	0.4652	0.8424	8.6201	13.227
16-19		1.5234	0.4874	0.4889	0.4873	0.4796	0.8176	8.1584	13.759
16-20		1.4609	0.4963	0.5053	0.5102	0.4633	0.8501	8.3996	13.075
Ave	**0.01**	**1.1914**	**0.4490**	**0.4487**	**0.4512**	**0,4598**	**0,8367**	**7.9138**	**13.581**
16-21		1.3828	0.4498	0.4400	0.4392	0.4417	0.8350	8.1736	13.698
16-22		1.2422	0.5221	0.5356	0.5448	0.5601	0.8599	8.4127	15.149
16-23		1.2188	0.4326	0.4289	0.4232	0.4306	0.8234	7.8342	12.967
16-28		0.9219	0.3918	0.3903	0.3978	0.4071	0.8288	7.2348	12.510
Ave.	**0.04**	**1.2344**	**0.4848**	**0.4852**	**0.4886**	**0.4840**	**0.8385**	**8.2241**	**13.759**
16-24		1.1641	0.4289	0.4227	0.4213	0.4204	0.8423	7.7053	12.919
16-25		1.3672	0.5061	0.5127	0.5200	0.5173	0.8283	8.4085	14.054
16-27		1.1719	0.5195	0.5202	0.5247	0.5144	0.8451	8.5585	14.304

Table B.2 Analysis of experimental results of F1500 filled tubes ,outer diameter 16 mm and thickness of 0.22 mm.

Average - File Name	Strain Rate (s^{-1})	Pmax kN	$P_{a,f}$(40%) kN	$P_{a,f}$(50%) kN	$P_{a,f}$(60%) kN	$P_{a,f}$ (SE) kN	SE	SAE(50%) kJ kg^{-1}	SAE(SE) kJ kg^{-1}
Ave.	**0.001**	**1.088**	**0.5232**	**0.5261**	**0.5283**	**0.5342**	**0.7936**	**7.9773**	**12.867**
FF1611		0.7969	0.4664	0.4753	0.4805	0.4913	0.7975	7.6345	12.572
FF1612		1.2031	0.6116	0.6075	0.6046	0.5920	0.7897	8.5752	13.186
FF1613		1.2666	0.4916	0.4955	0.5000	0.5194	0.7936	7.7224	12.845
Ave.	**0.003**	**1.1172**	**0.52405**	**0.5447**	**0.5479**	**0.5606**	**0.7903**	**8.172**	**13.2715**
FF1614		1.1563	0.5510	0.5820	0.5874	0.5903	0.7929	8.3810	13.408
FF1615		1.0781	0.4971	0.5074	0.5084	0.5309	0.7877	7.9630	13.135
Ave.	**0.01**	**1.3437**	**0.5878**	**0.583**	**0.5833**	**0.6247**	**0.7787**	**8.6028**	**14.0866**
FF1617		1.1797	0.6234	0.6220	0.6239	0.6207	0.7943	8.8394	14.280
FF1618		1.4922	0.6397	0.6201	0.6177	0.7334	0.7873	8.9504	15.558
FF1619		1.3594	0.5003	0.5069	0.5085	0.5202	0.7546	8.0187	12.422
Ave.	**0.04**	**1.1640**	**0.5924**	**0.5915**	**0.5880**	**0.5827**	**0.7903**	**8.7340**	**13.659**
FF16110		0.8281	0.6159	0.6128	0.6070	0.6006	0.8054	8.9558	14.136
FF16111		1.3281	0.6214	0.6209	0.6133	0.5917	0.7666	8.8406	13.023
FF16112		1.3359	0.5400	0.5409	0.5439	0.5558	0.7989	8.4057	13.820

Table B.3 Analysis of experimental results of F2500 filled tubes , outer diameter 16 mm and thickness of 0.22 mm.

Average - File Name	Strain Rate (s^{-1})	Pmax kN	$P_{a,f}$ (40%) kN	$P_{a,f}$ (50%) kN	$P_{a,f}$ (60%) kN	$P_{a,f}$ (SE) kN	SE	SAE(50%) kJ kg^{-1}	SAE(SE) kJ kg^{-1}
Ave.	**0.001**	**1.1406**	**0.5999**	**0.6017**	**0.607**	**0.6064**	**0.7921**	**8.6761**	**13.758**
FF1621		1.3672	0.6404	0.6344	0.6340	0.6428	0.7737	8.6736	13.599
FF1622		1.0234	0.6370	0.6342	0.6444	0.6149	0.8022	9.0043	14.003
FF1623		1.0313	0.5223	0.5366	0.5426	0.5617	0.8006	8.3506	13.674
Ave.	**0.003**	**1.5156**	**0.6317**	**0.6369**	**0.6447**	**0.6498**	**0.7840**	**9.0170**	**14.455**
FF1624		1.5000	0.6835	0.6785	0.6720	0.6505	0.7765	9.2728	13.806
FF1625		1.6406	0.6534	0.6586	0.6717	0.6849	0.7842	9.1189	14.875
FF1626		1.4063	0.5582	0.5736	0.5906	0.6141	0.7915	8.6595	14.684
Ave.	**0.01**	**1.4713**	**0.6586**	**0.6543**	**0.6535**	**0.6574**	**0.7775**	**9.2900**	**14.5696**
FF1617		1.3672	0.5975	0.5930	0.5969	0.6138	0.7705	8.8275	14.189
FF1618		1.6406	0.6914	0.6898	0.6907	0.7063	0.7885	9.6100	15.526
FF1619		1.4063	0.6870	0.6801	0.6729	0.6523	0.7735	9.4327	13.994
Ave.	**0.04**	**1.5351**	**0.6837**	**0.6895**	**0.7028**	**0.7080**	**0.7726**	**9.6183**	**15.261**
FF16211		1.6953	0.6844	0.6951	0.7077	0.7196	0.7690	9.6798	15.420
FF16212		1.375	0.6831	0.6839	0.6980	0.6964	0.7763	9.5569	15.102

Table B.4 Analysis of experimental results of F3500 filled tubes , outer diameter 16 mm and thickness of 0.22 mm.

Average - File Name	Strain Rate (s^{-1})	Pmax kN	$P_{a,f}$(40%) kN	$P_{a,f}$(50%) kN	$P_{a,f}$(60%) kN	$P_{a,f}$(SE) kN	SE	SAE(50%) kJ kg^{-1}	SAE(SE) kJ kg^{-1}
Ave.	**0.001**	**1.2135**	**0.6227**	**0.6220**	**0.6262**	**0.6320**	**0.7533**	**8.7061**	**13.3923**
FF1631		1.3672	0.6519	0.6376	0.6285	0.6270	0.7332	8.6157	12.558
FF1632		1.2969	0.6569	0.6662	0.6781	0.6855	0.7707	9.1616	14.528
FF1633		0.9766	0.5593	0.5622	0.5721	0.5836	0.7562	8.3410	13.091
Ave.	**0.003**	**1.2396**	**0.6447**	**0.6466**	**0.6575**	**0.6750**	**0.7641**	**9.2375**	**14.7866**
FF1634		1.5938	0.6702	0.6750	0.6896	0.7044	0.7627	9.1294	14.528
FF1635		1.0781	0.6246	0.6141	0.6086	0.6129	0.7619	8.9570	13.625
FF1636		1.0469	0.6395	0.6507	0.6743	0.7077	0.7679	9.6962	16.206
Ave.	**0.01**	**1.3984**	**0.6698**	**0.6766**	**0.6817**	**0.6923**	**0.7624**	**9.2730**	**14.6040**
FF1637		1.1953	0.6806	0.6835	0.6833	0.6865	0.7499	9.4280	14.615
FF1638		1.4688	0.6653	0.6828	0.6985	0.7160	0.7564	9.2783	14.727
FF1639		1.5313	0.6636	0.6635	0.6635	0.6744	0.7809	9.1128	14.470
Ave.	**0.04**	**1.2808**	**0.6782**	**0.6880**	**0.6896**	**0.6984**	**0.7789**	**9.3637**	**14.853**
FF16310		1.6094	0.6561	0.6702	0.6734	0.6644	0.7926	9.0863	14.433
FF16311		1.1016	0.6960	0.7079	0.7061	0.7326	0.7784	9.6653	15.579
FF16312		1.1316	0.6825	0.6861	0.6895	0.6982	0.7658	9.3396	14.547

Table B.5 Analysis of experimental results of empty tubes ,outer diameter 25 mm and thickness of 0.29 mm.

Average - File Name	Strain Rate (s^{-1})	Pmax kN	P_a(40%) kN	P_a50%) kN	P_a(60%) kN	P_a(SE) kN	SE	SAE(50%) kJ kg^{-1}	SAE(SE) kJ kg^{-1}
Ave.	**0.001**	**2.0254**	**0.9218**	**0.9268**	**0.9324**	**0.9357**	**0.8261**	**7.5404**	**12.5857**
25-1		1.9531	0.9239	0.9546	0.9623	0.9438	0.8366	7.7426	12.813
25-2		1.7188	0.8519	0.8642	0.8799	0.9213	0.8061	7.0044	12.609
25-3		2.7500	1.0029	0.9833	0.9672	0.9642	0.8335	7.9584	12.456
25-4		1.6797	0.9088	0.9051	0.9203	0.9137	0.8282	7.4564	12.465
Ave.	**0.003**	**2.6883**	**0.9507**	**0.9518**	**0.9503**	**0.9375**	**0.82075**	**8.0027**	**12.4867**
25-16		2.8940	0.9341	0.9616	0.9729	0.9824	0.8174	7.8103	12.961
25-17		2.3984	0.9504	0.9608	0.9677	0.9379	0.8302	8.7962	12.536
25-18		3.0469	0.9995	0.9642	0.9510	0.9414	0.8032	7.8220	12.269
25-19		2.4141	0.9191	0.9209	0.9099	0.8883	0.8322	7.5826	12.181
Ave.	**0.01**	**2.5488**	**0.9875**	**0.9755**	**0.9786**	**0.9580**	**0.8227**	**7.8707**	**12.7207**
25-20		2.2266	0.9390	0.9196	0.9287	0.9166	0.8217	7.4395	12.193
25-21		2.5391	0.9967	0.9742	0.9767	0.9500	0.8303	8.0559	13.052
25-22		3.0078	1.0573	1.0508	1.0565	1.036	0.8122	8.2077	13.177
25-23		2.4219	0.9572	0.9577	0.9526	0.9295	0.8268	7.7797	12.461
Ave.	**0.04**	**2.2473**	**0.9527**	**0.9561**	**0.9635**	**0.9578**	**0.8079**	**7.8904**	**12.7783**
25-24		1.9609	0.9418	0.9425	0.9464	0.9536	0.8029	7.7653	12.625
25-25		1.7734	0.9523	0.9645	0.9794	0.9645	0.8148	7.9821	13.012
25-26		3.0078	0.9641	0.9615	0.9648	0.9554	0.8062	7.9238	12.698

Table B.6 Analysis of experimental results of F1500 filled tubes , outer diameter 25 mm and thickness of 0.29 mm.

Average - File Name	Strain Rate (s^{-1})	Pmax kN	$P_{a,f}$ (40%) kN	$P_{a,f}$ (50%) kN	$P_{a,f}$ (60%) kN	$P_{a,f}$(SE) kN	SE	SAE(50%) kJ kg^{-1}	SAE(SE) kJ kg^{-1}
Ave.	**0.001**	**2.6484**	**1.0934**	**1.0963**	**1.099**	**1.1925**	**0.7799**	**7.721**	**12.331**
FF25110		2.8515	1.1005	1.0997	1.1035	1.1336	0.7845	7.8447	12.688
FF25111		3.0469	1.0676	1.0672	1.0734	1.1010	0.7759	7.4711	11.943
FF25112		2.0469	1.1122	1.1221	1.1202	1.3430	0.7793	7.8472	12.362
Ave.	**0.003**	**3.2343**	**1.2145**	**1.2009**	**1.1988**	**1.2133**	**0.7863**	**8.3173**	**13.195**
FF2517		3.2734	1.2813	1.2553	1.2366	1.2410	0.7839	8.5318	13.149
FF2518		3.2891	1.1728	1.1739	1.1794	1.2032	0.7899	8.2587	13.371
FF2519		3.1406	1.1893	1.1736	1.1804	1.1958	0.7852	8.1615	13.066
Ave.	**0.01**	**3.0026**	**1.1983**	**1.192**	**1.1914**	**1.2054**	**0.7942**	**8.3747**	**13.510**
FF2514		2.9297	1.2670	1.2490	1.2354	1.2234	0.7930	8.7085	13.531
FF2515		2.9922	1.1508	1.1465	1.1522	1.1850	0.7897	8.0023	13.065
FF2516		3.0859	1.1771	1.1804	1.1865	1.2079	0.7998	8.4133	13.935
Ave.	**0.04**	**3.0312**	**1.1758**	**1.1712**	**1.1738**	**1.1975**	**0.7816**	**8.2394**	**13.346**
FF2511		2.9297	1.1667	1.1583	1.1540	1.1760	0.7850	8.3633	13.464
FF2512		2.8828	1.1476	1.1432	1.1550	1.1870	0.7813	8.1082	13.163
FF2513		3.2812	1.2132	1.2121	1.2124	1.2296	0.7786	8.2466	13.411

Table B.7 Analysis of experimental results of F2500 filled tubes , outer diameter 25 mm and thickness of 0.29 mm.

Average - File Name	Strain Rate (s^{-1})	Pmax kN	$P_{a,f}$(40%) kN	$P_{a,f}$(50%) kN	$P_{a,f}$(60%) kN	$P_{a,f}$(SE) kN	SE	SAE(50%) kJ kg^{-1}	SAE(SE) kJ kg^{-1}
Ave.	**0.001**	**2.7715**	**1.1896**	**1.1831**	**1.1834**	**1.2378**	**0.7853**	**7.8688**	**12.933**
FF2521		2.3359	1.1633	1.1604	1.1587	1.1936	0.7869	7.3390	12.507
FF2522		3.2131	1.2167	1.1924	1.1897	1.2858	0.7868	8.1058	13.012
FF2523		2.7656	1.1887	1.1964	1.2018	1.2341	0.7821	8.1616	13.279
Ave.	**0.003**	**2.4503**	**1.2157**	**1.216**	**1.221**	**1.2544**	**0.7812**	**8.1723**	**13.179**
FF2524		1.8438	1.1648	1.1575	1.1516	1.1824	0.7781	7.9150	12.586
FF2525		2.3432	1.2997	1.3032	1.3157	1.3332	0.7831	8.5822	13.759
FF2526		3.1641	1.1825	1.1874	1.1956	1.2475	0.7825	8.0198	13.193
Ave.	**0.01**	**3.1510**	**1.262**	**1.2595**	**1.2593**	**1.2814**	**0.7827**	**8.4918**	**13.52**
FF2527		3.2266	1.3262	1.3133	1.3144	1.3392	0.7729	8.6051	13.567
FF2528		3.2812	1.2146	1.2254	1.2254	1.2358	0.7936	8.3781	13.407
FF2529		2.9453	1.2452	1.2399	1.2380	1.2692	0.7817	8.4921	13.586
Ave.	**0.04**	**2.5468**	**1.2225**	**1.2194**	**1.2235**	**1.2564**	**0.7746**	**8.2566**	**13.183**
FF25210		2.7578	1.2409	1.2342	1.2348	1.2646	0.7733	8.3326	13.207
FF25211		2.6875	1.2027	1.2031	1.2116	1.2522	0.7734	8.1613	13.144
FF25212		2.1953	1.2238	1.2208	1.2242	1.2524	0.7771	8.2759	13.199

Table B.8 Analysis of experimental results of F3500 filled tubes , outer diameter 25 mm and thickness of 0.29 mm.

Average - File Name	Strain Rate (s^{-1})	Pmax kN	$P_{a,f}$(40%) kN	$P_{a,f}$(50%) kN	$P_{a,f}$(60%) kN	$P_{a,f}$(SE) kN	SE	SAE(50%) kJ kg^{-1}	SAE(SE) kJ kg^{-1}
Ave.	**0.001**	**3.0208**	**1.1963**	**1.1923**	**1.1933**	**1.2075**	**0.7784**	**7.9912**	**12.599**
FF2531		2.9844	1.2305	1.2318	1.2313	1.2130	0.7759	8.2968	12.679
FF2532		3.0469	1.1985	1.1868	1.1897	1.2180	0.7799	7.8689	12.599
FF2533		3.0312	1.1600	1.1584	1.1590	1.1915	0.7795	7.8080	12.519
Ave.	**0.003**	**2.7916**	**1.1693**	**1.1652**	**1.1647**	**1.1973**	**0.7808**	**7.6741**	**12.51**
FF2534		2.6953	1.1897	1.1962	1.1970	1.2357	0.7872	7.9549	12.945
FF2535		2.5703	1.1236	1.1052	1.0983	1.1213	0.7746	7.1680	11.776
FF2536		3.1094	1.1945	1.1942	1.1987	1.2349	0.7806	7.8993	12.809
Ave.	**0.01**	**2.4974**	**1.2367**	**1.2357**	**1.2347**	**1.2488**	**0.7809**	**8.2774**	**13.073**
FF2537		2.4609	1.2027	1.2011	1.1967	1.2066	0.7853	8.0861	12.783
FF2538		2.4141	1.2399	1.2554	1.2558	1.2589	0.7804	8.4627	13.251
FF2539		2.6172	1.2676	1.2507	1.2517	1.2808	0.7769	8.2835	13.186
Ave.	**0.04**	**2.5416**	**1.2465**	**1.2414**	**1.2394**	**1.2572**	**0.7592**	**8.3509**	**12.832**
FF25310		3.3672	1.3492	1.3399	1.3429	1.3544	0.7418	8.8465	13.264
FF25311		2.7578	1.2277	1.2207	1.2144	1.2414	0.7744	8.1381	12.818
FF25312		1.5000	1.1625	1.1635	1.1610	1.1758	0.7614	8.0682	12.415

APPENDIX C

Constitute Model of Specific Absorbed Energy

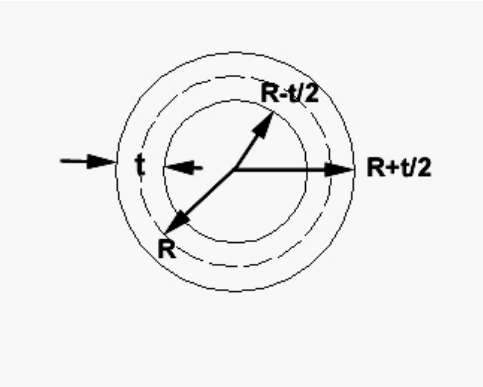

Figure C.1 Tube geometry

Specific absorbed energy calculations are formulated based on the tube geometry given in Figure C.1. The tube cross section area (A) and the mass (m_{tube}) of the tube geometry of Figure C.1 are;

$$A = \pi\left[\left(R + \frac{t}{2}\right)^2 - \left(R - \frac{t}{2}\right)^2\right] = 2Rt\pi \tag{C.1}$$

and

$$m_{tube} = \rho_c l A = \rho_c l 2Rt\pi \tag{C.2}$$

The filler area (A_f) and mass (m_f) are;

$$A_f = \pi\left(R - \frac{t}{2}\right)^2 = \pi\left(R^2 - Rt + \frac{t^2}{4}\right) \tag{C.3}$$

$$m_f = \rho^* l\pi\left(R^2 - Rt + \frac{t^2}{4}\right) \tag{C.4}$$

Combining Equations C.2 and C.4 gives the following relation for the total mass of the filled tube,

$$m_t = \rho_c l 2Rt\pi + \rho^* l\pi\left(R^2 - Rt + \frac{t^2}{4}\right) \tag{C.5}$$

Specific absorbed energy of the empty and filled tubes at the deformation length corresponding to stroke efficiency are expressed as,

$$SAE_{empty} = \frac{P_a}{m_t} S_E l \tag{C.6}$$

and

$$SAE_{filled} = \frac{P_a + P_f}{m_t} S_E l \tag{C.7}$$

The S_E values of the empty tubes are taken as the average of all experiments. However, the S_E values for filled tubes are expressed as a parabolic function of foam relative density, see Fig. 4.32.

C.4.1 Empty Tubes

C.4.1.2 Equation 2.18(Concertina mode - Wierzbicki et al.)

Inserting Equation 2.18 into Equation C.6 yields,

$$SAE_{empty} = \frac{11.22\sigma_0 t^{3/2} R^{1/2}}{m_t} S_E l \tag{C.8}$$

Rearranging Equation C.4 gives the thickness of the empty tube in terms of total mass and radius as,

$$t = \frac{1}{\rho_C l 2\pi} \frac{m_t}{R} \tag{C.9}$$

Substituting Equation C.9 into Equation C.8 yields,

$$SAE_{empty} = 3493.6 \, {}^{1}\!/_{R} \, S_E m_t^{1/2} \tag{C.10}$$

Values of the parameters given in Equation C.10 are as follows: ρ_C= 2700 kg/m^3, l=40 mm, σ_0=137.5 MPa, S_E (16 mm)= 0.838 and S_E(25 mm)= 0.8211. Using these values, following equations are derived for the SEA of 16 and 25 mm empty tubes as function of the total mass,

$$SAE_{empty} = 371.05 m_t^{1/2} \tag{C.11}$$

and

$$SAE_{empty} = 232.18 m_t^{1/2} \tag{C.12}$$

C.4.2 Equation 2.20 (Diamond mode - Singace et al.)

Using Equation 2.20 gives sequentially following equations for the SAE of 16 and 25 mm empty Al tubes deforming in diamond mode;

$$SAE_{empty} = -50456.066 m_t + 12641.598 \tag{C.13}$$

and

$$SAE_{empty} = -1.262 * 10^5 m_t + 12901.789 \tag{C.14}$$

C.4.2.1 Foam Filled Tubes

C.4.2.1.1 Equation 2.18 (Concertina mode - Wierzbicki et al.)

The average crushing load of the filled tube (concertina mode) is given by the following equation ,

$$P_a + P_f = 11.22\sigma_0 t^{3/2} R^{1/2} + CK\left(\frac{\rho^*}{\rho_s}\right)^n \pi\left(R^2 - Rt + \frac{t^2}{4}\right) \qquad (C.15)$$

Substitution of Equations C.15 and C. 5 into Equation C.7 gives the following equation for the SAE of the filled tube,

$$SAE_{filled} = \frac{11.22\sigma_0 t^{3/2} R^{1/2} + CK\left(\frac{\rho^*}{\rho_s}\right)^n \pi\left(R^2 - Rt + \frac{t^2}{4}\right)}{\rho_c l 2Rt\pi + \rho^* l\pi\left(R^2 - Rt + \frac{t^2}{4}\right)} S_E l \qquad (C.16)$$

Inserting the values of the parameters of the Equation C.16 gives sequentially following SAE of the filled 16 and 25 mm tubes as function of the foam density as;

$$SAE_{filled} = \frac{9.233 \cdot 10^9 + 18.243 \cdot 10^6 \rho^{*1.579}}{4.732 \cdot 10^6}(0.83816 -$$

$$0.001014\rho^* - 4.5178 \cdot 10^{-5}\rho^{*2}) \qquad (C.17)$$

and

$$SAE_{filled} = \frac{1.006 \cdot 10^{10} + 14.435 \cdot 10^6 \rho^{*1.579}}{6.56910^6}(0.83799 -$$

$$0.0036945\rho^* + 5.897 \cdot 10^{-5}\rho^{*2}) \qquad (C.18)$$

C.4.2.2.2 Equation 2.20 (Diamond mode - Singace et al.)

Substution of Equation 2.20 and foam load into Equation C.7 gives sequentially following relations for SAE of the 16 and 25 mm Al tubes deforming in diamond mode of deformation:

$$SAE_{filled} = \frac{9.257 \cdot 10^{9} + 18.243 \cdot 10^{6} \rho^{*1.579}}{4.732 \cdot 10^{6}} (0.83816 - 0.001014\rho^{*} - 4.5178 \cdot 10^{-5} \rho^{*2}) \quad \text{(C.19)}$$

and

$$SAE_{filled} = \frac{1.101 \cdot 10^{10} + 14.435 \cdot 10^{6} \rho^{*1.579}}{6.56910^{6}} (0.83799 - 0.0036945\rho^{*} + 5.897 \cdot 10^{-5} \rho^{*2}) \quad \text{(C.20)}$$